Technische Universität München
Fakultät für Physik

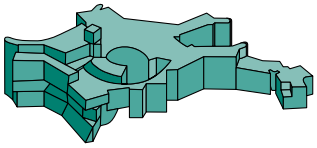

Max-Planck-Institut
für Astrophysik

Applications of Different Neutrino-Transport Methods in Three-Dimensional Supernova Simulations

Robert Maximilian Glas

Vollständiger Abdruck der von der Fakultät für Physik der Technischen Universität München zur Erlangung des akademischen Grades eines

Doktors der Naturwissenschaften (Dr. rer. nat.)

genehmigten Dissertation.

Vorsitzender:		Prof. Dr. Lothar Oberauer
Prüfer der Dissertation:	1.	apl. Prof. Dr. Hans-Thomas Janka
	2.	Prof. Dr. Alejandro Ibarra

Die Dissertation wurde am 15.10.2019 bei der Technischen Universität München eingereicht und durch die Fakultät für Physik am 04.12.2019 angenommen.

Contents

Chapter 1.

Introduction

When in the year 1054 Chinese astronomers observed a "guest star" in the constellation Taurus (Clark and Stephenson, 1977), they could hardly envision what we know today: the life of a massive star had ended in a tremendous explosion, outshining its entire host galaxy in visible light and appearing so bright in the sky that astronomers on Earth could mistake the distant explosion for a visiting star (see, for example, Hester 2008 and Blandford and Bühler 2017). It took many hundreds of years, before Lundmark (1921) identified the matter that was expelled during this ancient explosion as the Crab Nebula, which had already been discovered by English astronomers in the 18^{th} century. It was Baade and Zwicky (1934a,b) who speculated for the first time about the "transition of an ordinary star into a neutron star" at the end of a star's lifetime, taking place in an explosive event they termed "supernova". A few decades later, Staelin and Reifenstein (1968) found the associated compact remnant that survived the explosion seen in 1054 (Comella et al., 1969)—the Crab Pulsar, a neutron star spinning at a frequency of approximately 30 Hz today (Lyne et al., 2015).

The Current Understanding of Supernovae Since these early days of supernova research, our knowledge about stellar explosions has grown a lot. While accreting or merging white dwarfs that approximate the Chandrasekhar mass limit (Chandrasekhar, 1931, 1935) fade away in a thermonuclear explosion that disrupts the whole star (see, e.g., the reviews by Hillebrandt and Niemeyer 2000 and Hillebrandt et al. 2013), more massive stars with masses larger than approximately $8\,\mathrm{M}_\odot$ explode as core-collapse supernovae (CCSNe), leaving behind a compact remnant that is either a neutron star or a black hole. On their way to core collapse, these massive stars run through several successive burning stages, in which lighter elements are fused to heavier ones. Consisting of mostly hydrogen ($\approx 75\,\%$) and some helium ($\approx 25\,\%$) in the beginning, these stars develop iron cores that eventually become unstable against the gravitational collapse (see, e.g., the historical review by Bethe 1990). During core collapse, the matter is compressed to central densities exceeding the nuclear density ($\approx 2.7 \times 10^{14}\,\mathrm{g\,cm^{-3}}$, see, e.g., Janka 2012), at which the short-range forces of the strong interaction start to strongly repel nucleons from each other. While adjusting to a new equilibrium state, the inner core rebounds, abruptly halting the collapse, and emitting a shock wave that begins to run outwards through the still infalling outer core. Contrary to the initial conjecture (Colgate and Johnson, 1960), this prompt shock does not instantly break out, but instead stalls because of energy losses mainly due to the dissociation of the iron-group nuclei into neutrons and protons. The shock turns into an accretion shock. It was Colgate and White (1966) who first accounted for the important role of neutrinos, which are generated in vast amounts during the collapse by electron captures on protons and nuclei, and which carry away $99\,\%$ of the released gravitational binding energy ($\approx 10^{53}\,\mathrm{erg}$) of the emerging proto-neutron star. By proposing that a small fraction of these neutrinos are reabsorbed by the stellar matter and, thus, power the explosion by depositing their energy, Colgate and White laid the foundations of the present theoretical understanding of the CCSN mechanism.

The Delayed Neutrino-Heating Mechanism Based on that previous research, Bethe and Wilson (1985) worked out the delayed neutrino-heating mechanism, according to which the stalled shock wave is revived after a few hundreds of milliseconds due to the continuous heating of the post-shock matter by neutrinos that stream out of the hot proto-neutron star (see also the reviews by Kotake et al. 2006, Janka et al. 2012, Burrows 2013, and Foglizzo et al. 2015). During this phase, hydrodynamic instabilities play an important role in supporting the shock revival. On the one hand, convection in the gain layer (i.e., the region behind the shock where neutrino heating processes dominate the cooling reactions) is triggered by a negative entropy gradient that arises due to the heating by neutrinos. As a consequence of convective overturn, fresh, low-entropy matter is transported down to the regions of strong heating, and buoyant bubbles with high-entropy material rise up to the shock front, instead of being accreted onto the proto-neutron star. On the other hand, the standing accretion shock instability (SASI) reveals itself as large-scale oscillation of the shock front, most commonly in the form of dipolar sloshing or spiral modes (Blondin et al., 2003; Blondin and Shaw, 2007; Foglizzo et al., 2007). Besides helping the shock revival by pushing the shock farther out, both convection and SASI cause non-radial flows that increase the dwell time of matter in the gain layer.

The delayed neutrino-heating mechanism provides the currently most promising explanation of the final fate of most massive stars (see, for example, Janka 2012, who also discusses alternative mechanisms). It is consistent with the only measurement of neutrinos from a supernova (SN 1987A), which was observed in February 1987 in the Large Magellanic Cloud (Hirata et al., 1987; Bionta et al., 1987; Alexeyev et al., 1988). Still, various open questions regarding CCSNe need to be finally answered, for example: what are the properties of the emerging compact remnant, such as the mass, spin, and kick velocity? Which elements are produced by nucleosynthesis, and then expelled during the explosion? Which progenitor stars fail to explode and instead collapse to black holes? For all of these questions, a detailed understanding of the neutrino-heating mechanism is inevitable. Although we have learned a lot through observations of optical and other electro-magnetic radiation, these measurements are rather limited with respect to the central explosion engine because the inner regions of stars are not transparent to photons. A lot more information could be obtained from neutrino measurements, but with the exception of SN 1987A, from which two dozen neutrinos were detected on Earth, we do not have any observational data for neutrinos from supernovae. In addition, up to now we have not measured any gravitational-wave signal from a supernova (Abbott et al., 2016).

Modeling Core-Collapse Supernovae For this reason, most of our knowledge about the neutrino-heating mechanism of CCSNe originates from first-principle simulations of the collapse and post-bounce phase of massive stars. Starting from initial conditions describing the progenitor star, these simulations model the temporal evolution of the stellar fluid by solving the equations of hydrodynamics, which correspond to conservation laws for the density, momentum, and total energy of the matter. The hydrodynamics equations are self-consistently coupled to a neutrino radiation-transport scheme, including neutrino-matter interactions like absorption, emission, and scattering processes. They further account for the gravitational self-interaction of the stellar medium, and are completed by a microphysical equation of state which describes the behavior of nuclear matter.

Simulations in one dimension (i.e., assuming spherical symmetry; 1D) fail to explode most of the stars (see, e.g., Thompson et al. 2003) because they neglect important non-radial flows induced by hydrodynamic instabilities. Nevertheless, the delayed neutrino-heating mechanism has been shown to work in many two-dimensional (i.e., assuming axial symmetry; 2D) and an increasing number

of three-dimensional (i.e., using no symmetry assumptions; 3D) simulations (see, e.g., Janka et al. 2012; Takiwaki et al. 2012, 2014; Lentz et al. 2015; Müller 2015; Janka et al. 2016; Bruenn et al. 2016; Roberts et al. 2016; Summa et al. 2016; Ott et al. 2018; Vartanyan et al. 2019b,a). However, 2D simulations are restricted by the symmetry assumption, which influences the development of hydrodynamic instabilities, and 3D simulations do not result in robust explosions (see, e.g., Hanke et al. 2013; Melson et al. 2015a; Müller et al. 2017; Summa et al. 2018; O'Connor and Couch 2018b) or cannot explain the observed explosion energies (Burrows et al., 2019).

Neutrino Transport Another important aspect of modeling CCSNe is the transport of neutrinos, which in general is governed by the seven-dimensional Boltzmann equation describing the temporal evolution of the particle distribution function in the six-dimensional phase space (i.e., depending on three spatial and three momentum space coordinates, and time). However, a direct solution of the time-dependent Boltzmann equation in its full complexity and with high resolution is computationally not feasible at the moment. For this reason, several approximations have been introduced to reduce the complexity of the full Boltzmann equation. One class of approximations is based on the angular moments (i.e., integrals over the solid angle in momentum space) of the particle distribution function or the closely related specific intensity. In particular, two-moment schemes evolve the energy density and the energy-flux density of neutrinos, which correspond to the zeroth and first angular moments, respectively. The system of moment equations needs to be closed by relating the neutrino-pressure tensor (corresponding to the second moment) to the low-order moments, for example via an analytic expression. Such two-moment schemes (often also called "M1" methods) are commonly employed in the literature (see, for example, Foucart et al. 2015, Just et al. 2015, O'Connor and Couch 2018a, Skinner et al. 2016, Roberts et al. 2016 and Kuroda et al. 2016).

The RbR+ Approximation Another widely used approximation is ray-by-ray-plus (RbR+) transport (Rampp and Janka, 2002; Buras et al., 2006b), for which the specific intensity is assumed to be spherically symmetric around the radial direction of the spherical polar coordinate system. A direct consequence of the RbR+ approximation in a two-moment scheme are vanishing non-radial (i.e., polar and azimuthal) components of the neutrino flux, whereas in a fully multidimensional (FMD) transport scheme all three flux components are evolved. Because of its parallel efficiency, RbR+ is employed in several recent simulations (Takiwaki et al., 2014; Lentz et al., 2015; Summa et al., 2018).

There have been speculations about the influence of the RbR+ approximation on the neutrino-heating mechanism in 2D (see Section 3.1.2 for an extensive summary). In particular, the RbR+ approximation has been shown to foster shock revival in 2D models that featured strong SASI-sloshing modes in the polar directions, when compared to a FMD transport scheme (Skinner et al., 2016; Just et al., 2018). However, hydrodynamic instabilities in 2D are constrained by the symmetry assumption, which even prevents the growth of some modes of instabilities, like the spiral mode of SASI (Blondin and Shaw, 2007). Furthermore, the transport of turbulent energy in 2D simulations has been found to be unphysical (Hanke et al., 2012; Couch, 2013; Couch and Ott, 2015). For these reasons, the self-consistent modeling of CCSNe must ultimately proceed to the general 3D case, and it is therefore indispensable to assess the influence of the RbR+ approximation on the neutrino-heating mechanism also in 3D simulations.

LESA Further speculations about the RbR+ approximations concern the lepton-number emission self-sustained asymmetry (LESA), a phenomenon that was first found by Tamborra et al. (2014a) in their 3D simulations with RbR+ transport. The key feature of LESA is a global, dipolar asymmetry

of the lepton-number flux, i.e. the hemispheric number-flux difference of electron neutrinos (ν_e) minus electron antineutrinos ($\bar{\nu}_e$). In particular, the dipolar component of the lepton-number flux can rise to values as large as the monopole component for some models, and the direction of the dipole vector remains relatively stable over time periods of tens to hundreds of milliseconds. LESA has possible consequences on the nucleosynthesis of the neutrino-heated ejecta and on the neutron-star kick velocities (Janka et al., 2016); the detailed impact of LESA on these aspects, however, needs still to be determined in future studies.

Shortly after the discovery of LESA, Sumiyoshi et al. (2015) speculated that it may be an artifact of the RbR+ approximation. Only in recent studies, O'Connor and Couch (2018b) and Vartanyan et al. (2019a) have ended these speculations by identifying LESA also in some of their 3D simulations with FMD neutrino transport. Nevertheless, the influence of the RbR+ approximation on the effects of LESA remained to be examined.

Overview of This Thesis

Goals In this thesis, we assess the influence of the RbR+ approximation for neutrino transport on the delayed neutrino-heating mechanism of CCSNe. After previous studies in axial symmetry found the RbR+ approximation to facilitate shock revival for some progenitor stars, we satisfy the need for an evaluation in the general 3D case by comparing—for the first time—self-consistent 3D simulations with RbR+ transport and a FMD scheme that does not make use of RbR+. To this end, we conducted in total eight 3D simulations with angular resolutions of roughly 4° ("low resolution") and 2° ("high resolution") for an exploding $9\,\mathrm{M}_\odot$ progenitor model and a $20\,\mathrm{M}_\odot$ model that does not explode with the employed simplified set of neutrino rates. Furthermore, we analyze our set of 3D simulations for LESA, a phenomenon that was found by Tamborra et al. (2014a) in their 3D simulations using RbR+ transport. We use the unique possibility to evaluate the dependencies of LESA on the employed neutrino-transport method (FMD or RbR+) and reveal a global, dipolar flow pattern in the neutron star that is associated with LESA.

Organization We start in Chapter 2 by describing the framework that we use to simulate CCSNe, including detailed expressions of the underlying equations of neutrino radiation transport (Section 2.2), an overview of the numerical methods that we use to solve these equations (Section 2.4), a comparison of the RbR+ approximation and the FMD scheme (Section 2.5), as well as the setup of our 2D and 3D simulations (Section 2.6). We continue in Chapter 3 with a recapitulation of previous studies employing various neutrino-transport approximations and investigating the influence of RbR+ in 2D simulations (Section 3.1), followed by a summary of our own 2D simulations (Section 3.2). The main results for our comparison of 3D simulations with RbR+ and FMD neutrino transport are discussed in Section 3.3 for the $20\,\mathrm{M}_\odot$ progenitor model and Section 3.4 for the $9\,\mathrm{M}_\odot$ progenitor model, concluded by a summary in Section 3.5. In Chapter 4, we present the analysis of our 3D models for LESA. Starting with a general overview of the LESA phenomenon in Section 4.1, we discuss the key features of LESA that we find in our 3D simulations in Section 4.2, with a focus on the differences between models with RbR+ and FMD transport methods. In Section 4.3, we analyze the flow patterns in the neutron star that are associated with LESA, and in Section 4.4 we briefly summarize our attempt in Glas et al. (2019a) to connect the LESA phenomenon to Chandrasekhar's linear theory of thermal instability in spherical shells (Chandrasekhar, 1961). After summarizing our findings for LESA in Section 4.5, we conclude this thesis in Chapter 5.

Chapter 2.

Core-Collapse Supernova Simulations with the Alcar Code

This chapter deals with the basic principles of our CCSN simulations, which were conducted with the Aenus-Alcar[1] code (Obergaulinger, 2008; Just et al., 2015, 2018). In these simulations, the evolution of the stellar fluid is modeled by the hydrodynamics equations (see Section 2.1), and the neutrino transport is approximated by a system of two-moment equations (see Section 2.2). The interactions between neutrinos and the stellar matter are described in Section 2.3. We use Godunov-type finite-volume methods in spherical polar coordinates to solve both the equations of hydrodynamics and neutrino transport (see Section 2.4). The Alcar code is capable of employing both the FMD neutrino-transport scheme and the RbR+ approximation (see Section 2.5), which is a great advantage for the main goal of this thesis—the comparison of 3D simulations with FMD and RbR+ transport—because complicated code-to-code comparisons (concerning all other aspects) can be avoided. Finally, the setup of our simulations is discussed in Section 2.6. For a detailed description of the Alcar code and its application to CCSN simulations we refer the reader to Just et al. (2015) and Just et al. (2018). The following sections (in particular Sections 2.1 to 2.5) represent a summary of these two publications.

Throughout this thesis, we employ spherical polar coordinates for variables both in position space (with radius r, polar angle θ, and azimuthal angle ϕ) and in momentum space (with neutrino energy ε, polar angle ϑ, and azimuthal angle φ). Depending on the context, the vector indices i, j, and k run over the components of either position space or momentum space, respectively.

2.1. Equations of Hydrodynamics

The equations of hydrodynamics describe the temporal evolution of the stellar fluid. They are based on conservation laws for the baryonic density ρ, the electron fraction Y_e, the momentum density ρv^i (with v^i being the fluid velocity), and the total (i.e., internal plus kinetic) energy density e_t:

$$\partial_t \rho + \nabla_j \left(\rho v^j\right) = 0, \tag{2.1a}$$

$$\partial_t \left(\rho Y_e\right) + \nabla_j \left(\rho Y_e v^j\right) = Q_\mathrm{N}, \tag{2.1b}$$

$$\partial_t \left(\rho v^i\right) + \nabla_j \left(\rho v^i v^j + P_\mathrm{g}\right) = -\rho \nabla^i \phi_\mathrm{g} + Q^i_\mathrm{M}, \tag{2.1c}$$

$$\partial_t e_\mathrm{t} + \nabla_j \left(v^j \left(e_t + P_\mathrm{g}\right)\right) = -\rho v_j \nabla^j \phi_\mathrm{g} + Q_\mathrm{E} + v_j Q^i_\mathrm{M}. \tag{2.1d}$$

[1] The Aenus-Alcar code consists of a hydrodynamics module called Aenus (Obergaulinger, 2008), and a neutrino-transport module called Alcar (Just et al., 2015), with Alcar being the short form of "**a**lgebraic **l**ocal **c**losure **a**pproach for **r**adiation". Throughout this thesis, however, the name Alcar refers to the complete Aenus-Alcar code.

Here, ∂_t and ∇_i represent derivatives with respect to time and position, respectively. The electron fraction is defined by the difference of electron number n_{e^-} and positron number n_{e^+}, divided by the number of baryons n_B, i.e.,

$$Y_e = \frac{n_{e^-} - n_{e^+}}{n_\mathrm{B}}. \tag{2.2}$$

The gravitational self-interaction of the stellar matter enters the hydrodynamics equations through source terms that depend on the gravitational potential ϕ_g. For the calculation of ϕ_g we solve Poisson's equation, assuming Newtonian gravity but taking into account general-relativistic corrections as described by Marek et al. (2006, case A). The gravitational potential is obtained from spherically averaged radial profiles, i.e. we assume spherical symmetry for ϕ_g. The hydrodynamics equations are closed by a microphysical equation of state, which expresses the gas pressure P_g as a function of ρ, Y_e, and the internal energy. For this study, we employ the "SFHo" equation of state by Steiner et al. (2013), which we extended to a minimum temperature of 10^{-3} MeV to describe also the low-temperature regions that we encounter in a low-mass progenitor model. The neutrino-matter interactions are included in the hydrodynamics equations by source terms for the electron number (Q_N), momentum (Q^i_M), and total energy (Q_E). The calculation of the source terms is described in Section 2.3 (see, in particular, Equations (2.21)), including a list of all neutrino interactions that are taken into account (see Table 2.1). The equations of hydrodynamics are a system of hyperbolic differential equations, which we solve by Godunov-type finite-volume methods. The detailed numerical methods are described in Section 2.4.

2.2. Two-Moment Neutrino Radiation Transport

In this section, we derive the equations of two-moment neutrino radiation transport. In general, two-moment schemes evolve the energy density and energy-flux density of neutrinos, which correspond to the first two angular moments of the specific intensity. The system of moment equations is closed by relating the high-order moments (like the neutrino-pressure tensor) to the low-order moments via an analytic expression. The derivations in this section are mostly based on the publications by Munier and Weaver (1986a,b) and Just et al. (2015, 2018).

2.2.1. Radiation Transfer Equation

In general, the transport of neutrinos is governed by the Boltzmann equation, which describes the temporal evolution of the particle distribution function f in the six-dimensional phase space. In the framework of neutrino radiation transport, we instead often use the specific intensity $I = I(t, \boldsymbol{x}, \boldsymbol{n}, \varepsilon)$, depending on time t, position $\boldsymbol{x}$, neutrino energy ε, and the unit vector in momentum direction $\boldsymbol{n}$. It is related to the distribution function by (compare Munier and Weaver 1986a, Equation (173), where $\nu = \varepsilon/h$ is the neutrino frequency)

$$I(\boldsymbol{x}, t, \boldsymbol{n}, \varepsilon) = \frac{h}{c^2}\, \varepsilon^3\, f(\boldsymbol{x}, t, \boldsymbol{n}, \varepsilon), \tag{2.3}$$

with the speed of light c, and Planck's constant h. The evolution of I in time is governed by the radiation transfer equation (Munier and Weaver, 1986b, Equation (112)),

$$\frac{1}{c}\partial_t I + n^i\, \nabla_i I = [I]_\mathrm{coll}\,, \tag{2.4}$$

which corresponds to the Boltzmann equation assuming no external field and a neutrino velocity of c. The collision term on the right hand side of Equation (2.4) includes all source terms describing the interactions between neutrinos and matter.

In the context of CCSN simulations it is convenient to solve Equation (2.4) in a mixed-frame approach, in which spatial coordinates (concerning $\boldsymbol{x}$) are defined in the lab frame (short for laboratory frame; often referred to as "Eulerian frame"), and momentum space coordinates (concerning $\boldsymbol{n}$ and ε) are defined in the co-moving frame of the stellar fluid (often referred to as "Lagrangian frame" or "fluid frame"). Because the distribution function is isotropic in the co-moving frame, we can exploit symmetries in the collision integral and, thus, describe the source terms in a much simpler way. After performing the transformations into the co-moving frame (accurate to order v/c), the radiation transfer equation in the mixed-frame approach reads (compare Just et al. 2015, Equation (4); Munier and Weaver 1986b, Equation (153))

$$\begin{aligned}
&\frac{1}{c}\partial_t I + \frac{v_i n^i}{c^2}\partial_t I + n^j \nabla_j I + \frac{v^j}{c}\nabla_j I \\
&- \partial_\epsilon \left[I\epsilon \left(\frac{a_i n^i}{c^2} + \frac{1}{c} n^j n^k \nabla_j v_k \right) \right] \\
&+ \nabla_{n,i} \left[I \left(\frac{a_j n^j}{c^2} n^i - \frac{a^i}{c^2} + \frac{1}{c} n^i n^j n^k \nabla_j v_k \right. \right. \\
&\qquad \left. \left. - \frac{1}{c} n^j \nabla_j v^i - \Gamma^i{}_{jl} n^j n^l - \frac{1}{c} \Gamma^i{}_{jl} n^l v^j \right) \right] \\
&+ I \left[2\frac{a_i n^i}{c^2} + \frac{1}{c}\nabla_i v^i + \Gamma^i{}_{il} n^l + \frac{1}{c} n^j n^k \nabla_j v_k \right] = [I]_{\text{coll}} \,.
\end{aligned} \tag{2.5}$$

Here, $\Gamma^i{}_{jk}$ are the Christoffel symbols associated with the spatial coordinates, $\boldsymbol{a} = \partial_t \boldsymbol{v}$ is the particle acceleration, and $\nabla_{n,i}$ is the derivative in momentum space.

2.2.2. Angular Moments and Evolved Moment Equations

Instead of solving Equation (2.5) directly, we construct the angular moments of the specific intensity by integrating over the solid angle in momentum space[2] $\mathrm{d}\Omega_n$,

$$E = \frac{1}{c} \int \mathrm{d}\Omega_n \; I, \tag{2.6a}$$

$$F^i = \int \mathrm{d}\Omega_n \; I \; n^i, \tag{2.6b}$$

$$P^{ij} = \frac{1}{c} \int \mathrm{d}\Omega_n \; I \; n^i n^j, \tag{2.6c}$$

$$Q^{ijk} = \int \mathrm{d}\Omega_n \; I \; n^i n^j n^k. \tag{2.6d}$$

We restrict ourselves here to the first four moments, but the integration scheme of Equations (2.6) could, in principle, be continued until one ends up with an infinite series of angular moments. We identify E with the neutrino energy density (zeroth moment), F^i with the neutrino energy-flux density (first moment), and P^{ij} with the neutrino pressure tensor (second moment). In Appendix A, we provide for the sake of completeness also the expressions for the energy-integrated moments, together with the corresponding transformations into the lab frame.

By analogy with Equations (2.6a) and (2.6b), the first two angular moments of the radiation transfer equation (accurate to order v/c) are obtained by integrating Equation (2.5) over $\mathrm{d}\Omega_n$ and

[2] We distinguish between the solid angle in position space, $\mathrm{d}\Omega = \sin\theta \, \mathrm{d}\theta \, \mathrm{d}\phi$, and the solid angle in momentum space, $\mathrm{d}\Omega_n = \sin\vartheta \, \mathrm{d}\vartheta \, \mathrm{d}\varphi$.

dropping terms that are effectively of order v^2/c^2 (compare Just et al. 2015, Equations (7a) and (7b)),

$$\partial_t E + \nabla_j \left(F^j + v^j E \right) + P^{ij} \nabla_i v_j - \partial_\varepsilon \left(\varepsilon P^{ij} \nabla_i v_j \right) = C_E, \tag{2.7a}$$

$$\partial_t F^i + \nabla_j \left(c^2 P^{ij} + v^j F^i \right) + F^j \nabla_j v^i - \partial_\varepsilon \left(\varepsilon Q^{ijk} \nabla_j v_k \right) = C_F^i. \tag{2.7b}$$

Here, C_E and C_F^i correspond to the zeroth and first moment of the collision integral, respectively. Detailed expressions for C_E and C_F^i can be found in Equations (2.17).

In order to take into account general-relativistic redshift and time dilation effects in the moment equations, we correct Equations (2.7) by including dependencies on the lapse function α. In particular, when compared to the general-relativistic moment equations (see, e.g., Shibata et al. 2011 and Cardall et al. 2013), we assume the lapse function to be the only general-relativistic metric component. The corrected moment equations read (compare Just et al. 2018, Equations (3a) and (3b))

$$\begin{aligned} \partial_t E + \nabla_j \left(\alpha F^j + v^j E \right) + P^{ij} \nabla_i v_j + F^i \nabla_i \alpha \\ - \partial_\varepsilon \left[\varepsilon \left(P^{ij} \nabla_i v_j + F^i \nabla_i \alpha \right) \right] = \alpha \, C_E, \end{aligned} \tag{2.8a}$$

$$\begin{aligned} \partial_t F^i + \nabla_j \left(\alpha c^2 P^{ij} + v^j F^i \right) + F^j \nabla_j v^i + c^2 E \nabla^i \alpha \\ - \partial_\varepsilon \left[\varepsilon \left(Q^{ijk} \nabla_j v_k + c^2 P^{ij} \nabla_j \alpha \right) \right] = \alpha \, C_F^i. \end{aligned} \tag{2.8b}$$

The lapse function is calculated by integrating the general relativistic Euler equation (see, for example, Rampp and Janka 2002, Section 3.7.2),

$$\frac{\partial \ln \alpha}{\partial r} = - \frac{1}{\rho c^2 + e_{\mathrm{int}} + p} \left(\frac{\partial p}{\partial r} - \frac{Q_{\mathrm{M}}}{\Gamma} \right), \tag{2.9}$$

from the surface to the center. Here, e_{int} is the internal energy density. At the surface, we apply the boundary condition $\alpha = \Gamma$ (van Riper, 1979) with the metric function Γ (see Rampp and Janka 2002).

The Equations (2.8) represent the system of two-moment neutrino-transport equations that are solved in the Alcar code. Instead of evolving separate equations for the higher moments P^{ij} and Q^{ijk}, which also appear in Equations (2.8), we truncate the (otherwise infinite) series of moment equations via a closure relation (see next section). Essentially, by integrating over the solid angle in momentum space and introducing a closure relation, the dimensionality of the radiation transfer equation (2.4) is effectively reduced by two, because the dependencies on the momentum space angles ϑ and φ are eliminated. While two-moment closure schemes (often called "M1 schemes" in the literature) evolve the first two moments (i.e., the energy density and energy-flux density of neutrinos), other schemes truncate the system of equations at a different order. For example, in flux-limited diffusion schemes (see, e.g., Bruenn 1985; Bruenn et al. 2013; Zhang et al. 2013) the energy-flux density is not separately evolved, but is obtained from the gradient of the energy density.

2.2.3. Analytical Closure Relation

The system of two-moment equations (2.8) describes the evolution of the first two moments, E and F^i. Instead of solving separate equations for the higher moments P^{ij} and Q^{ijk}, which also appear

in Equations (2.8), we introduce an analytical relation to close the system of moment equations. In the ALCAR code, this analytical relation expresses the higher moments P^{ij} and Q^{ijk} as functions of the evolved first two moments E and F^i, i.e.,

$$P^{ij} = P^{ij}(E, F^i), \tag{2.10a}$$

$$Q^{ijk} = Q^{ijk}(E, F^i). \tag{2.10b}$$

The closure for the neutrino-pressure tensor P^{ij} can be parametrized as (see Just et al. 2015, Equation (30); but also Levermore 1984 and Pennisi and Trovato 1987)

$$P^{ij} = E\left(\frac{1-\chi}{2}\delta^{ij} + \frac{3\chi-1}{2}n_F^i n_F^j\right), \tag{2.11}$$

with the Kronecker delta δ^{ij}, the normalized flux direction n_F^i,

$$n_F^i = \frac{F^i}{|\boldsymbol{F}|}, \tag{2.12}$$

and a parameter χ, which corresponds to the generalization of the Eddington factor. Similarly, the closure for the third moment Q^{ijk} can be parametrized as (see Just et al. 2015, Equation (32); but also Pennisi 1992)

$$Q^{ijk} = cE\left[\frac{f-q}{2}\left(n_F^i\delta^{jk} + n_F^j\delta^{ik} + n_F^k\delta^{ij}\right) + \frac{5q-3f}{2}n_F^i n_F^j n_F^k\right]. \tag{2.13}$$

Here, q is a parameter, and f is the flux factor,

$$f = \frac{|\boldsymbol{F}|}{cE}. \tag{2.14}$$

The detailed expressions for both χ and q depend on the choice of the closure relation. For this study, we use the analytical closure by Minerbo (1978), which is based on the principle of maximum entropy from statistical mechanics. In a study of the radiation field around spherically symmetric proto-neutron star models, Murchikova et al. (2017) found the closure by Minerbo (1978, "ME" in their terminology) to yield better results than other closures in most cases and, thus, they conclude that it is the most attractive closure for problems involving neutrino transport around proto-neutron stars. Using the expressions from Minerbo (1978), we obtain (see also Just et al. 2015, Equation (28a))

$$\chi(f) = \frac{1}{3} + \frac{1}{15}\left(6f^2 - 2f^3 + 6f^4\right), \tag{2.15}$$

and (see the derivation by Just et al. 2015, Equation (33) and Appendix A)

$$q(f) = \frac{f}{75}\left(45 + 10f - 12f^2 - 12f^3 + 38f^4 - 12f^5 + 18f^6\right). \tag{2.16}$$

2.3. Neutrino-Matter Interactions

In this section, we describe the neutrino-matter interactions that we include in our simulations. After providing an overview of the neutrino interactions in Section 2.3.1, we discuss some implementation details in Section 2.3.2, and explain the coupling of the interaction source terms to the hydrodynamics equations in Section 2.3.3.

Table 2.1.: Neutrino interactions included in our simulations. The top part of the table lists all neutrino interactions, divided into groups of absorption and emission processes, scattering, pair production and annihilation, and nucleon-nucleon bremsstrahlung. The symbols denote neutrons (n), protons (p), nucleons (N, either n or p), heavy nuclei with nucleon number (A) and proton number (Z), electrons (e^-), positrons (e^+), electron neutrinos (ν_e), electron antineutrinos ($\bar{\nu}_e$), heavy-lepton neutrinos (ν_x), and any neutrino kind (ν_i). In the bottom part of the table, we provide comments and the corresponding references for the neutrino interactions (compare the numbers in square brackets).

Absorption and emission (ν_e and $\bar{\nu}_e$ only)			
$n + \nu_e$	$\rightleftharpoons$	$p + e^-$	[1], [2]
$p + \bar{\nu}_e$	$\rightleftharpoons$	$n + e^+$	[1], [2]
$(\mathrm{A}, \mathrm{Z}) + \nu_e$	$\rightleftharpoons$	$(\mathrm{A}, \mathrm{Z}+1) + e^-$	[1]
$(\mathrm{A}, \mathrm{Z}) + \bar{\nu}_e$	$\rightleftharpoons$	$(\mathrm{A}, \mathrm{Z}-1) + e^+$	[1]
Scattering			
$n + \nu_i$	$\rightleftharpoons$	$n + \nu_i$	[1], [2]
$p + \nu_i$	$\rightleftharpoons$	$p + \nu_i$	[1], [2]
$(\mathrm{A}, \mathrm{Z}) + \nu_i$	$\rightleftharpoons$	$(\mathrm{A}, \mathrm{Z}) + \nu_i$	[1], [3]
$e^\pm + \nu_i$	$\rightleftharpoons$	$e^\pm + \nu_i$	[4], [5]
Pair production and annihilation (ν_x only)			
$e^- + e^+$	$\rightleftharpoons$	$\nu_x + \nu_x$	[6], [8]
Bremsstrahlung (ν_x only)			
$\mathrm{N}_1 + \mathrm{N}_2$	$\rightleftharpoons$	$\mathrm{N}_1 + \mathrm{N}_2 + \nu_x + \nu_x$	[7], [8]

References

[1] Bruenn (1985); Mezzacappa and Bruenn (1993)
[2] Weak-magnetism and nucleon-recoil corrections (Horowitz, 2002)
[3] Ion-screening corrections (Bruenn and Mezzacappa, 1997; Horowitz, 1997)
[4] Yueh and Buchler (1977); Bruenn (1985); Cernohorsky (1994)
[5] Damping of source terms for $\rho > 5 \times 10^{12}\,\mathrm{g\,cm^{-3}}$ (O'Connor, 2015)
[6] Bruenn (1985); Pons et al. (1998)
[7] Hannestad and Raffelt (1998)
[8] Simplified description (like absorption and emission, see O'Connor 2015)

2.3.1. Overview

Table 2.1 provides an overview of all neutrino-matter interactions for the three different evolved neutrino species: electron neutrinos ν_e, electron antineutrinos $\bar{\nu}_e$, and a third species ν_x that represents all heavy-lepton neutrinos. The set of interactions contains absorption and emission processes of neutrinos both by nucleons (i.e., neutrons and protons) and by nuclei. Because absorption and emission of heavy-lepton neutrinos are suppressed due to the large rest mass of muon and tau leptons, we include these processes only for electron-type neutrinos, ν_e and $\bar{\nu}_e$, respectively (see, however, Bollig et al. 2017, who demonstrate the possible influence of muons in 2D CCSN simulations). We further take into account the following scattering processes for all three neutrino species: isoenergetic scattering of neutrinos on nucleons, coherent scattering of neutrinos on nuclei

with ion-screening corrections due to medium correlations (Bruenn and Mezzacappa, 1997; Horowitz, 1997), and inelastic scattering of neutrinos off electrons e^- and positrons e^+ (Yueh and Buchler, 1977; Bruenn, 1985; Cernohorsky, 1994). All interactions of neutrinos with nucleons (i.e., absorption, emission, and scattering) include weak-magnetism and nucleon-recoil corrections (Horowitz, 2002). Detailed information about the calculation of all interactions with nucleons and nuclei can be found in the publications by Bruenn (1985) and Mezzacappa and Bruenn (1993). For neutrino scattering off electrons and positrons we follow a suggestion by O'Connor (2015) in damping the source terms at densities larger than $5 \times 10^{12}\,\mathrm{g\,cm^{-3}}$ (see Section 2.3.2 for details). The heavy-lepton neutrinos are produced (and annihilated) in neutrino-antineutrino pairs via nucleon-nucleon bremsstrahlung (Hannestad and Raffelt, 1998) and e^-e^+ annihilation (and creation) (Bruenn, 1985; Pons et al., 1998). Both the nucleon-nucleon bremsstrahlung and the e^-e^+-pair processes are implemented with a simplified description, in which these interactions are treated similarly to absorption and emission terms (following O'Connor 2015; see Section 2.3.2 for details). Because the production and annihilation of electron-type neutrinos are by far dominated by the emission and absorption on nucleons and nuclei, we include neither the nucleon-nucleon bremsstrahlung, nor the e^-e^+-pair processes for ν_e and $\bar{\nu}_e$.

2.3.2. Details of the Implementation

The neutrino interactions enter the moment equations (2.8) via the source terms C_E and C_F^i for the energy density and energy-flux density, respectively. These source terms can be separated into contributions from absorption, emission, and iso-energetic scattering processes (subscript "aes"), and from inelastic scattering processes (subscript "is"),

$$C_E = C_{E,\mathrm{aes}} + C_{E,\mathrm{is}}, \tag{2.17a}$$
$$C_F^i = C_{F,\mathrm{aes}}^i + C_{F,\mathrm{is}}^i. \tag{2.17b}$$

We follow the formalism of Bruenn (1985) and Rampp and Janka (2002) and rewrite the source terms $C_{E,\mathrm{aes}}$ and $C_{F,\mathrm{aes}}^i$ as functions of an effective absorption opacity κ_a (corrected for stimulated absorption) and an effective scattering opacity κ_s, (see also Just et al. 2018, Equations (A2a) and (A2b)),

$$C_{E,\mathrm{aes}} = c\kappa_\mathrm{a}\left(E^\mathrm{eq} - E\right), \tag{2.18a}$$
$$C_{F,\mathrm{aes}}^i = -c\left(\kappa_\mathrm{a} + \kappa_\mathrm{s}\right)F^i. \tag{2.18b}$$

Here, E^eq is the equilibrium energy density, given by the Fermi-Dirac distribution (see, e.g., Just et al. 2015, Equation (15)),

$$E^\mathrm{eq}(\varepsilon, \mu_\nu, T) = 4\pi\left(\frac{\varepsilon}{hc}\right)^3\left[\exp\left(\frac{\varepsilon - \mu_\nu}{k_\mathrm{B}T}\right) + 1\right]^{-1}, \tag{2.19}$$

for neutrinos with chemical potential μ_ν and energy ε, and for a fluid temperature T (with k_B being the Boltzmann constant).

The computation of the opacities κ_a and κ_s follows the explanations given in the appendix of Rampp and Janka (2002), but additionally includes corrections to interactions with nucleons due to weak magnetism and nucleon recoil (Horowitz, 2002). Furthermore, we use a simplified description for both the nucleon-nucleon bremsstrahlung and the e^-e^+-pair processes, which are treated as absorption and emission terms. Specifically, these two processes enter the absorption opacity by means of an isotropic emissivity (see O'Connor 2015 for details, in particular in their Section 2.6.2).

Similarly to O'Connor (2015), we include the nucleon-nucleon bremsstrahlung and the e^-e^+-pair processes only for heavy-lepton neutrinos, because the production and annihilation of ν_e and $\bar{\nu}_e$ are by far dominated by charged-current interactions (i.e., the emission off and the absorption on nucleons and nuclei).

For the calculation of the source terms $C_{E,\mathrm{aes}}$ and $C^i_{F,\mathrm{aes}}$ (Equations (2.18)), the opacities κ_a and κ_s are treated explicitly in time, i.e., they are computed from quantities that are given at the old time step. In contrast, the neutrino energy density E and energy-flux density F^i are treated implicitly in time, which means that we have to invert the system of equations to obtain values for E and F^i at the new time step. In most cases, the equilibrium energy density is calculated from quantities μ_ν and T defined at the old time step, i.e., E^eq is treated explicitly in time. However, in some rare cases where the values for E^eq strongly differ between two time steps, we obtain improved values for μ_ν and T by an intermediate, implicit step (see the appendix of Just et al. 2018 for details). In practice, we encounter strongly differing values for E^eq between two time steps only in regions of strong neutrino-matter coupling and, therefore, apply the intermediate step only for densities larger than $10^{14}\,\mathrm{g\,cm^{-3}}$.

In addition to the source terms for absorption, emission, and iso-energetic scattering processes, the source terms in Equations (2.17) also take into account contributions from the inelastic scattering of neutrinos off electrons and positrons. The corresponding source terms $C_{E,\mathrm{is}}$ and $C^i_{F,\mathrm{is}}$ are calculated explicitly in time to avoid computationally expensive inversions of the two-moment equations. In order to retain a stable evolution when the scattering rates become too high to be followed properly with an explicit treatment, we follow a suggestion by O'Connor (2015, inspired by Thompson et al. 2003) in damping the source terms for the inelastic scattering by a factor of

$$f_\mathrm{is} = \max\left[1, \left(\frac{\rho}{5\times10^{12}\,\mathrm{g\,cm^{-3}}}\right)^{\frac{3}{2}}\right]. \tag{2.20}$$

In other words, the source terms $C_{E,\mathrm{is}}$ and $C^i_{F,\mathrm{is}}$ are damped only for densities larger than $5\times10^{12}\,\mathrm{g\,cm^{-3}}$.

In the following, we briefly compare the set of neutrino interactions between this work and the study by Just et al. (2018), who conducted 2D CCSN simulations with the Alcar code, comparing different approximations and corrections to the neutrino physics. Our set of neutrino interactions corresponds to their "pp" and "rbr-pp" models, respectively, depending on whether the FMD or the RbR+ neutrino transport was employed. This means, in particular, than in contrast to the reference models of Just et al. 2018, we include nucleon-nucleon bremsstrahlung and the e^-e^+-pair processes ("pp" is the short form of pair processes) only for heavy-lepton neutrinos and with the aforementioned simplified description. However, we neither include strangeness corrections to the axial-vector coupling in neutral-current interactions (Horowitz 2002 and Horowitz et al. 2017; as in models "str" of Just et al. 2018), nor axial response corrections to the neutrino-nucleon scattering cross section due to many-body effects (Horowitz et al. 2017; as in models "mb" of Just et al. 2018). Moreover, in contrast to models "nones" and "norel" of Just et al. 2018, we do take into account inelastic neutrino-electron scattering as well as velocity-dependent and gravitational redshift terms.

2.3.3. Coupling to the Hydrodynamics Equations

The neutrino-matter interactions are included in the hydrodynamics equations (2.1) by source terms for the electron number (Q_N), momentum (Q^i_M), and total energy (Q_E). They are computed from the source terms C_E and C^i_F (Equations (2.17)) of the two-moment system for neutrino transport

via (see also Just et al. 2018, Equations (2a) to (2c))

$$Q_N = -\alpha\, m_\mathrm{B} \int (C_{E,\nu_e} - C_{E,\bar{\nu}_e})\, \varepsilon^{-1}\ \mathrm{d}\varepsilon, \tag{2.21a}$$

$$Q^i_M = -\alpha \frac{1}{c^2} \sum_\nu \int C^i_{F,\nu}\ \mathrm{d}\varepsilon, \tag{2.21b}$$

$$Q_E = -\alpha \sum_\nu \int C_{E,\nu}\ \mathrm{d}\varepsilon. \tag{2.21c}$$

Here, m_B is the atomic mass unit, and the sums run over all neutrino species ν with $\nu \in \{\nu_e, \bar{\nu}_e, \nu_x\}$.

2.4. Numerical Methods

In this section, we describe the numerical methods that we use to solve the equations of hydrodynamics (2.1) and the system of two-moment neutrino-transport equations (2.8). Both the hydrodynamics and neutrino-transport equations represent hyperbolic differential equations, which are commonly solved by conservative finite-volume methods. In these methods, the physical quantities are discretized as cell-volume averages, i.e., the discretized representation $\hat{u}$ of a quantity u in a cell with volume ΔV is given by

$$\hat{u} = \frac{1}{\Delta V} \int_{\Delta V} u\ \mathrm{d}V. \tag{2.22}$$

Using this representation, the divergence terms that appear in the differential equations can be rewritten as surface integrals (by means of Gauss's divergence theorem) over the interface fluxes between adjacent cells.

In the Alcar code, we use a Godunov-type (Godunov, 1959) finite-volume scheme to solve both the equations of hydrodynamics and the equations of neutrino transport. The cell-interface fluxes between adjacent cells are obtained by the approximate "HLLC" Riemann solver (Toro et al. 1994; based on the fundamental "HLL" two-wave solver by Harten et al. 1983). In the vicinity of coordinate-aligned shocks, we switch to the "HLLE" Riemann solver (Einfeldt 1988; Einfeldt et al. 1991; see also Toro 1997). To compute the cell-interface fluxes of a quantity u, the Riemann solver requires the values of u at the cell interfaces, which need to be reconstructed from the cell averages $\hat{u}$. For the reconstruction of the interface values, we employ the piecewise-parabolic method (PPM; Colella and Woodward 1984) in the cell-centered "PPM_5" version of Mignone (2014).

For the time integration of both the hydrodynamics and neutrino-transport equations we use an explicit, directionally unsplit second-order Runge-Kutta scheme, with the same time stepping for the two set of equations. The global time step Δt is constrained by the Courant-Friedrichs-Lewy condition (CFL; Courant et al. 1928). It is computed by

$$\Delta t = f_\mathrm{CFL} \times \min\left(\Delta t_\mathrm{hydro}, \Delta t_\mathrm{transport}\right), \tag{2.23}$$

where Δt_hydro and $\Delta t_\mathrm{transport}$ are the minimum time steps of the hydrodynamics and the neutrino-transport equations, respectively, and $f_\mathrm{CFL} \leq 1$ is the CFL factor.

For further details of the numerical methods that are employed in the Alcar code we refer the reader to the extensive documentation provided by Just et al. (2015, in particular Section 3).

2.5. FMD versus RbR+ Neutrino Transport

One of the main goals of this thesis is the comparison of 3D CCSN simulations with two different neutrino-transport methods: the FMD transport scheme on the one hand, and the RbR+

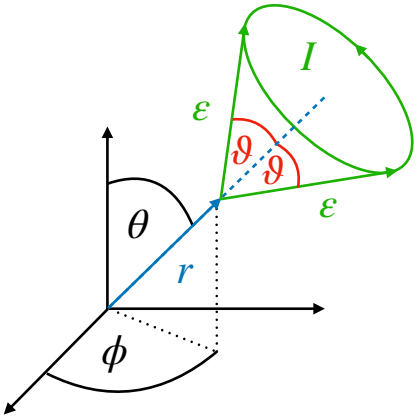

Figure 2.1.: Symmetry assumption of the RbR+ approximation (Rampp and Janka, 2002; Buras et al., 2006b). For RbR+ transport, the specific intensity I is assumed to be symmetric around the radial direction r of the spherical polar coordinate grid.

approximation on the other hand. For RbR+ transport (Rampp and Janka, 2002; Buras et al., 2006b), the specific intensity is assumed to be symmetric around the radial direction of the spherical polar coordinate grid (see the illustration in Figure 2.1). One direct consequence of the RbR+ approximation are vanishing non-radial flux components, F^θ and F^ϕ, and vanishing off-diagonal pressure-tensor elements, P^{ij} with $i \neq j$. For this reason, with the RbR+ approximation only the radial flux component F^r is evolved, while in the FMD transport scheme all three flux components F^r, F^θ, and F^ϕ are evolved (compare the moment equation for F^i in Equation (2.8b)). In the Alcar code, the FMD scheme is implemented as default transport method, and the RbR+ approximation can easily be employed by explicitly setting $F^\theta = F^\phi = 0$. Throughout this thesis, we use the advanced version[3] of RbR+ (Buras et al., 2006b), which means that we include the lateral neutrino-pressure contributions in the hydrodynamics equations (in particular, Equations (2.1c) and (2.1d)) for densities larger than $10^{12}\,\mathrm{g\,cm^{-3}}$ via the source term Q^θ_M (see the discussion in Buras et al. 2006b, Section 2.2.3, and Equation (18); but also Equation (5) in Just et al. 2018),

$$Q^\theta_{M,\mathrm{RbR+}} = -\frac{\alpha}{3}\sum_\nu \int \frac{1}{r\,\sin\theta}\,\partial_\theta E\,\mathrm{d}\varepsilon. \tag{2.24}$$

For densities smaller than $10^{12}\,\mathrm{g\,cm^{-3}}$ we set $Q^\theta_{M,\mathrm{RbR+}} = 0$. In contrast, in the FMD scheme we use the general expression from Equation (2.21b) to calculate Q^θ_M (independently of the density).

2.6. Setup of Simulations

In this section we describe the setup of our 2D and 3D CCSN simulations, including the settings of the neutrino-transport solver (Section 2.6.1), the grids and the numerical resolution employed in our runs (Section 2.6.2), a simplification ("1D core") that allows us to use a larger time step and hence to make our simulations consume less computational resources (Section 2.6.3), the initialization of our simulations (Section 2.6.4) together with the progenitor models used in this thesis (Section 2.6.5), and a summary of the set of eight 3D simulations that we use to analyze the differences between the neutrino-transport methods FMD and RbR+ in 3D (Section 2.6.6). Most contents of this section

[3]The original version of the transport approximation from Rampp and Janka (2002) is called ray-by-ray (RbR), and the advanced version that was introduced in Buras et al. (2006b) is called ray-by-ray-plus (RbR+).

Table 2.2.: Grid parameters for 2D and 3D simulations. We distinguish between "polar" (coarser resolution at the poles), "equatorial" (coarser resolution at the equator), and "uniform" (uniform resolution) angular grid structures. This table is taken from Glas et al. (2019b, Table 1).

	Label	Angular Grid Structure	$N_r \times N_\theta$ ($\times N_\phi$)
3D	L	polar	$320 \times 40 \times 80$
3D	H	polar	$640 \times 80 \times 160$
2D	pol/40	polar	320×40
2D	pol/80	polar	640×80
2D	equ/80	equatorial	640×80
2D	uni/80	uniform	640×80

(in particular, Sections 2.6.2 to 2.6.5) have already been published in Glas et al. (2019b, see also the information on already published material on page 73).

2.6.1. Neutrino Transport

Alcar's neutrino-transport module solves the system of energy-dependent two-moment equations (2.8), which describes the evolution of the energy density E and the energy-flux density F^i of neutrinos (see Section 2.2 for an extensive summary). We evolve E and F^i (both measured in the co-moving frame of the fluid) for three neutrino species: electron neutrinos ν_e, electron antineutrinos $\bar{\nu}_e$, and a third species ν_x that represents all four heavy-lepton neutrinos. For the discretization of the neutrino energy ε, we employ 15 bins that are logarithmically spaced in the interval $0 \leq \varepsilon \leq 400\,\mathrm{MeV}$. The discretization of the neutrino-transport equations and the hydrodynamics equations in position space is based on the same spatial grids (see next section).

2.6.2. Grids and Numerical Resolution

To assess the influence of numerical grid resolution, we vary the number of grid cells (N_r, N_θ, and N_ϕ, respectively). A summary for our 2D and 3D simulations can be found in Table 2.2. In general, we differentiate between "low" and "high" resolutions. For 2D simulations our naming convention is based on the number of lateral zones (i.e., "40" for low resolution, and "80" for high resolution), whereas for 3D simulations we simply abbreviate low ("L") and high ("H") resolutions. In both 2D and 3D simulations, the radial grid ranges from 0 to 10^9 cm and contains $N_r \in \{320, 640\}$ zones. The cell sizes in radial direction increase logarithmically, starting with 10^4 cm in the center of the star. In radial direction, we use a reflecting inner boundary (at $r = 0$) for all evolved quantities, and at the outer boundary (at $r = 10^9$ cm) we use an inflow condition for hydrodynamic quantities with time-independent values for density, infall velocity, and total energy (all obtained from the progenitor model) and prescribe a free outflow condition for the neutrinos.

In 3D simulations, the polar grid is composed of two large zones at each pole ($\theta = 0°$ and $\theta = 180°$, respectively) and $N_\theta - 4$ zones around the equatorial plane with equal sizes. For low-resolution grids with $N_\theta = 40$ zones (high with $N_\theta = 80$) the first cell measures 12° (10°) and the second cell 6° (4°), leading to a cell size of 4° (2°) for the remaining equally sized zones to cover the entire 180° range. Using this particular arrangement with coarser angular resolution at the poles, we are able to sustain a computationally affordable time step by avoiding exceedingly small cell sizes in azimuthal direction, which are proportional to $\sin\theta$, and which dictate the time step in our 3D simulations according to the CFL criterion. In azimuthal direction (relevant only in 3D), the grid cells have constant size over the whole 360° domain, leading to a cell size of 4.5° (2.25°) for

$N_\phi = 80$ ($N_\phi = 160$) zones. We use a reflecting boundary in lateral direction (at angles $\theta = 0°$ and $\theta = 180°$) for 2D and 3D simulations, and periodic boundary conditions in azimuthal direction (at the interface where $\phi = 0°$ or, equivalently, $\phi = 360°$) for 3D simulations.

In our 2D simulations, we assess the influence of the polar grid by varying the number and arrangement of angular grid cells. First, we performed 2D simulations on a polar grid with $N_\theta = 80$ uniformly distributed cells (labeled 'uni/80', see Table 2.2), leading to a polar grid resolution of 2.25°. Second, we tested the polar grid structure that we apply in the 3D simulations (with coarser angular resolution at the poles to alleviate time step constraints) also in 2D simulations (labeled 'pol/40' for $N_\theta = 40$, and 'pol/80' for $N_\theta = 80$ zones, respectively). Third, to further assess the influence of partially coarsened angular resolution, we conducted one 2D simulation on a polar grid with coarse resolution at the equator (labeled 'equ/80' with $N_\theta = 80$ zones). Specifically, the 'equ/80' grid consists of two 10°-zones symmetrically arranged around the equator ($\theta = 90°$), surrounded by two 4°-zones and 76 remaining zones with 2° to cover the entire 180° range.

2.6.3. 1D Core

In both 2D and 3D simulations, further constraints on the time step arise near the center of the spherical coordinate system, where cell sizes in lateral and azimuthal directions are smallest because of their dependence on the radial coordinate. We alleviate these constraints by evolving the innermost 10^6 cm in spherical symmetry ("1D core") and, thus, neglecting angular variations in the (spherically symmetric) innermost region of the proto-neutron star. This is an acceptable approach as long as the central core of $r < 10^6$ cm remains convectively stable, which is practically fulfilled until about 100 ms after bounce but can become marginally valid afterwards. While the violation of this condition has some influence on the evolution of proto-neutron star convection (see Section 4.3.3), the consequences are irrelevant for the results discussed in Chapter 3.

2.6.4. Initialization

Because there is no growth of hydrodynamic instabilities during core collapse until bounce, we simulate the collapse of the iron core in 1D and start our 2D and 3D simulations from the 1D data at 15 ms after core bounce. The 1D simulations are performed on the same radial grid (with $N_r = 640$) that we use in 2D and 3D simulations. To trigger hydrodynamic instabilities in the post-bounce phase, we initialize the multi-dimensional simulations with random seed perturbations in the density with an amplitude of 0.1 %.

2.6.5. Progenitor Models

We conducted CCSN simulations for two different non-rotating, solar-metallicity progenitor models (see Figure 2.2 for the radial profiles of density, electron fraction, radial velocity, and temperature at the onset of collapse). The first model, a 20 $M_\odot$ star from Woosley and Heger (2007, labeled s20 in the following), has already been extensively studied in literature. In 2D, both successful (Bruenn et al., 2016; Summa et al., 2016) and failed explosions (Skinner et al., 2016; Vartanyan et al., 2018) have been reported. Other groups have found successful and failed explosions in dependence on the simulation setup (e.g., the employed set of neutrino-interaction rates) when performing 2D (see, e.g., Bollig et al., 2017; Kotake et al., 2018; O'Connor and Couch, 2018a; Just et al., 2018) and 3D (Melson et al., 2015a) simulations of the s20 progenitor model. Thus, the s20 progenitor model seems to reside at the threshold between successful and failed explosions.

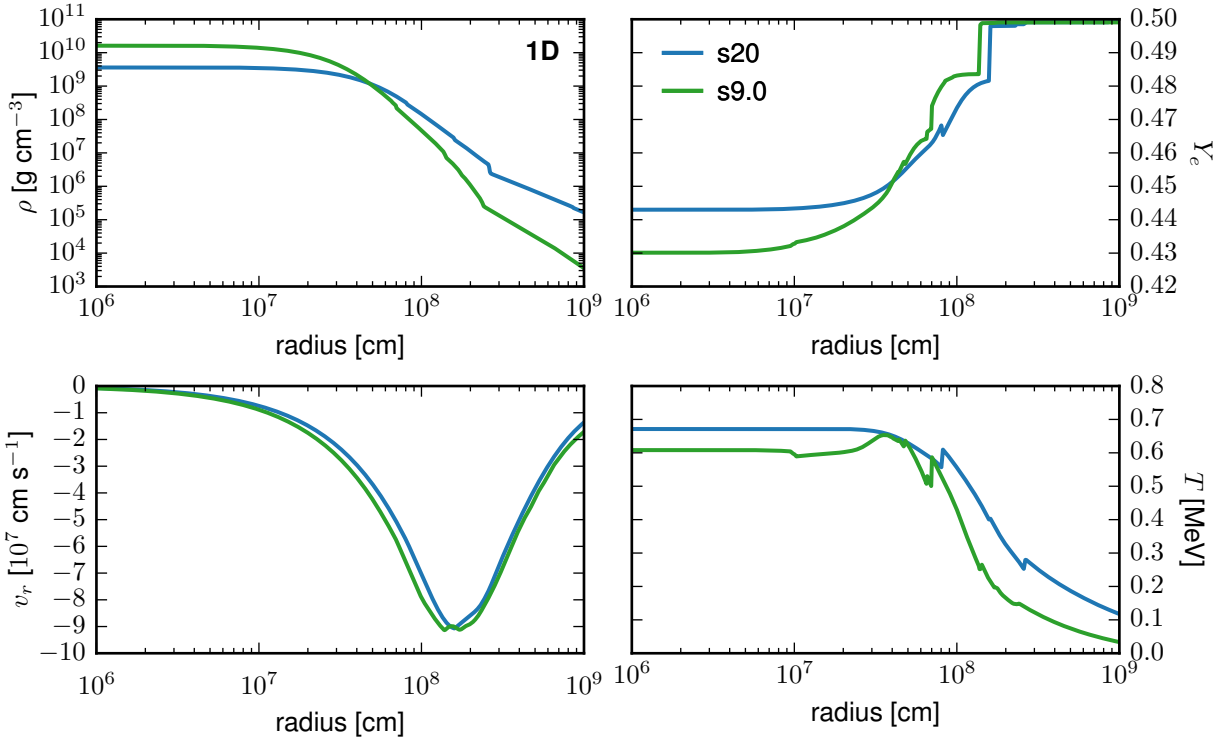

Figure 2.2.: Radial profiles at the onset of collapse of the spherically symmetric progenitor models s20 (blue lines) and s9.0 (green lines). We show, in dependence on the radius r, the densities ρ (top left), electron fractions Y_e (top right), radial velocities v_r (bottom left), and temperatures T (bottom right). This figure is a slightly rearranged version of Figure 1 from Glas et al. (2019b).

In order to additionally compare the explosion dynamics of 2D and 3D simulations, we chose the second progenitor model such that we expect robust successful explosions. The $9\,\mathrm{M}_\odot$ progenitor model from Woosley and Heger (2015, labeled s9.0 in the following)[4] has been shown to rather readily explode in 2D simulations by Radice et al. (2017) and Just et al. (2018). As most models at the low-mass end of iron-core progenitors, the s9.0 star exhibits a very steep density gradient at the edge of the degenerate core (see the radial density profile in Figure 2.2). As a consequence of the steep density gradient, the mass accretion rate drops rapidly during the first few 100 ms after core bounce, leading to favorable conditions for shock runaway. This can be seen from Figure 2.3, which shows the mass accretion rate, evaluated at a radius of $r = 400\,\mathrm{km}$, for the 1D simulations of the s9.0 and s20 progenitor models. Here, the mass accretion rate at any radius r is defined by the surface integral,

$$\dot{M}(r) = r^2 \int_{4\pi} \rho\, v_r\, \mathrm{d}\Omega, \tag{2.25}$$

with baryonic mass density ρ and radial velocity component v_r.

2.6.6. Overview of All 3D Simulations

For this work, we conducted in total eight 3D CCSN simulations. Table 2.3 summarizes the key features of these simulations: first, we performed simulations of two different progenitor models

[4] We use a slightly modified version of the $9\,\mathrm{M}_\odot$ progenitor model, which is described by Sukhbold et al. (2016). Data are available at `https://wwwmpa.mpa-garching.mpg.de/ccsnarchive/data/SEWBJ_2015/index.html`.

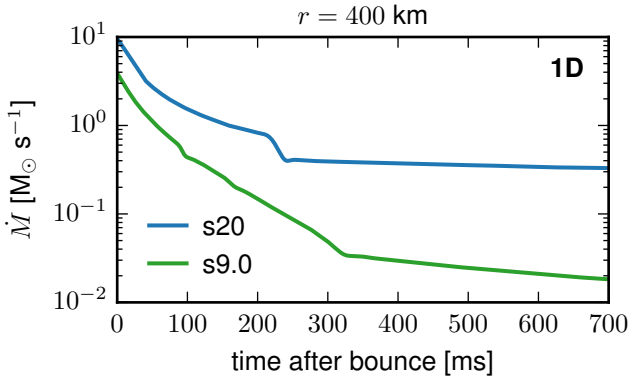

Figure 2.3.: Mass accretion rates as functions of the time after bounce for 1D simulations of the progenitor models s20 (blue line) and s9.0 (green line). The mass accretion rates $\dot{M}$ (see Equation (2.25)) are evaluated at a radius of $r = 400\,\mathrm{km}$. Note that $\dot{M}$ shows excellent agreement between 1D, 2D, and 3D simulations (until the time of shock revival in the case of successful explosions). This figure is a slightly rearranged version of Figure 2 from Glas et al. (2019b).

Table 2.3.: Summary of all 3D simulations. This table is taken from Glas et al. (2019a, Table 1).

Model Name	Progenitor	Transport	Resolution	$N_r \times N_\theta \times N_\phi$	Explosion
s20 FMD L	s20	FMD	L	$320 \times 40 \times 80$	no
s20 RbR+ L	s20	RbR+	L	$320 \times 40 \times 80$	no
s20 FMD H	s20	FMD	H	$640 \times 80 \times 160$	no
s20 RbR+ H	s20	RbR+	H	$640 \times 80 \times 160$	no
s9.0 FMD L	s9.0	FMD	L	$320 \times 40 \times 80$	yes
s9.0 RbR+ L	s9.0	RbR+	L	$320 \times 40 \times 80$	yes
s9.0 FMD H	s9.0	FMD	H	$640 \times 80 \times 160$	yes
s9.0 RbR+ H	s9.0	RbR+	H	$640 \times 80 \times 160$	yes

(s20 and s9.0; see Section 2.6.5), four simulations in each case. Second, we varied the numerical grid resolution (see Section 2.6.2) by changing the number of grid cells in radial (N_r), lateral (N_θ), and azimuthal (N_ϕ) direction for both progenitor models. For high resolution ("H"), we employ twice as many cells in each direction as compared to the low resolution ("L"). Third, we employed either the FMD neutrino-transport scheme, or made use of the RbR+ approximation (see Section 2.5). As the table indicates, we obtain successful explosions only for the s9.0 model (see Section 3.4), while all simulations of the s20 model fail to explode (see Section 3.3).

Chapter 3.

Simulations with FMD and RbR+ Neutrino Transport

One of the main goals of this thesis is to assess the influence of the RbR+ approximation on the delayed neutrino-heating mechanism in 3D CCSN simulations. For this purpose, we performed in total eight 3D simulations (see Table 2.3) with either the FMD neutrino-transport scheme or the RbR+ approximation. Before we discuss the results of our 3D simulations including the comparison of FMD and RbR+ neutrino-transport methods, we recapitulate the status of modeling the neutrino transport in CCSN on the basis of previous studies. We start with a brief overview of different transport approximations used in the literature (Section 3.1), with a focus on the influence of the RbR+ approximation in previous 2D simulations (Section 3.1.2), and complemented by a summary of the 2D simulations that we performed with our Alcar code (Section 3.2). Our main results regarding the comparison of 3D simulations are presented in Section 3.3 for the s20 progenitor model, and in Section 3.4 for the s9.0 progenitor model. We conclude the comparison of FMD and RbR+ neutrino transport in Section 3.5. The contents of this chapter have already been published in Glas et al. (2019b, see also the information on already published material on page 73).

3.1. Transport Methods in the Literature

In general, the transport of neutrinos is governed by the seven-dimensional (three spatial and three momentum dimensions plus time) Boltzmann transport equation describing the time evolution of the single-particle distribution function in the six-dimensional phase space (see Section 2.2.1). Solving it in its full complexity, for example by the discrete-ordinate (S_n) method (Sumiyoshi and Yamada, 2012), is currently computationally only feasible for selected temporal snapshots (Sumiyoshi et al., 2015), or for time-dependent axisymmetric hydrodynamic simulations with low resolution in momentum space (Nagakura et al., 2018). Alternatively, a Monte Carlo solver (Sedonu) has been applied for comparison with the S_n solutions on a 2D stationary background (Richers et al., 2017).

3.1.1. Overview of Transport Approximations

For this reason, a variety of approximations have been introduced to reduce the complexity of the full Boltzmann equation. The isotropic diffusion-source approximation is based on the decomposition of the neutrino distribution function into a trapped particle and a streaming particle component, which are separately evolved (Liebendörfer et al., 2009; Pan et al., 2016). Other schemes evolve the angular moments (i.e., integrals) of the specific intensity of neutrinos, instead of the particle phase-space distribution function itself. In flux-limited diffusion schemes, for example, the neutrino energy density (corresponding to the zeroth angular moment) is evolved, and the neutrino flux density (first moment) is obtained from the gradient of the energy density (Bruenn, 1985; Bruenn

et al., 2013; Zhang et al., 2013). Two-moment transport schemes, which also evolve the neutrino flux density, need to close the system of moment equations by relating the Eddington tensor (second moment) to the low-order moments (often called "M1" methods and used in many published codes; Foucart et al. 2015; Just et al. 2015; O'Connor and Couch 2018a; Skinner et al. 2016; Roberts et al. 2016; Kuroda et al. 2016; see also Section 2.2). Another widely-used approximation is RbR+ transport, which assumes the specific intensity to be symmetric around the radial direction of the spherical polar coordinate grid (Rampp and Janka, 2002; Buras et al., 2006b; Bruenn et al., 2013). A direct consequence of RbR+ are vanishing lateral and azimuthal (i.e., non-radial) flux components (see Section 2.5). All of these approximations require tests of their viability by mutual comparison and, ultimately, comparison with full Boltzmann solutions.

3.1.2. Influence of the RbR+ Approximation

There have been speculations about the influence of RbR+ on the neutrino-heating mechanism in 2D, mostly based on studies that neglect time-dependent effects, leaving the temporal evolution unclear. Dolence et al. (2015) analyzed neutrino fluxes based on a temporal snapshot of a two-dimensional CCSN simulation. They found larger angular variations of the radiation fluxes for RbR+ compared to their multi-group, flux-limited diffusion scheme in 2D, and they speculated that RbR+ might exaggerate angular variations because of an unphysically high correlation between matter and the neutrino field. Another study by Sumiyoshi et al. (2015) investigated neutrino-heating rates in the gain layer (i.e. where neutrino-matter interactions result in net heating), based on temporal snapshots of 3D CCSN simulations. When comparing results from solving the Boltzmann equation directly to results with the RbR+ approximation, they found differences in the local heating rates of 20%. However, the rates integrated spatially over the gain layer differed by only 2% (a similar conclusion was reached by Buras et al., 2006b). A time-dependent investigation was carried out by Skinner et al. (2016), who performed self-consistent, two-dimensional CCSN simulations of the post-bounce phase of various progenitor models. They hypothesize that there may be an unphysically strong feedback between the axial sloshing of the standing accretion shock instability (SASI, Blondin et al., 2003) and the neutrino field, leading to explosions in axisymmetric simulations with RbR+ more readily, compared to applications employing a multi-group, fully multi-dimensional two-moment transport solver. In addition, Just et al. (2018) found the RbR+ approximation to be conducive to explosions in time-dependent 2D CCSN simulations in particular for models that exhibit violent activity of SASI, when compared to a fully multi-dimensional two-moment transport scheme. The 2D behavior, however, turned out to be highly stochastic and very sensitive to minor variations of the applied input physics, for which reason the 2D results were hard to interpret in a clear way.

So far, time-dependent studies have investigated the influence of RbR+ only in 2D simulations, in which hydrodynamical instabilities are constrained by the imposed symmetry axis. Furthermore, 3D simulations allow for different modes of instabilities (e.g. the spiral mode of the SASI, Blondin and Shaw, 2007), and they show a different transport of turbulent energy compared to the 2D case (Hanke et al., 2012; Couch, 2013; Couch and Ott, 2015).

For these reasons, it is indispensable to assess the influence of the neutrino-transport treatment on the heating mechanism also in time-dependent 3D simulations. We fulfill this need by comparing self-consistent, time-dependent CCSN simulations in 3D with a FMD neutrino-transport scheme and with the RbR+ approximation.

3.2. Summary of 2D Simulations

Before we start to discuss our main 3D results, we summarize in this section the results of our 2D simulations for the s20 and s9.0 progenitor models. We will make use of these results in Sections 3.3 and 3.4, where we will, i.a., compare 2D and 3D simulations. Since this thesis mainly focuses on 3D results, we refer the reader to Just et al. (2018), who performed a detailed comparison of 1D and 2D CCSN simulations using the Alcar code and varying the physics inputs in a large set of models. Their results regarding the comparison between FMD and RbR+ neutrino transport in 2D simulations are consistent with our 2D results summarized in this section.

Here, we present only a small sample of 2D simulations with either FMD neutrino transport or the RbR+ approximation. To assess the influence of grid resolution, we varied the number of radial and angular grid zones (the labels of our simulations contain the number of angular grid zones, see Section 2.6.2 and Table 2.2). For the s20 progenitor model, we also varied the type of the polar grid. Besides uniform angular cell spacing (labeled 'uni'), coarser resolution at the poles (labeled 'pol' and copying the lateral grid structure applied to 3D simulations to alleviate time step constraints) was tested. Moreover, we performed one simulation on a polar grid with coarser resolution at the equator (labeled 'equ'). Except for using different neutrino-transport methods and the aforementioned grid parameters, all physical and numerical inputs are identical in our simulations.

3.2.1. The s20 Model in 2D: FMD versus RbR+

We present an overview of all 2D simulations for the s20 progenitor model in Figure 3.1. The top panel of Figure 3.1 shows the temporal evolution of the angle-averaged shock radii R_{s}, which indicate successful shock revival for two of the RbR+ simulations between 400 ms and 500 ms after core bounce. In these simulations, shock revival occurs shortly after the Si/Si-O interface falls through the shock, leading to a significant drop in the mass accretion rate at ~ 200 ms (compare Figure 2.3). As the bottom left panel of Figure 3.1 shows, successful shock revival is accompanied by a drop in the neutrino luminosities, which is a direct consequence of the reduced mass accretion onto the neutron star. We define the luminosity L_ν for any neutrino species ν at a radius r in the co-moving frame of the stellar fluid by integrating over the radial neutrino flux $F_\nu^r(r)$ (see Equation (2.6b)),

$$L_\nu(r) = r^2 \int F_\nu^r(r)\ \mathrm{d}\varepsilon\ \mathrm{d}\Omega. \tag{3.1}$$

In contrast, non-exploding models exhibit almost constant neutrino luminosities after 200 ms post bounce (p.b.) because of continuing mass accretion. From the evolution of the shock radii we also conclude that none of the 2D simulations with FMD neutrino transport results in an explosion until at least 700 ms after bounce.

As already argued by Dolence et al. (2015) and Skinner et al. (2016), this discrepancy between 2D simulations with RbR+ and FMD neutrino transport may be explained by a stronger feedback between the neutrino field and the axial sloshing of the SASI in the case of the RbR+ approximation. For this reason, we analyzed the time-dependent neutrino-heating rates at the poles, and we found deviations from the angle-averaged values to be significantly larger in RbR+ simulations. We will come back to a discussion of this behavior in our comparison between differences of 2D and 3D heating rates (see Section 3.3). This analysis confirms that in 2D simulations with strong SASI sloshing along the axis, the RbR+ approximation can amplify local variations at the poles and, therefore, may lead to conditions that are more beneficial for shock revival than corresponding results with an FMD neutrino-transport scheme.

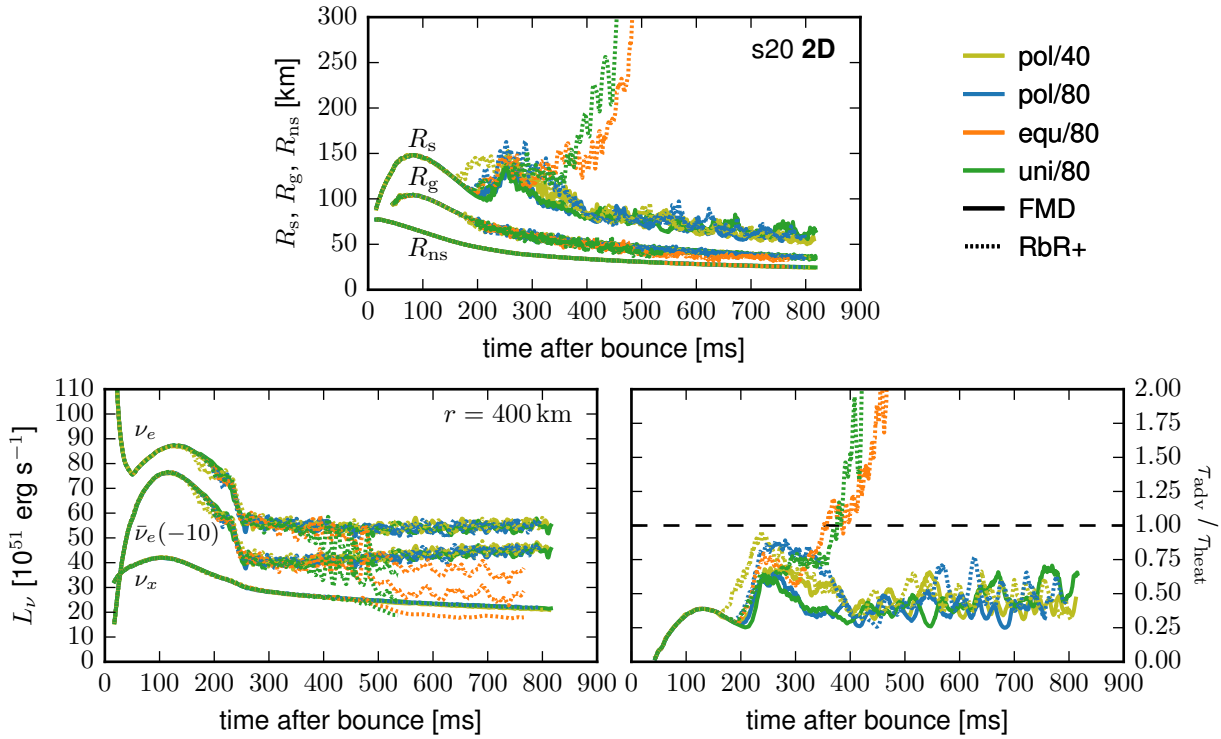

Figure 3.1.: Comparison of 2D simulations of the s20 progenitor model. We show, as functions of the time after bounce, the angle-averaged shock radii R_s, gain radii R_g, and neutron-star radii R_{ns} (all in the top panel; see labels), the neutrino luminosities L_ν (bottom left panel) for ν_e, $\bar{\nu}_e$, and ν_x (see labels), and the ratios of advection to heating timescales τ_{adv}/τ_{heat} (bottom right panel). The neutrino luminosities L_ν are evaluated at a radius of $r = 400$ km in the co-moving frame of the stellar fluid. The simulations differ in the neutrino-transport scheme (line style), and in the grid type and resolution (line color), see legend and Table 2.2 for an overview. Note that the neutrino luminosities and the ratios of advection to heating timescales were smoothed by running averages of 5 ms, and that some lines were shifted vertically to facilitate readability of the plot. These lines are marked with labels indicating the number by which they are shifted in units of the ordinate. This figure is a slightly rearranged version of Figure 3 from Glas et al. (2019b).

3.2.2. The s20 Model in 2D: Influence of the Polar Grid

In addition to discrepancies between 2D simulations with RbR+ and FMD neutrino transport, we find further differences in dependence on the polar grid. As the top panel of Figure 3.1 shows, we find successful shock revival only for RbR+ simulations with high angular grid resolution at the poles (labels 'uni/80' and 'equ/80'). In contrast, simulations that were performed on a grid with coarse polar resolution (labels 'pol/40' and 'pol/80') do not exhibit shock revival.

These discrepancies do not seem to be caused by differences in the time-dependent evolution of the angle-integrated neutrino quantities. Until the time when exploding models experience shock runaway, we find the neutrino luminosities, mean energies, and root mean square energies for all neutrino species to be in good agreement between all 2D simulations. The bottom left panel of Figure 3.1 shows only, for an example, the temporal evolution of the neutrino luminosities for all neutrino species.

To assess the influence of the angular grid resolution, we analyze the conditions for shock revival in our 2D simulations. Favorable conditions for an explosion arise when matter remains in the

gain layer for a time that is long enough for neutrinos to deposit sufficient energy to cause shock expansion. The total binding energy of matter in the gain layer, $E^{\mathrm{g}}_{\mathrm{tot}}$, is calculated from the specific internal energy e_{int}, specific kinetic energy $v^2/2$, and gravitational potential ϕ_{grav} as

$$E^{\mathrm{g}}_{\mathrm{tot}} = \int_{V_{\mathrm{gain}}} \rho \left(e_{\mathrm{int}} + \frac{v^2}{2} + \phi_{\mathrm{grav}} \right) \mathrm{d}V, \tag{3.2}$$

with velocity magnitude v. The volume of the gain layer, V_{gain}, encompasses the region from the average gain radius R_{g}, at which the angle-averaged net neutrino energy transfer turns from cooling into heating, to the angle-dependent shock radius $R_{\mathrm{s}}(\theta, \phi)$. The characteristic timescale for neutrino heating is then given by (Buras et al., 2006a; Müller et al., 2012b; Summa et al., 2018)

$$\tau_{\mathrm{heat}} = \frac{|E^{\mathrm{g}}_{\mathrm{tot}}|}{Q^{\mathrm{g}}_{\nu}}, \tag{3.3}$$

with Q^{g}_{ν} being the total neutrino-heating rate in the gain layer,

$$Q^{\mathrm{g}}_{\nu} = \int_{V_{\mathrm{gain}}} Q_E \, \mathrm{d}V. \tag{3.4}$$

Here, Q_E is the energy source term (energy exchange rate per volume), which couples the hydrodynamics and neutrino-transport equations (see Equation (2.21c)). The typical timescale for matter residing in the gain layer is given by the advection timescale, which we approximate (assuming steady-state conditions, Marek and Janka, 2009; Müller et al., 2012b) by

$$\tau_{\mathrm{adv}} \approx \frac{M_{\mathrm{g}}}{\dot{M}}, \tag{3.5}$$

with M_{g} being the total mass in the gain layer,

$$M_{\mathrm{g}} = \int_{V_{\mathrm{gain}}} \rho \, \mathrm{d}V, \tag{3.6}$$

and $\dot{M}$ being the mass accretion rate (see Equation (2.25)), evaluated at a radius of $r = 400\,\mathrm{km}$. In the case when the ratio of advection to heating timescale, $\tau_{\mathrm{adv}}/\tau_{\mathrm{heat}}$, exceeds unity, neutrino heating leads to beneficial conditions for shock expansion and may ultimately power an explosion (Janka, 2001; Thompson et al., 2005; Fernández, 2012).

We show the ratios $\tau_{\mathrm{adv}}/\tau_{\mathrm{heat}}$ in the bottom right panel of Figure 3.1. At 400 ms p.b., approximately when shock expansion sets in, we find exploding models to reach and exceed ratios of unity. Non-exploding simulations with RbR+ ('pol/40' and 'pol/80') exhibit slightly larger timescale ratios than the exploding models in the phase between 200 ms and 300 ms p.b., reaching values close to unity in this phase without, however, leading to successful shock revival. This strongly suggests that the explosions are caused by pole effects in models with fine resolution at the poles. In contrast, the values for $\tau_{\mathrm{adv}}/\tau_{\mathrm{heat}}$ stay well below unity in all (non-exploding) simulations with FMD neutrino transport. This confirms that RbR+ simulations exhibit more favorable conditions for successful shock revival than their FMD counterparts, but the differences between successful and unsuccessful RbR+ simulations (corresponding to high and low polar resolutions, respectively) are caused by pole effects.

In order to understand the subtle differences that determine the explosion behavior of some 2D RbR+ models while other RbR+ models fail to explode, we consider the evolution of relevant quantities in the immediate vicinity of the poles. We do not find any discriminative differences until

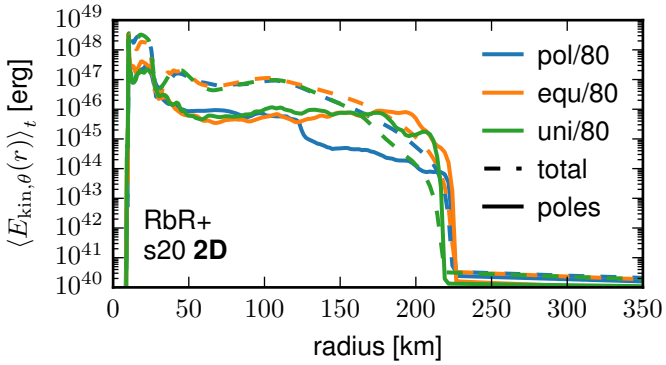

Figure 3.2.: Lateral kinetic energies $E_{\mathrm{kin},\theta}(r)$ for three different 2D RbR+ simulations of the s20 progenitor model. We show $E_{\mathrm{kin},\theta}(r)$, averaged over a time interval $t \in [300\,\mathrm{ms}, 350\,\mathrm{ms}]$, as functions of radius r. The total lateral kinetic energies (dashed lines) are obtained by integrating the kinetic energy over spherical shells at each radius r (see Equation (3.7)). For polar kinetic energies (solid lines), the shell integral includes only regions close to the poles with polar angles $\theta \in [0, 10°]$ and $\theta \in [170°, 180°]$. To facilitate comparison, the polar energies are rescaled by the ratio of the total shell volume to the polar volume at each radius. Notice that the radial grids of all three simulations are identical, so we can compare integrals over radial shells in a straightforward manner. This figure is a slightly rearranged version of Figure 4 from Glas et al. (2019b).

350 ms p.b. in the polar neutrino luminosities and energies, nor in the polar neutrino heating and cooling rates. However, we find turbulent motions at the poles to be suppressed in models with coarse polar resolution. This can be seen in Figure 3.2, where we plot the lateral kinetic energies near the poles for three different 2D high-resolution simulations with the RbR+ approximation. The lateral kinetic energy at a radius r is obtained by integrating over the radial shell volume $V_{\mathrm{shell}}(r)$,

$$E_{\mathrm{kin},\theta}(r) = \int_{V_{\mathrm{shell}}(r)} \rho \, \frac{v_\theta^2}{2} \, \mathrm{d}V, \tag{3.7}$$

with v_θ being the polar velocity component. We differentiate between total lateral kinetic energies (dashed lines), for which we integrate over the entire radial shell with polar angles $\theta \in [0°, 180°]$, and lateral kinetic energies near the poles (solid lines), for which the volume $V_{\mathrm{shell}}(r)$ includes only the regions of the radial shell in the vicinity of the poles for polar angles $\theta \in [0, 10°]$ and $\theta \in [170°, 180°]$. To facilitate comparison, we rescale the polar energies by the ratio of total shell volume to polar volume at each radius. Figure 3.2 shows the lateral kinetic energies averaged over the time interval $t \in [300\,\mathrm{ms}, 350\,\mathrm{ms}]$, which corresponds to the phase of violent turbulent motions in the gain layer shortly before exploding models exhibit shock runaway. In the region behind the shock, i.e. between 120 km and 220 km, the polar kinetic energies are significantly suppressed in the simulation with coarser polar grid resolution ('pol/80', solid blue line), when compared to the other two simulations (solid orange and green lines), but also when compared to the total kinetic energy (dashed blue line). For simulations with high polar resolution ('equ/80' and 'uni/80'), the polar energies exceed the total energies (dashed orange and green lines) for radii between 170 km and 220 km.

Since all our successful explosions of the s20 progenitor model in 2D are driven by strong SASI sloshing motions in polar directions, we suspect that in simulations with coarser angular resolution at the poles the suppression of turbulent motions leads to conditions that are less favorable for a successful explosion because of weaker turbulent effects (see, e.g., Murphy et al. 2013; Müller and Janka 2015; Radice et al. 2016; Mabanta and Murphy 2018) in particular around the grid axis. For 2D simulations of the s20 model, this suffices to turn a successful explosion into a failed one.

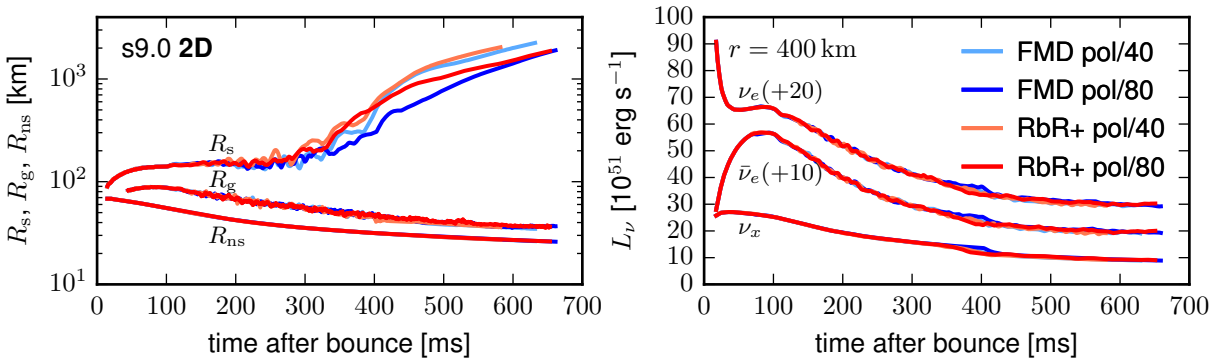

Figure 3.3.: Comparison of 2D simulations of the s9.0 progenitor model. Similarly as for Figure 3.1, we show, as functions of the time after bounce, the angle-averaged shock radii R_s, gain radii R_g, and neutron-star radii R_{ns} (all in the left panel; see labels), and the neutrino luminosities L_ν (right panel) for ν_e, $\bar{\nu}_e$, and ν_x (see labels). The neutrino luminosities are evaluated at a radius of $r = 400$ km in the co-moving frame of the stellar fluid. We differentiate the 2D simulations of the s9.0 model by color (see legend). Note that the luminosities were smoothed by running averages of 5 ms, and some lines were shifted vertically to facilitate readability of the plot. These lines are marked with labels indicating the number by which they are shifted in units of the ordinate. This figure is a slightly rearranged version of Figure 5 from Glas et al. (2019b).

3.2.3. The s9.0 Model in 2D

In order to compare simulations with the RbR+ approximation and FMD neutrino transport in the case of successful CCSN explosions, we chose the low-mass iron-core progenitor star s9.0 for our second set of 2D and 3D simulations (compare Radice et al. 2017 and Just et al. 2018, who found explosions for the s9.0 model in 2D simulations with FMD neutrino transport). For the 2D simulations of the s9.0 model, we restricted ourselves to the polar grids that we use in our 3D simulations ('pol/40' and 'pol/80').

In Figure 3.3 we present an overview of all 2D simulations of the s9.0 progenitor model. As the temporal evolution of the angle-averaged shock radii (left panel) shows, all simulations exhibit shock revival within 300 ms – 400 ms after core bounce. Apart from stochastic fluctuations, we find only minor differences in the evolution of the shock radii and perfect agreement for gain radii and neutron-star radii. Simulations with low grid resolution and with the RbR+ approximation tend to exhibit slightly larger shock radii, when compared to simulations with high resolution and with FMD transport, respectively. The time-dependent evolution of the neutrino properties agrees very well between all 2D simulations. The right panel of Figure 3.3 displays, as an example, the neutrino luminosities (evaluated at a radius of $r = 400$ km in the co-moving frame), which steadily fall due to the decline of mass accretion onto the neutron star. The slightly more pronounced drop in the luminosities between 350 ms and 420 ms corresponds to Doppler-shift effects in the co-moving frame quantities associated with the absolute increase of the radial velocity at 400 km when the shock passes this radius.

3.2.4. Summary of the 2D Simulations

We find our 2D simulations for both progenitor models, s20 and s9.0, to be consistent with results by other groups. For a detailed assessment of 2D simulations of the s20 and s9.0 progenitor models with the Alcar code, including comparisons to results from other codes, we refer the reader to Just et al. (2018). We will come back to our 2D simulations in some parts of the next sections when

comparing results between 2D and 3D simulations.

3.3. Results from 3D Simulations: s20 Model

In this section, we present the results of our 3D simulations of the s20 progenitor model. The results for the s9.0 progenitor model can be found in Section 3.4 (for an overview of all 3D simulations that we performed, see Table 2.3).

3.3.1. General Overview: FMD versus RbR+

We carried out four 3D simulations of the s20 progenitor model and followed the post-bounce phase for at least 500 ms. For a general overview of our simulations, we present the temporal evolution of several diagnostic quantities in Figure 3.4. The top panel shows the angle-averaged shock radii $R_{\rm s}$ (solid lines), the average gain radii $R_{\rm g}$ (dashed lines), and the neutron-star radii $R_{\rm ns}$ (dotted lines), which are defined as the radii at which the angle-averaged density drops below $10^{11}\,{\rm g\,cm^{-3}}$. Both neutron-star radii and gain radii show an essentially identical behavior in all four simulations (see legend in the top right), indicating that the influence of the neutrino-transport method and the grid resolution on the neutron-star contraction are negligible.

The evolution of the shock radii reveals various features that are present in all four simulations: In the first 100 ms after bounce, the stalled shock (having experienced energy drain by nuclear photodisintegration and neutrino losses) expands to roughly 150 km, pushed outward by the accreted mass that assembles itself around the nascent neutron star. Subsequently, the shock begins to retreat as the neutron star contracts in response to neutrino losses. Shortly after 200 ms, the Si/Si-O interface falls through the shock, accompanied by a steep decrease in the mass accretion rate (compare Figure 2.3), which causes an almost immediate increase of the shock radius. The subsequent evolution depends strongly on the influence of hydrodynamic instabilities, in particular SASI mass motions, which lead to alternating phases of shock expansion and shock retraction until the end of our simulations. For the low-resolution simulations we find slightly stronger oscillations and larger values of the shock radius in the case of the RbR+ approximation. For the high-resolution simulations, however, the differences in the evolution of the shock radii between RbR+ and FMD are only minor and, when disregarding fluctuations that arise due to the stochastic nature of hydrodynamic instabilities, the RbR+ and FMD simulations are in very good agreement with each other. Without any indications of shock runaway, the average shock radii decrease to 80 km or less at the end of all 3D simulations. In contrast to some of the 2D cases (compare Figure 3.1), we do not find any successful explosion in 3D simulations of the s20 model.

As already discussed in Section 3.2, successful shock revival depends on the conditions in the gain layer. Favorable conditions for an explosion arise when the advection timescale $\tau_{\rm adv}$ exceeds the heating timescale $\tau_{\rm heat}$, resulting in a ratio $\tau_{\rm adv}/\tau_{\rm heat} \gtrsim 1$. The center left panel of Figure 3.4 shows the ratio of advection to heating timescale for all 3D simulations of the s20 progenitor model. Corresponding to phases of shock expansion and shock retraction, all simulations exhibit phases with conditions that are more and less favorable for shock revival, i.e. where $\tau_{\rm adv}/\tau_{\rm heat}$ is close to unity, or much smaller than unity, respectively. In low-resolution simulations, the RbR+ approximation leads to conditions that are more beneficial for shock revival than results with FMD transport at most times. This is consistent with the larger shock radii that we observe in the RbR+ simulation. In contrast, the high-resolution simulations exhibit quite similar conditions for shock revival throughout the whole simulated evolution with considerably smaller differences between RbR+ and FMD than in the low-resolution cases.

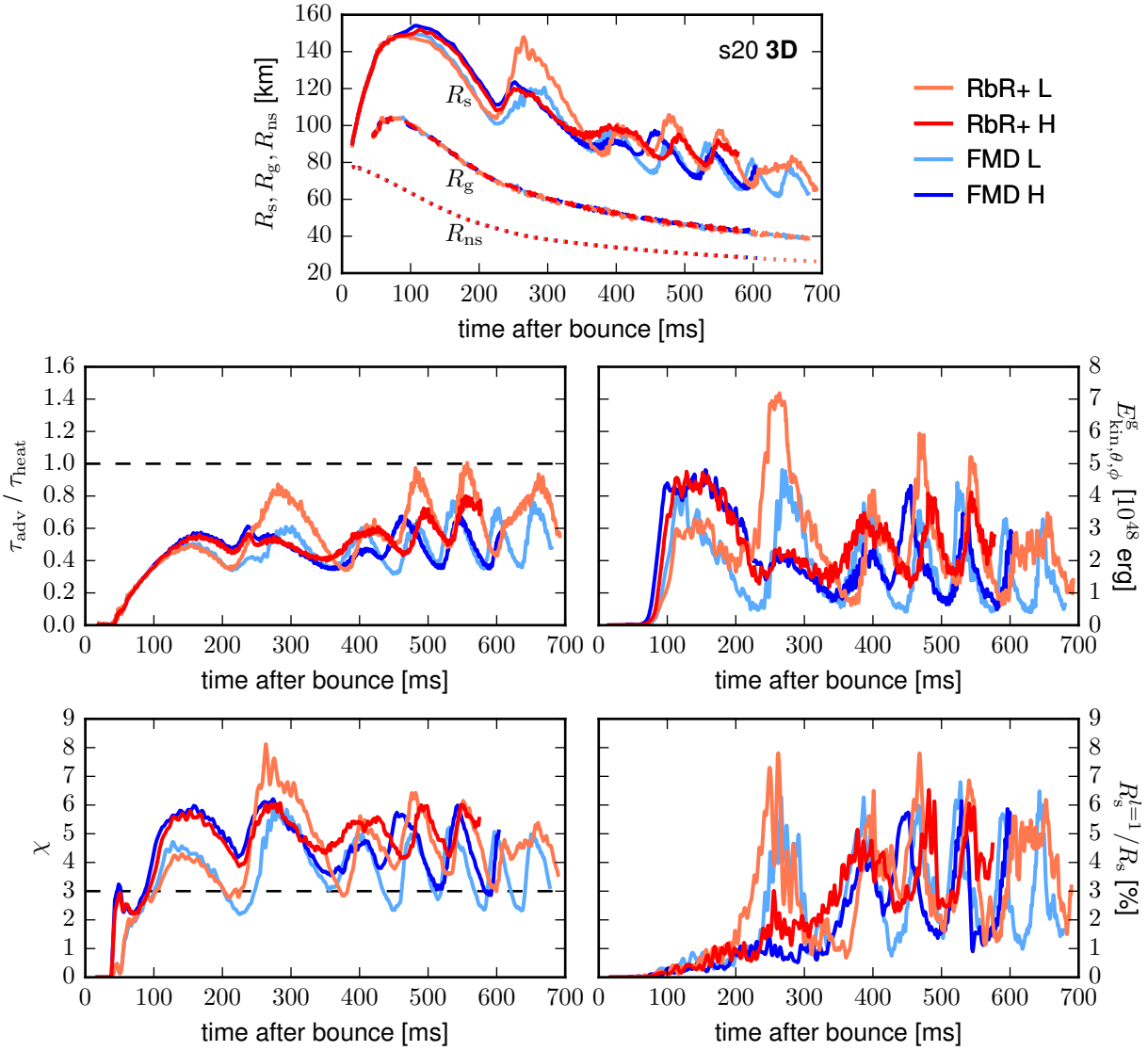

Figure 3.4.: Overview of all 3D simulations of the s20 progenitor model. Shown are, as functions of the time after bounce, the angle-averaged shock radii R_s (solid lines), average gain radii R_g (dashed lines), and neutron-star radii R_{ns} (dotted lines; all in the top panel), the ratios of advection to heating timescales τ_{adv}/τ_{heat} (center left panel), the non-radial kinetic energies in the gain layer $E^g_{kin,\theta,\phi}$ (center right panel), the χ parameters (bottom left panel), and the dipole moments of the angle-dependent shock radii $R_s^{l=1}$, normalized to corresponding values of the monopole moments R_s (bottom right panel). The different line colors correspond to low- (suffixes "L") and high-resolution (suffixes "H") simulations with either the FMD neutrino-transport scheme or the RbR+ approximation (see legend). Note that χ and $R_s^{l=1}$ were smoothed by running averages of 5 ms. This figure is a slightly rearranged version of Figure 6 from Glas et al. (2019b).

3.3.2. Influence of the Grid Resolution in 3D

In addition to the aforementioned differences between simulations with RbR+ and FMD, we find the high-resolution simulations to exhibit larger shock radii (roughly 10 km difference) between 100 ms and 220 ms after bounce, when compared to the low-resolution cases. Consequently, the masses in the gain layer and, therefore, the advection timescales are larger in high-resolution simulations, leading to higher timescale ratios in these cases. These differences between low- and high-resolution simulations are caused by hydrodynamic instabilities in the post-shock region, which are slightly stronger and, thus, push the shock further outward in the high-resolution simulations. This can be seen from the center right panel of Figure 3.4, which shows the non-radial kinetic energies in the gain layer, $E^{\mathrm{g}}_{\mathrm{kin},\theta,\phi}$, as functions of the time after bounce. We calculate $E^{\mathrm{g}}_{\mathrm{kin},\theta,\phi}$ by the volume integral[1]

$$E^{\mathrm{g}}_{\mathrm{kin},\theta,\phi} = \int_{V_{\mathrm{gain}}} \rho \left(\frac{v_\theta^2 + v_\phi^2}{2} \right) \mathrm{d}V, \tag{3.8}$$

with polar and azimuthal velocity components v_θ and v_ϕ, respectively. The high-resolution simulations exhibit a slightly earlier rise and larger values of the lateral kinetic energies until 200 ms p.b., after which they start oscillating in all simulations in a similar manner as the angle-averaged shock radii.

A possible explanation for the different behavior between low- and high-resolution simulations in these first 200 ms is provided by Fernández and Thompson (2009), who show that higher (radial) grid resolution is beneficial for the growth of SASI, and results from 3D CCSN simulations by Fernández (2015) reveal higher kinetic energies in the gain layer for simulations with higher angular resolution (see Figure 7d there). In order to assess the evolution of hydrodynamic instabilities in the post-shock layer in more detail and, in particular, to distinguish between SASI-dominated and convection-dominated phases in our simulations, we analyze two additional diagnostic quantities.

First, we consider the χ parameter (Foglizzo et al., 2006), which provides information about the conditions for the growth of convection in the post-shock layer. Favorable conditions arise when buoyant mass motions can set in faster than seed perturbation get advected out of the gain layer, i.e., when the timescale for the growth of convective activity is short compared to the advection timescale. The χ parameter essentially measures the ratio of advection timescale to convective growth timescale in the gain layer,

$$\chi = \int \frac{\langle \omega_{\mathrm{BV}} \rangle}{|\langle v_r \rangle|} \, \mathrm{d}r, \tag{3.9}$$

with the Brunt-Väisälä frequency ω_{BV} and the angle-averaged radial velocity $\langle v_r \rangle$. We apply linear averaging of ω_{BV} as described in Appendix B[2], and we only take into account regions in the gain layer with $R_{\mathrm{g}} < r < R_{\mathrm{s}}(\theta, \phi)$ that are locally unstable for convection, i.e. where $\omega_{\mathrm{BV}} > 0$. According to Foglizzo et al. (2006, assuming the linear regime for the growth of perturbations), a value of $\chi \gtrsim 3$ is necessary for the development of convective activity in the gain layer.

Short advection timescales (corresponding to small values of χ) disfavor the growth of convection in the post-shock layer, but they have been shown to amplify the linear growth rates of SASI (see, e.g., Foglizzo et al., 2006; Scheck et al., 2008; Müller et al., 2012a). Thus, we can at least very roughly discriminate between conditions that are beneficial for convective growth ($\chi \gtrsim 3$), and

[1] Note that Equations (3.7) and (3.8) define two different types of lateral kinetic energies. Equation (3.7) defines $E_{\mathrm{kin},\theta}(r)$ for radial shells (see Section 3.2), whereas Equation (3.8) defines $E^{\mathrm{g}}_{\mathrm{kin},\theta,\phi}$ for the whole gain layer.

[2] For a detailed discussion of the various methods to calculate the χ parameter and the definition of the Brunt-Väisälä frequency, see Appendix B.

conditions that favor the development of SASI activity ($\chi \lesssim 4$)[3].

Second, we perform a multipole analysis and decompose the angle-dependent shock radii $R_\mathrm{s}(\theta,\phi)$ into real spherical harmonics $Y_l^m(\theta,\phi)$ of degree l and order m (see, e.g., Burrows et al., 2012; Ott et al., 2013),

$$Y_l^m(\theta,\phi) = \begin{cases} \sqrt{2}\, N_l^m P_l^m(\cos\theta)\cos m\phi & m>0, \\ N_l^0 P_l^0(\cos\theta) & m=0, \\ \sqrt{2}\, N_l^{|m|} P_l^{|m|}(\cos\theta)\cos|m|\phi & m<0, \end{cases} \tag{3.10}$$

with the associated Legendre polynomials P_l^m and

$$N_l^m = \sqrt{\frac{2l+1}{4\pi}\frac{(l-m)!}{(l+m)!}}. \tag{3.11}$$

The multipole coefficients read (Hanke et al., 2013)

$$a_l^m = \frac{(-1)^{|m|}}{\sqrt{4\pi(2l+1)}} \int R_\mathrm{s}(\theta,\phi) Y_l^m(\theta,\phi)\,\mathrm{d}\Omega. \tag{3.12}$$

With this normalization, the monopole moment ($l=0$) is trivially given by the angle-averaged shock radius, $R_\mathrm{s}^{l=0} = a_0^0 = R_\mathrm{s}$, and the dipole moment ($l=1$) is obtained by

$$R_\mathrm{s}^{l=1} = \sqrt{\sum_{m=-1}^{1} [a_1^m(r)]^2}. \tag{3.13}$$

For later reference, we identify the components of the dipole vector in Cartesian coordinates to coincide with $a_x = a_1^1$, $a_y = a_1^{-1}$, and $a_z = a_1^0$. The large-scale motions of SASI sloshing and spiral modes are reflected in large amplitudes of dipolar or quadrupolar character, whereas convective overturn can both result in smaller-scale deformation of the shock (i.e. excitation of higher l-modes, $l>2$, of shock asymmetry) and in large-scale deformation when large high-entropy plumes ascend toward the shock surface.

Figure 3.4 shows the temporal evolution of the χ parameters in the bottom left panel and the dipole moments of the shock deformation, normalized by the angle-averaged shock radii, in the bottom right panel. Starting at 100 ms after bounce, we find high-resolution simulations because of larger shock radii to exhibit more favorable conditions for convective growth, i.e. systematically larger values of χ than in the low-resolution cases until 250 ms after bounce. The increasing dipole moments of the shock deformation reveal that convective overturn in high-resolution simulations becomes more violent with time, with the dipole moments reaching up to 3% of the monopoles' amplitudes at ~ 250 ms. In contrast, the low-resolution simulations exhibit only weak convective activity with $\chi \lesssim 4$ and stay SASI-dominated until at least 250 ms after bounce. They develop their first violent SASI activity with a combination of sloshing and spiral modes between 200 ms and 300 ms, which cause the angle-averaged shock radii to exhibit large oscillations and the dipole amplitudes of the shock deformation to reach up to 8% of the average shock radii. Due to the infall of the Si/Si-O interface shortly after 200 ms p.b., the shock rapidly expands in both low- and

[3]Note that in addition to analyzing the χ parameter, we inspected the time-dependent evolution of the entropy distribution to discriminate between phases of convection and SASI. The sloshing and spiral modes of SASI can be identified by large-scale motions of the entropy-jump at the shock, whereas the appearance of low- and high-entropy plumes indicates convective overturn. We found that the χ parameter matches the phases of SASI growth ($\chi \lesssim 4$) and of growth of convection ($\chi \gtrsim 3$) quite well for all our 3D simulations.

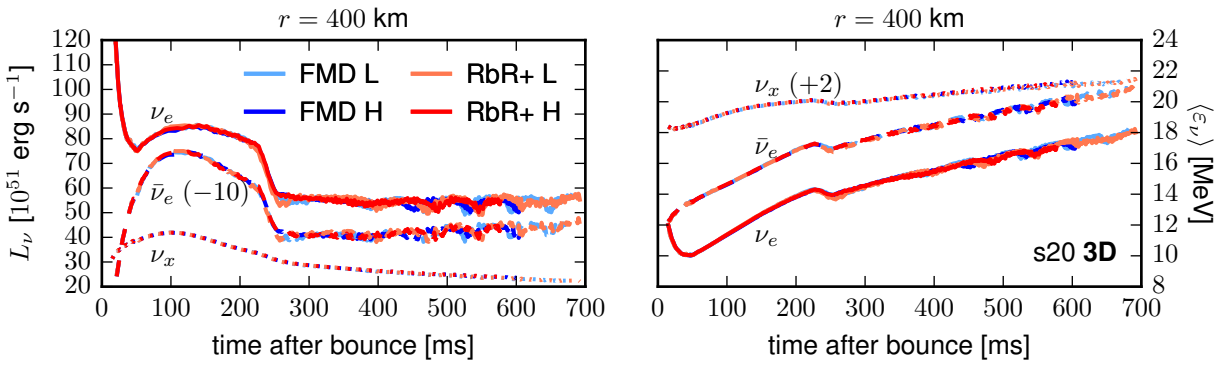

Figure 3.5.: Neutrino luminosities L_ν (left panel) and neutrino mean energies $\langle\varepsilon_\nu\rangle$ (right panel) as functions of time after bounce for all 3D simulations of the s20 progenitor model. Luminosities and mean energies are measured at a radius of $r = 400\,\mathrm{km}$ in the co-moving frame of the stellar fluid for electron neutrinos ν_e (solid lines), electron antineutrinos $\bar{\nu}_e$ (dashed lines), and heavy lepton neutrinos ν_x (dotted lines). Note that some lines were shifted vertically to facilitate readability of the plot. These lines are labeled with the number by which they are shifted in units of the ordinate in parentheses. This figure is a slightly rearranged version of Figure 7 from Glas et al. (2019b).

high-resolution simulations, leading to an increase of the mass in the gain layer and, consequently, of the advection timescale. As a result, all simulations experience a convection-dominated phase at around 300 ms after bounce.

The subsequent evolution after 300 ms p.b. is similar in all simulations with alternating phases of convection and SASI, which represent repetitions of the following cycle: During a shock-retraction phase, small shock radii and short advection timescales amplify the growth rates of SASI. Combinations of SASI sloshing and spiral modes evolve and expand the shock front, leading to larger advection timescales, which favor the growth of convective motions and damp the further growth of SASI. With the shock reaching a maximal radius, the cycle enters a convection-dominated phase, before the shock recedes again and SASI growth sets in once again.

3.3.3. Surface-Integrated Neutrino Luminosities and Energies

The evolution of hydrodynamic instabilities in the post-shock region with alternating phases of SASI and convection and shock expansion and contraction influences the mass accretion rate onto the neutron star. As a consequence, temporal fluctuations in the angle-averaged densities and temperatures occur at the surface of the neutron star. Since electron-type neutrinos (ν_e and $\bar{\nu}_e$) energetically decouple from the stellar matter in this region, their luminosities and energies reflect the time-dependent fluctuations of the thermodynamic conditions at the neutron-star surface. The left panel of Figure 3.5 shows corresponding fluctuations of the order of 10% to 20% in both the ν_e and $\bar{\nu}_e$ luminosities starting at roughly 400 ms after bounce. On a much smaller scale, these variations also exist in the mean energies of ν_e and $\bar{\nu}_e$ (see right panel of Figure 3.5). The mean energies of the radial neutrino fluxes are defined for any species ν at a radius r by

$$\langle\varepsilon_\nu(r)\rangle = \frac{\int F_\nu^r(r)\ \mathrm{d}\varepsilon\ \mathrm{d}\Omega}{\int F_\nu^r(r)\ \varepsilon^{-1}\ \mathrm{d}\varepsilon\ \mathrm{d}\Omega}. \tag{3.14}$$

The luminosities and mean energies of heavy-lepton neutrinos (ν_x) are hardly affected by fluctuations in the density and temperature at the neutron-star surface, because they are produced only much

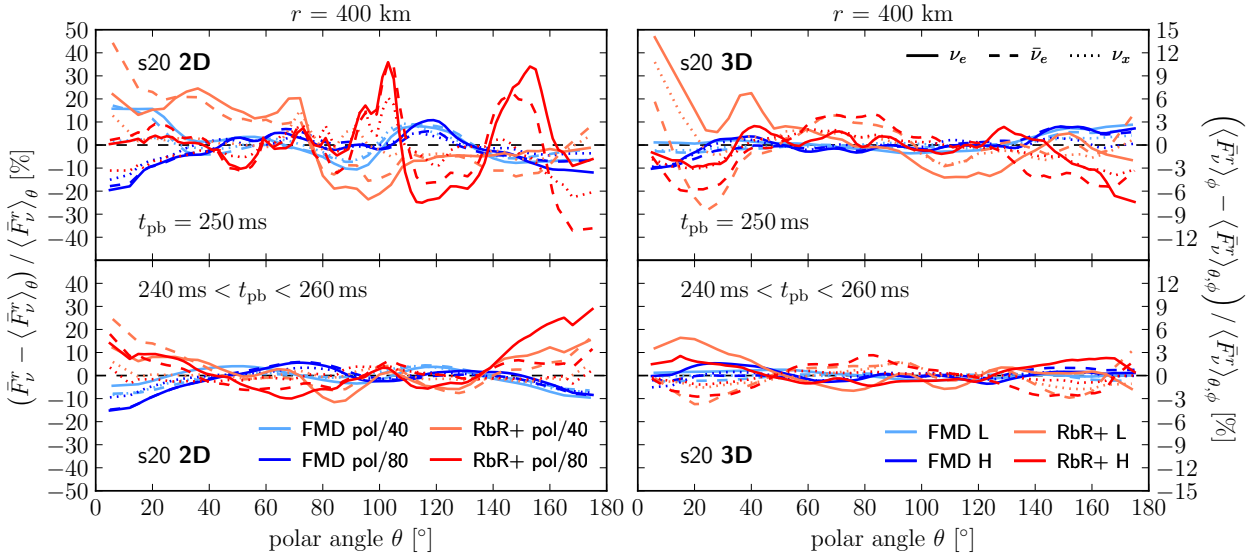

Figure 3.6.: Lateral variations of energy-integrated radial neutrino fluxes $\bar{F}^r_\nu$, relative to their angular averages $\langle\bar{F}^r_\nu\rangle$ (see Equations (3.15a) to (3.15c)) and normalized by the angle-averaged fluxes, as functions of the polar angle θ for various simulations of the s20 progenitor model (see legends in the bottom panels, indicative for each column) for ν_e (solid lines), $\bar{\nu}_e$ (dashed lines), and ν_x (dotted lines). We compare 2D simulations (left panels) and 3D simulations (right panels). For the latter the fluxes are averaged over the azimuthal angle ϕ (i.e., $\langle\bar{F}^r_\nu\rangle_\phi$ and $\langle\bar{F}^r_\nu\rangle_{\theta,\phi}$, respectively). The top panels show flux deviations for temporal snapshots of each simulation at a post-bounce time of $t_{\rm pb} = 250\,{\rm ms}$, whereas the bottom panels show time-averaged deviations in the time interval $240\,{\rm ms} < t_{\rm pb} < 260\,{\rm ms}$. All fluxes are measured at a radius of $r = 400\,{\rm km}$ in the co-moving frame of the stellar fluid. Note that the range of the ordinate changes from left to right panels. This figure is taken from Glas et al. (2019b, Figure 8).

deeper inside the neutron star by thermal pair creation and bremsstrahlung processes, and scattering of ν_x on electrons and nucleons does not suffice for ν_x to stay in thermodynamic equilibrium with the stellar fluid in the accretion layer.

Because the evolution of hydrodynamic instabilities is very similar in all simulations with only phase shifts in the cyclic shock expansion and contraction phases due to the stochastic nature of SASI and convection, there are also no significant differences between the neutrino luminosities and mean energies of all our 3D simulations of the s20 progenitor. In particular, although the dynamical evolution exhibits some differences between low-resolution and high-resolution simulations in the first 300 ms after bounce, the neutrino properties still agree to an excellent degree. We conclude that surface-integrated luminosities and mean energies of neutrinos are very robust and do not sensitively depend on the neutrino-transport method or the numerical grid resolution.

3.3.4. Angular Variations of the Neutrino Fluxes

In addition to the analysis of surface-integrated luminosities, we also consider the angular variations of the neutrino fluxes. Figure 3.6 shows the deviations of energy-integrated radial neutrino fluxes $\bar{F}^r_\nu$ to their angular averages $\langle\bar{F}^r_\nu\rangle$ as functions of the polar angle θ. In general, the angular averages

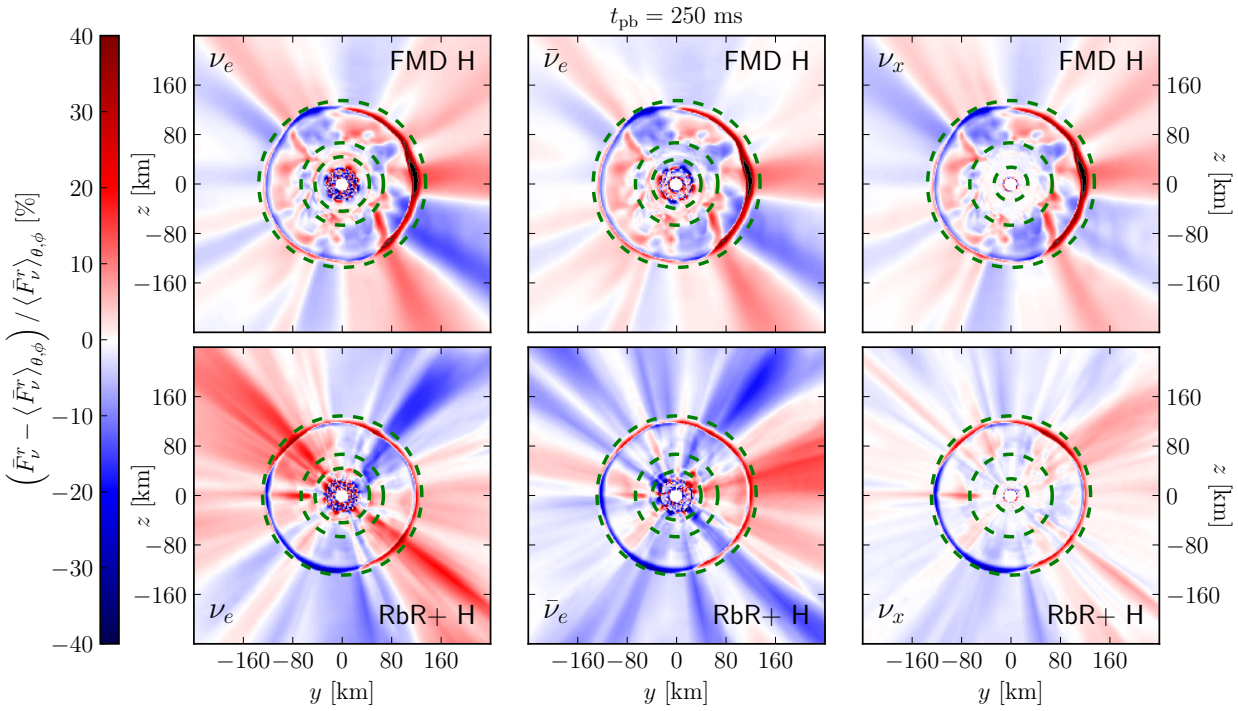

Figure 3.7.: Relative variations between energy-integrated radial neutrino fluxes $\bar{F}^r_\nu$ and their angular averages $\langle \bar{F}^r_\nu \rangle_{\theta,\phi}$ (see Equation (3.15c)), normalized by the angle-averaged fluxes, for the 3D high-resolution simulations of the s20 progenitor model. We show the results in a plane (y-z) that contains the polar axis of our spherical polar grid. Results with FMD neutrino-transport scheme (top panels) are compared to the RbR+ approximation (bottom panels) for ν_e (left panels), $\bar{\nu}_e$ (central panels), and ν_x (left panels). All fluxes are measured in the co-moving frame of the stellar fluid. Similar to Figure 3.6, we show flux variations for temporal snapshots at a post-bounce time of $t_{\rm pb} = 250\,$ms. The inner (central, outer) green, dashed circles indicate the average neutrino spheres (average gain radii, maximum shock radii). Note that rings composed of dark red and dark blue parts just inside the maximum shock radii result from the discontinuous behavior of the co-moving radial fluxes at the angle-dependent shock radii. To facilitate comparisons, the color bar is limited to a range of $[-40\%, 40\%]$ and values outside of this interval are indicated by black color. This figure is taken from Glas et al. (2019b, Figure 9).

of an arbitrary quantity x are calculated by

$$\langle x \rangle_\theta = \frac{\int x \sin\theta \, \mathrm{d}\theta}{\int \sin\theta \, \mathrm{d}\theta}, \tag{3.15a}$$

$$\langle x \rangle_\phi = \frac{\int x \, \mathrm{d}\phi}{\int \mathrm{d}\phi}, \tag{3.15b}$$

$$\langle x \rangle_{\theta,\phi} = \frac{\int x \sin\theta \, \mathrm{d}\theta \, \mathrm{d}\phi}{\int \sin\theta \, \mathrm{d}\theta \, \mathrm{d}\phi}. \tag{3.15c}$$

The energy-integrated radial fluxes for any neutrino species ν are obtained by (compare Equation (A.3b))

$$\bar{F}^r_\nu = \int F^r_\nu \, \mathrm{d}\varepsilon. \tag{3.16}$$

Because most variations of radial fluxes occur in phases of strong hydrodynamic instabilities, we analyze the fluxes for a temporal snapshot at a post-bounce time of $t_{\rm pb} = 250\,$ms (top panels), when

the low-resolution simulations experience strong shock expansion due to violent SASI activity, and the high-resolution simulations exhibit strong convective overturn[4]. The deviations of the radial fluxes from their angular averages are significantly larger in both 2D (left side) and 3D (right side) simulations with the RbR+ approximation, when compared to the FMD neutrino-transport scheme. This observation also holds for flux variations that have been averaged over a time interval of $240\,\mathrm{ms} < t_{\mathrm{pb}} < 260\,\mathrm{ms}$ (see bottom panels). However, the amplitude of variations is significantly smaller in 3D simulations than in 2D models, e.g., it is less than 15% for RbR+ and 3% for FMD results for the temporal snapshot in 3D compared to up to 45% for RbR+ and 20% for FMD for the 2D case (notice that the range of the ordinate changes from left to right panels). The time-averaged deviations decrease to 5% or less in all 3D simulations, although in particular the low-resolution RbR+ simulation exhibits strong SASI sloshing and spiral motions during this phase. The time-averaged deviations reach up to 30% in 2D simulations with the RbR+ approximation, with the largest excursions for all neutrino species appearing at the poles (where $\theta \approx 0°$ and $\theta \approx 180°$, respectively). This observation strengthens our argument from Section 3.2, where we suspected that in 2D simulations the RbR+ approximation together with axial sloshing motions of SASI can amplify local variations at the poles which are already visible in the simulations with FMD transport. In contrast, we do not find this behavior in 3D simulations with RbR+ where time-averaged results of RbR+ and FMD models are much more similar (see bottom right panel of Figure 3.6). We further remark that we do not observe any significant dependence of angular variations of radial fluxes on the grid resolution, neither in 2D, nor in 3D simulations.

In simulations with the RbR+ approximation, the non-radial flux components F_ν^θ and F_ν^ϕ are not evolved. One consequence of this treatment can be seen in Figure 3.7, which displays the deviations of $\bar{F}_\nu^r$ from the angular averages $\langle \bar{F}_\nu^r \rangle_{\theta,\phi}$ for ν_e (left), $\bar{\nu}_e$ (center), and ν_x (right) with color coding in a plane (y-z) that contains the polar axis of the spherical polar grid. The high-resolution RbR+ simulation (bottom panels) shows radial "streaks" for all neutrino species between the shock and the neutrino energy sphere, at which neutrinos decouple energetically from the stellar matter, i.e. where the energy-averaged effective optical depth fulfills $\tau(r) = 2/3$. The optical depth is defined as

$$\tau(r) = \int_r^\infty \kappa_{\mathrm{eff}}(r')\,\mathrm{d}r', \tag{3.17}$$

with κ_{eff} the effective opacity,

$$\kappa_{\mathrm{eff}} = \sqrt{\kappa_{\mathrm{abs}}\kappa_{\mathrm{tot}}}, \tag{3.18}$$

calculated from the absorption and total opacities, κ_{abs} and κ_{tot}, and energetically averaged as in Buras et al. (2006b). For ν_e, e.g., the region between neutrino sphere (inner green, dashed circle) and maximum shock radius (outer green, dashed circle) approximately extends from 44 km to 129 km. In contrast, local variations in the radial neutrino fluxes are smoothed out by lateral flux components in the simulation with FMD neutrino-transport scheme (top panels), leading to a "patch-like" structure in the region between the neutrino sphere and the maximum shock radius (e.g., between 44 km and 135 km for ν_e). The FMD simulation exhibits a "streak-like" pattern, as it is seen in the RbR+ case, only outside this region, where non-radial neutrino flux components are approaching zero and, therefore, both neutrino-transport methods behave identically. Apart from these observations, we find maximal flux deviations for ν_e and $\bar{\nu}_e$ to be of the same order between RbR+ and FMD simulations, and for ν_x to be even smaller for the RbR+ simulation when compared to the FMD case.

[4]Since we compare to 2D simulations, we remark here that also the 2D simulations exhibit shock expansion caused by SASI sloshing motions in this phase (see Section 3.2).

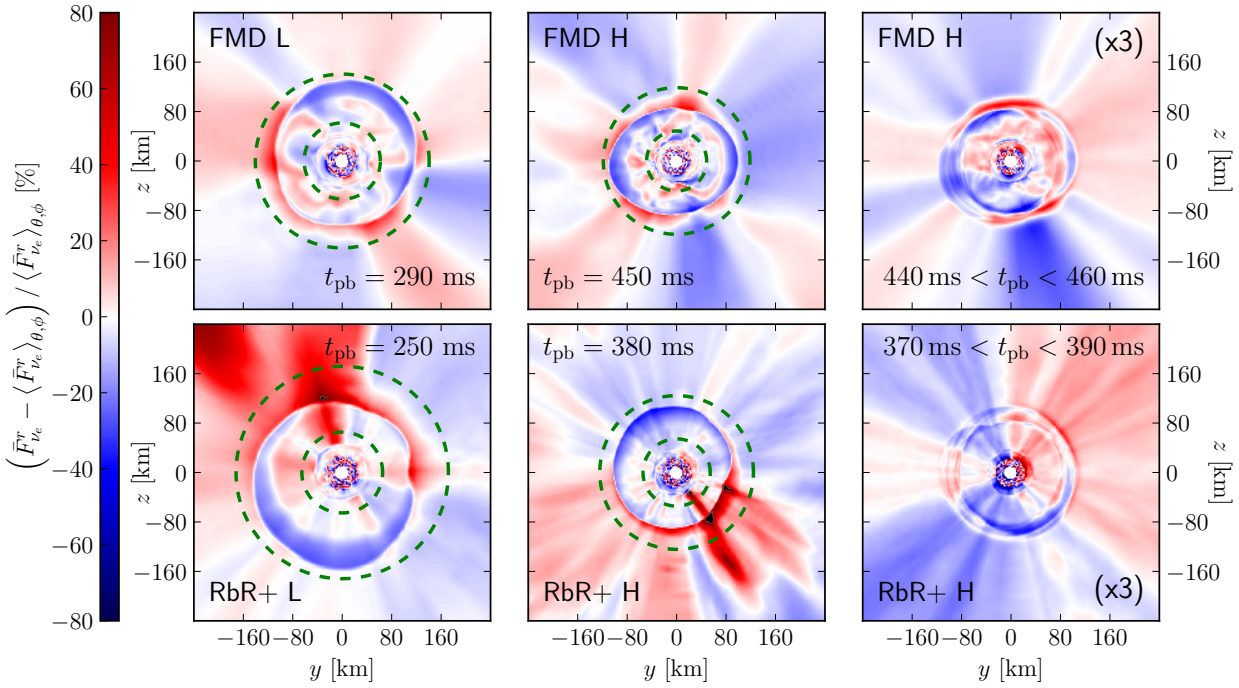

Figure 3.8.: Relative neutrino-flux variations as in Figure 3.7, but only for electron neutrinos, and for both low-resolution (left panels) and high-resolution (center and right panels) simulations of the s20 progenitor model at temporal snapshots that differ from Figure 3.7. The corresponding post-bounce times $t_{\rm pb}$ are noted in each panel. The flux variations in the right panel are averaged over time intervals of 20 ms. The inner (outer) green, dashed circles indicate the average gain (maximum shock) radii, respectively. To facilitate comparisons, the color bar is limited to a range of $[-80\%, 80\%]$ and values outside of this interval are indicated by black color. The time-averaged values in the right panels were scaled by a factor of 3. This figure is taken from Glas et al. (2019b, Figure 10).

Previous findings from 2D simulations suggest that the RbR+ approximation can amplify local deviations in particular in combination with strong axial sloshing activity of the SASI (see, e.g., Skinner et al., 2016; Just et al., 2018). For this reason, we further investigate fluctuations of radial fluxes in our 3D simulations in phases of violent SASI mass motions. Figure 3.8 again shows variations of $\bar{F}^r_{\nu_e}$ relative to the angular averages, but for low- (left panels) and high-resolution (central panels) simulations in phases of strong SASI-activity (the corresponding post-bounce times $t_{\rm pb}$ are noted in each panel). We restrict ourselves to analyze only fluxes of ν_e, since Figure 3.7 revealed no fundamental differences in the behavior of ν_e and $\bar{\nu}_e$ and relatively less prominent differences between RbR+ and FMD results for ν_x. In both simulations with the RbR+ approximation we find local "hot spots" at which the radial neutrino fluxes are high and, thus, significantly deviate from the angular averages. These deviations reach up to 80% and more, e.g. in the top left sector for the low-resolution RbR+ simulation (bottom left panel), and in the bottom right sector for the high-resolution RbR+ simulation (bottom center panel). In contrast, the FMD simulations (upper left and center panels) exhibit much lower variations. The time-averaged deviations of $\bar{F}^r_{\nu_e}$ are much smaller than corresponding instantaneous values for both high-resolution simulations, e.g., when averaged over a 20 ms time interval (right panels; the values in the right panels are scaled up by a factor of 3), and are more similar between high-resolution RbR+ and FMD simulations.

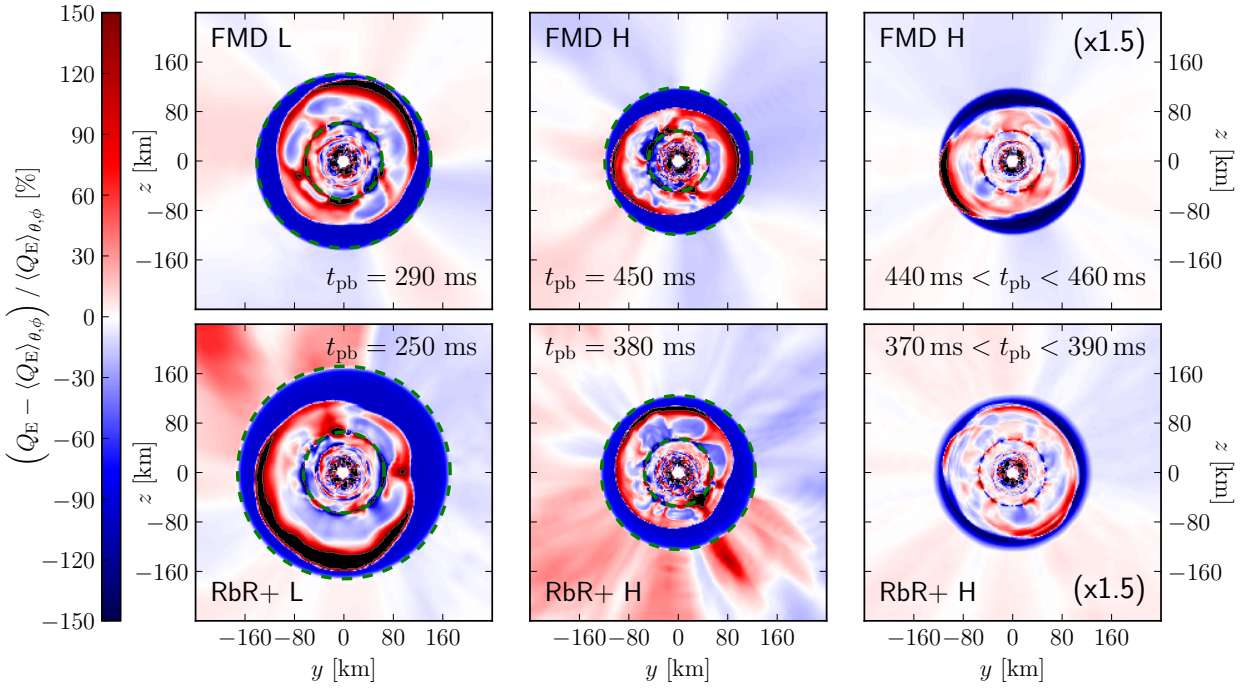

Figure 3.9.: Relative variations between the local net neutrino heating rates Q_E and their angular averages $\langle Q_E \rangle_{\theta,\phi}$ (see Equation (3.15c)), normalized by the angle-averaged values, for our 3D simulations of the s20 progenitor model. Correspondingly to Figure 3.8, the panels show data for temporal snapshots (left and center) and time-averaged values (right) in the same y-z-plane and for the same selection of simulations. The inner (outer) green, dashed circles indicate the average gain (maximum shock) radii, respectively. To facilitate comparisons, the color bar is limited to a range of $[-150\%, 150\%]$ and values outside of this interval are indicated by black color. The time-averaged values in the right panels were scaled by a factor of 1.5. Dark blue regions in the vicinity of the maximum shock radii are outside the gain layer and, thus, do not experience strong neutrino heating, whereas dark red and black regions are still inside the gain layer. Variations outside the maximum shock radii are irrelevant since the (absolute) heating rates are very small in these regions. This figure is taken from Glas et al. (2019b, Figure 11).

3.3.5. Neutrino-Heating Rates

In order to estimate the influence of locally amplified neutrino fluxes as seen in the RbR+ simulations on the neutrino heating in the gain layer, we consider deviations of the local net neutrino heating rates, which are given by the energy source term Q_E (see Equation (2.21c)), from their angular averages $\langle Q_E \rangle_{\theta,\phi}$ (see Equation (3.15c)). Figure 3.9 presents such deviations for low- and high-resolution 3D simulations for the same temporal snapshots as in Figure 3.8, i.e., during phases of violent SASI activity in all simulations. The amplitudes of fluctuations of the local heating rates are of the same order in all 3D simulations. Dark blue regions in the vicinity to the maximum shock radii are outside the gain layer and, therefore, do not experience strong neutrino heating, whereas dark red and black regions are still inside the gain layer. The spatial scales of regions with locally enhanced or reduced neutrino heating are large in low-resolution simulations, whereas high-resolution simulations resolve finer structures in the gain layer. However, the results do not show any significant differences in the spatial scales between simulations with RbR+ and FMD. Furthermore, the time-averaged heating rates, which are scaled up by a factor of 1.5, reveal very

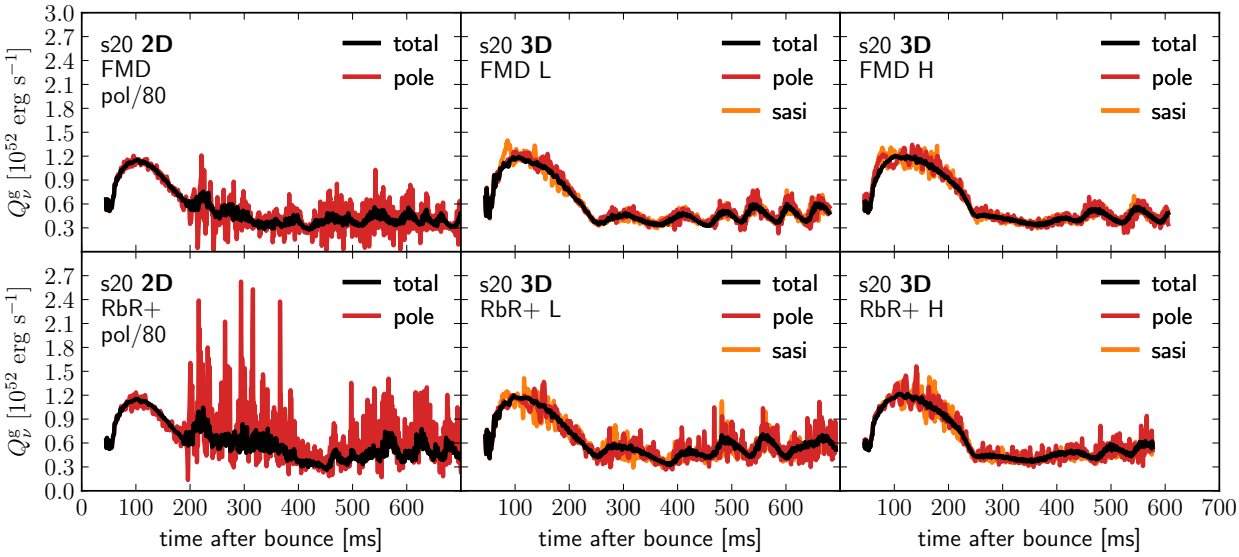

Figure 3.10.: Net neutrino heating rates, integrated over the gain layer, Q_ν^g (see Equation (3.4)), as functions of the time after bounce, for 2D and 3D simulations of the s20 progenitor model. 2D simulations are shown in the left panels, 3D simulations with low-resolution in the central panels, and high-resolution results in the right panels. The top (bottom) panels display simulations with the FMD neutrino-transport scheme (with the RbR+ approximation), respectively. Total heating rates (labeled "total"; black lines) are compared to the heating rates in a 19° cone around the north pole (i.e., where $\theta = 0°$; labeled "pole"; red lines), and to the heating rates in a 19° cone around the instantaneous SASI dipole direction (labeled "sasi"; orange lines), respectively. To facilitate comparisons, the heating rates at the poles and in the SASI directions are rescaled by the ratios of the total volume of the gain layer to the volumes of the constrained cones of integration. This figure is taken from Glas et al. (2019b, Figure 12).

similar patterns in RbR+ and FMD simulations. Regions with enhanced time-averaged heating rates (dark red and black regions) at a radius of roughly 100 km to 120 km indicate maximal excursions of the shock radii due to SASI motions.

In addition to instantaneous and time-averaged neutrino heating rates, we further investigate the time-dependent evolution of the total (net) neutrino heating rates in the gain layer, Q_ν^g. In Figure 3.10 Q_ν^g is compared for 2D simulations (left panels) and 3D simulations with low (central panels) and high resolution (right panels), respectively. The total heating rates (black lines), which result from integrating the local energy source terms Q_E over the entire volume of the gain layer (see Equation (3.4)), agree to high degree between all 2D and 3D simulations. In contrast, a different behavior is observed for the polar heating rates (red lines), for which the integral was carried out only over regions of the gain layer in the vicinity of the north pole, i.e., where the polar angle $\theta \in [0, 19°]$. To facilitate comparison, the heating rates at the pole are rescaled by the ratio of total volume to polar volume. In the 2D simulation with the RbR+ approximation (lower left panel) the polar heating rates are significantly larger than in the corresponding 2D simulation with FMD neutrino transport (upper left panel). Furthermore, the polar heating rates are enhanced in comparison to the total rates in the 2D RbR+ simulation, whereas they fluctuate around the total rates in the 2D FMD simulation with considerably lower amplitudes. These findings support our argument, that in 2D simulations the RbR+ approximation overestimates polar variations in feedback with strong axial SASI sloshing motions and, thus, it leads to conditions that are more favorable for successful shock revival than those obtained in 2D simulations with an FMD neutrino-transport scheme.

However, in 3D simulations with FMD and RbR+ the polar heating rates show much less differences. The low-resolution simulation with RbR+ exhibits slightly larger polar heating rates (central panels), whereas the differences between FMD and RbR+ almost vanish for high-resolution simulations (right panels). In general, we find the polar heating rates in 3D simulations to fluctuate much less around the total rates. Since, in contrast to 2D simulations, SASI sloshing and spiral modes are not restricted to a prescribed direction in 3D simulations, we also analyze the heating rates in the gain layer within a cone of half-opening angle of 19° around the instantaneous direction of the SASI mass motions, i.e., the dipole direction of the shock deformation, see Equations (3.12) and (3.13), and the associated explanations. The neutrino heating rates near the SASI direction (orange lines; we again rescale the heating rates by the ratio of total volume to cone volume) exhibit a very similar behavior as the polar heating rates, with the RbR+ simulations showing only insignificantly larger heating rates in the SASI direction than the corresponding FMD simulations, in particular in the high-resolution 3D simulations.

3.3.6. Summary

We find only minor differences between 3D simulations of the s20 progenitor model with the RbR+ approximation and an FMD neutrino-transport scheme, in particular when considering local deviations of neutrino fluxes and heating rates from their angular averages in the case of time integration over periods of typically 10 ms or longer (see, e.g., Figures 3.6, 3.8 and 3.9). Moreover, surface-integrated fluxes and mean energies of neutrinos show excellent agreement (see Figure 3.5), and also the overall post-bounce evolution with alternating phases of dominant SASI or convective activity is similar in all of our 3D simulations of the s20 progenitor model (see Figure 3.4). Considering gain-layer integrated neutrino-heating rates, we find only minor differences between FMD and RbR+ (see Figure 3.10), which contrasts results from 2D simulations, in which polar heating rates are significantly amplified in the case of RbR+.

3.4. Results from 3D Simulations: s9.0 Model

3.4.1. General Overview: FMD versus RbR+

In this section we discuss the results of our 3D simulations of the s9.0 progenitor model. As in our 3D simulations of the s20 model, we used either the RbR+ approximation or the FMD scheme for neutrino transport, and performed simulations with low as well as high grid resolution. For a general overview, the temporal evolution of a selection of several diagnostic quantities is presented in Figure 3.11. We find successful shock revival at roughly 300 ms after bounce for all four simulations, which can be seen from the evolution of the angle-averaged shock radii (top panel) and the ratios of advection timescale to heating timescale (center left panel), which considerably exceed 1 at that time. The agreement in the evolution of the average positions of shock, gain radius[5], neutron-star radius, and of the timescale ratios is excellent between all four 3D simulations of the s9.0 progenitor model.

Similar to our findings for 3D simulations of the s20 model (see Figure 3.4), we observe an earlier rise and larger values of the non-radial kinetic energies in the gain layer for the high-resolution simulations (center left panel). Because of the steep density gradient at the edge of the degenerate core in the s9.0 progenitor model (see Figure 2.2) and the resulting low mass advection rate (see

[5] At late times (i.e., after about 500 ms), the exact position of the boundary between heating and cooling layers sensitively depends on highly time-variable local downflows onto the neutron star. For this reason, the gain radii start to slightly differ between simulations in that phase.

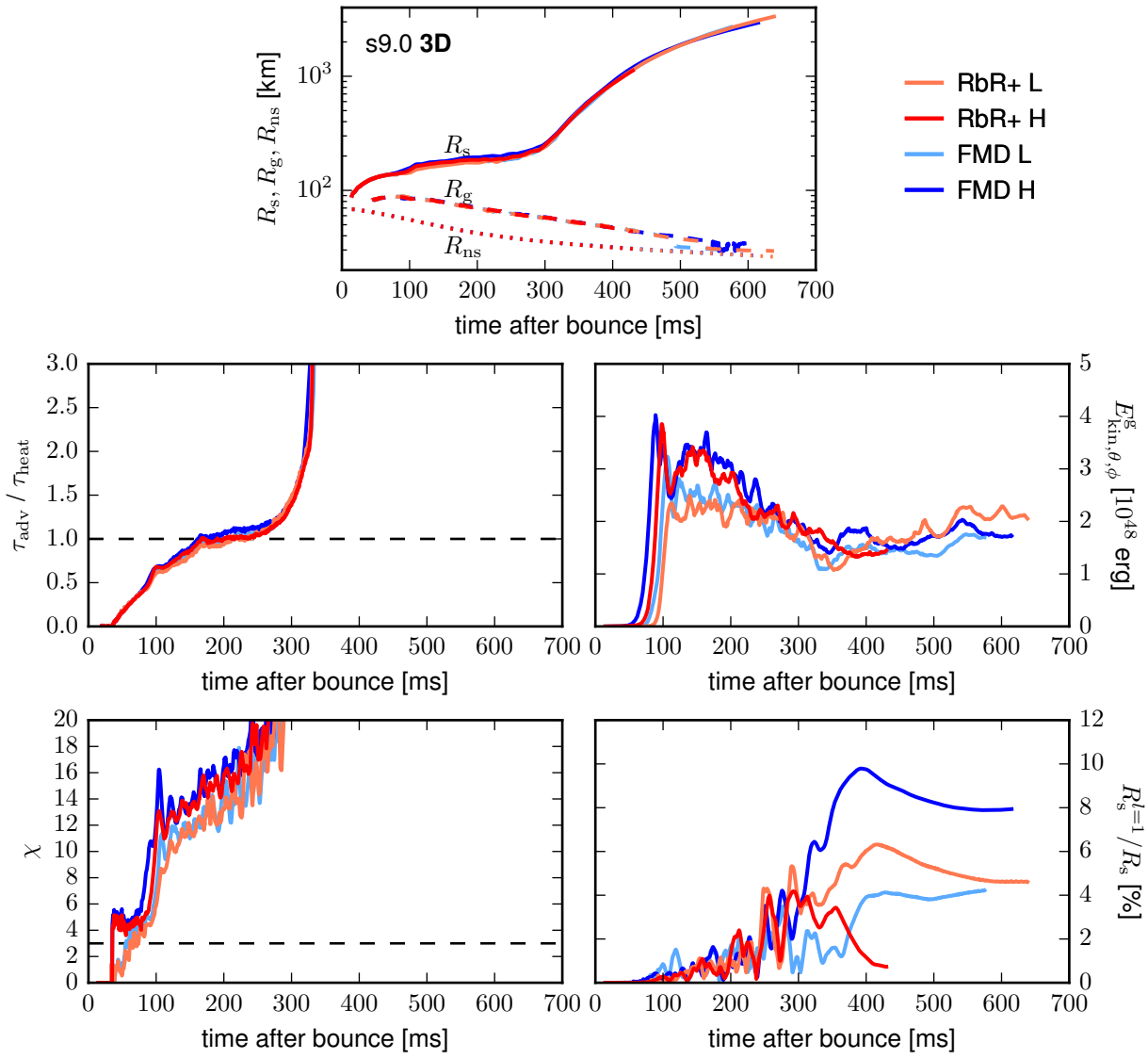

Figure 3.11.: Overview of all 3D simulations of the s9.0 progenitor model. Shown are, as functions of the time after bounce, the angle-averaged shock radii R_s (solid lines), gain radii R_g (dashed lines), and neutron-star radii R_{ns} (dotted lines; all in the top panel), the ratios of advection to heating timescale τ_{adv}/τ_{heat} (center left panel), the non-radial kinetic energies in the gain layer $E^g_{kin,\theta,\phi}$ (center right panel), the χ parameters (bottom left panel), and the dipole moments of the angle-dependent shock radii $R_s^{l=1}$, normalized to corresponding values of the monopole moments R_s (bottom right panel). The different line colors correspond to low- (suffix "L") and high-resolution (suffix "H") simulations with either the FMD neutrino-transport scheme or the RbR+ approximation (see legend). This figure is a slightly rearranged version of Figure 13 from Glas et al. (2019b).

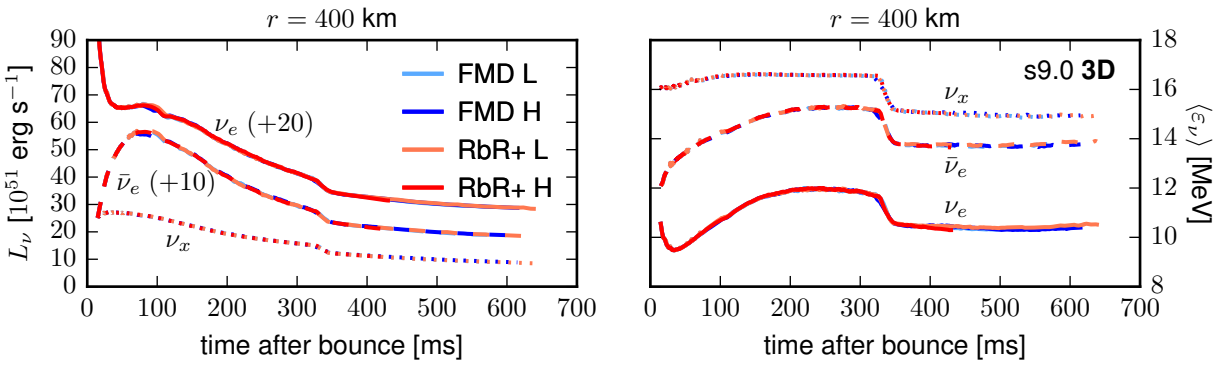

Figure 3.12.: Neutrino luminosities L_ν (left panel) and neutrino mean energies $\langle \varepsilon_\nu \rangle$ (right panel) as functions of the time after bounce for all 3D simulations of the s9.0 progenitor model. Luminosities and mean energies are measured at a radius of $r = 400$ km in the co-moving frame of the stellar fluid. Different line styles show electron neutrinos ν_e (solid lines), electron antineutrinos $\bar{\nu}_e$ (dashed lines) and heavy lepton neutrinos ν_x (dotted lines). To facilitate readability of the plot some lines were shifted vertically indicated by the numbers giving the shifts in units of the ordinate. This figure is a slightly rearranged version of Figure 14 from Glas et al. (2019b).

Figure 2.3), we find relatively long advection timescales and, thus, favorable conditions for the growth of convection in all simulations of the s9.0 model. Correspondingly, all simulations exhibit χ parameters considerably larger than the critical value of 3 starting at roughly 100 ms after bounce (bottom left panel). For this reason, all simulations of the s9.0 progenitor model stay convection-dominated and do not exhibit any obvious SASI activity until the end of the simulations. Remarkably, we observe the dipole moments of the shock deformation to reach amplitudes up to 10 % of the monopole moments (bottom right panel), triggered mainly by large-scale convective plumes in the post-shock layer. All in all, we do not find any major differences between all four 3D simulations of the s9.0 progenitor model, neither between low- and high-resolution simulations, nor between RbR+ and FMD neutrino transport.

Figure 3.12 shows the co-moving frame neutrino luminosities (left panel) and mean energies (right panel) for all three neutrino species at a radius of $r = 400$ km. Again, the agreement between all four simulations is excellent. Shortly after shock expansion at about 300 ms p.b., both neutrino luminosities and mean energies significantly drop due to the decline of the mass accretion onto the neutron star. As a result of continued cooling of the hot proto-neutron star, both neutrino luminosities and mean energies exhibit almost constant values (decreasing only slowly with time) until the end of our simulations.

Compared to our 2D simulations of the s9.0 model (see Section 3.2 and Figure 3.3), the 3D models exhibit a slightly earlier drop of the neutrino luminosities, i.e., at ~ 320 ms p.b. instead of ~ 380 ms – 420 ms p.b. in 2D simulations, resulting from slightly earlier shock expansion and a larger shock radius in 3D, which correlate with initially higher turbulent kinetic energies in the gain layer pushing the shock farther out. Furthermore, the shock radii show larger variations between simulations in 2D, whereas 3D simulations display a very good agreement.

3.4.2. Diagnostic Explosion Energies

Additional differences between 2D and 3D simulations of the s9.0 progenitor model appear in the diagnostic explosion energies. These are defined as the total energy in the gain layer (see

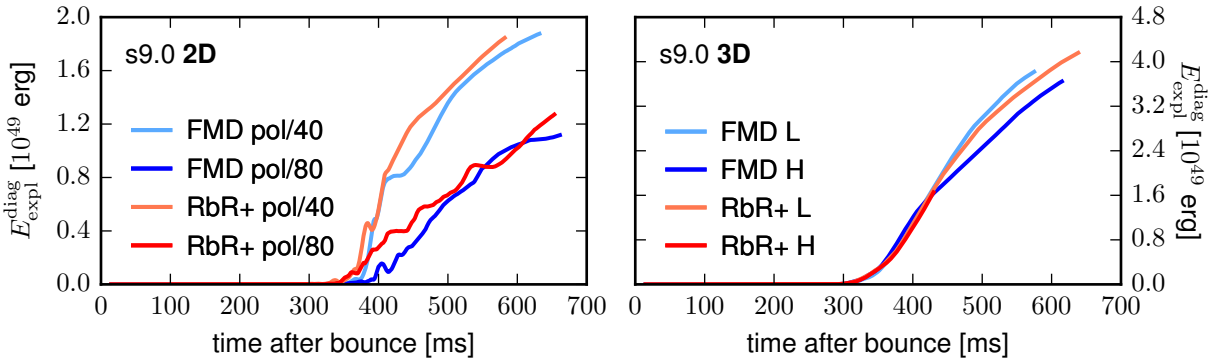

Figure 3.13.: Diagnostic explosion energies $E^{\rm diag}_{\rm expl}$ in dependence on the time after bounce for all 2D (left panel) and 3D (right panel) simulations of the s9.0 progenitor model. The range of the ordinate differs between top and bottom panels. This figure is a slightly rearranged version of Figure 15 from Glas et al. (2019b).

Equation (3.2)),

$$E^{\rm diag}_{\rm expl} = \int_{V_{\rm ps}} \rho \left(e_{\rm int} + \frac{v^2}{2} + \phi_{\rm grav} \right) {\rm d}V, \tag{3.19}$$

with the difference that the integral over the post-shock volume $V_{\rm ps}$ extends from $R_{\rm ns}$ to $R_{\rm s}(\theta, \phi)$, and that only zones where the total energy is positive are included in the integral. Figure 3.13 shows the diagnostic explosion energies for all 2D (left panel) and 3D (right panel) simulations of the s9.0 model. Our 3D simulations result in diagnostic explosion energies that almost reach (models 'FMD L' and 'FMD H') and even exceed (model 'RbR+ L') a value of 4×10^{49} erg, when measured at roughly 600 ms after bounce (note that explosion energies have not attained their terminal values at that time, and that model 'RbR+ H' was not simulated that long). In contrast, 2D simulations exhibit explosion energies that are systematically smaller by a factor 2 to 3 and start rising slightly later (in correspondence to the later outward acceleration of the shock in 2D). A similar trend of lower explosion energies in 2D than in 3D simulations was found by Melson et al. (2015b), who performed CCSN simulations of a low-mass progenitor model with a mass of 9.6 $\rm M_\odot$ and zero metallicity, and by Müller (2015) for simulations of an 11.2 $\rm M_\odot$ model.

Furthermore, the diagnostic explosion energies in 2D are higher in the low-resolution compared to the high-resolution simulations by almost 0.8×10^{49} erg, which is a result of larger post-shock volumes in the low-resolution models after roughly 400 ms (compare the evolution of angle-averaged shock radii in Figure 3.3). With the small sample of 2D simulations for the s9.0 model available, it is not clear to us whether this 2D difference is connected to resolution differences per se, or to the non-equidistant angular grid. In 3D, the considerably smaller differences of the diagnostic explosion energies stem from the morphology of the post-shock layer, while the angle-averaged shock radii are very similar between simulations (see Figure 3.11). Model 'FMD H' exhibits the most extreme shock deformation, which is evident from the fact that the dipole mode in this model is larger than in all other models (see Figure 3.11). This difference is probably caused by stochastic variations, and leads to the smallest post-shock volume and, therefore, the lowest diagnostic energy in model 'FMD H'.

3.4.3. Summary

We find an excellent agreement of the post-bounce evolution of the s9.0 progenitor model for all of our 3D simulations. Only small differences exist between simulations with low and high grid resolutions with respect to the initial growth of the non-radial kinetic energies in the gain layer and concerning the evolution of the diagnostic energies. Differences between 3D simulations with the RbR+ approximation and the FMD neutrino-transport scheme are negligible for the s9.0 progenitor model.

3.5. Conclusions: FMD versus RbR+

For the first time, we directly compared self-consistent CCSN simulations in 3D with the RbR+ approximation for neutrino transport and an FMD transport scheme to assess the influence of the two transport methods on the neutrino-heating mechanism in 3D. Our time-dependent simulations with "low" and "high" grid resolution (roughly 4.5° and 2.25° non-equidistant angular spacing, respectively) for a $9\,M_\odot$ and a $20\,M_\odot$ progenitor model were performed with the radiation-hydrodynamics code Aenus-Alcar, which implements an energy- and velocity-dependent, FMD two-moment neutrino-transport scheme with an algebraic "M1" closure relation for ν_e, $\bar{\nu}_e$, and ν_x, and which is able to employ the RbR+ approximation by setting all non-radial flux components to zero.

For both progenitor models we found very good agreement of the post-bounce evolution between 3D simulations with RbR+ and the FMD neutrino-transport scheme. Our 3D simulations of the $9\,M_\odot$ model result in successful shock revival at roughly 300 ms after bounce with diagnostic explosion energies reaching 4×10^{49} erg (and still growing by $\sim 10^{50}$ erg) when evaluated at 600 ms after bounce. In contrast, with our simplified neutrino opacities and small initial seed perturbations (used to initiate the growth of hydrodynamic instabilities), all 3D simulations of the $20\,M_\odot$ model fail to revive the stalled shock wave until at least 400 ms after bounce.

These findings contrast results from 2D simulations in which the RbR+ approximation has been shown to foster shock revival in models that featured strong sloshing motions of SASI along the polar symmetry axis (Skinner et al., 2016; Just et al., 2018). While our 2D simulations of the $20\,M_\odot$ model are dominated by such axial sloshing motions, the 3D simulations exhibit alternating phases of convective and SASI activity and, thus, show a substantially different post-bounce evolution than corresponding 2D simulations. In contrast, simulations of the $9\,M_\odot$ model are dominated by convection in both 2D and 3D and do not exhibit any obvious SASI activity.

Considering surface-integrated neutrino luminosities and mean energies, we found very good agreement of the results for all neutrino species between the 3D simulations of each progenitor model. Although angular variations of the radial neutrino fluxes differ between simulations with RbR+ and FMD, as a detailed analysis of the $20\,M_\odot$ model revealed (confirming previous investigations by Sumiyoshi et al. 2015), the 3D simulations systematically exhibit significantly smaller variations than corresponding 2D cases. Furthermore, the time-averaged (over typically 10 ms or longer) deviations of the radial fluxes and the neutrino-heating rates from their angular averages are in good agreement between 3D simulations with RbR+ and FMD. Moreover, the neutrino-heating rates near the instantaneous SASI direction agree considerably better between 3D simulations with RbR+ and FMD than in 2D models, in which fluctuations of the heating rates in the polar directions are much larger with RbR+ transport. Therefore, aside from stochastic fluctuations in the shock radius, the overall evolution for both progenitor models is very similar in 3D with FMD and RbR+ transport. Our results show that the differences between 3D models with different resolution is larger than the differences with the two transport treatments.

In conclusion, the post-bounce evolution of 3D simulations with the RbR+ approximation and the FMD neutrino-transport scheme agrees much better than between corresponding 2D models. These results back up the use of RbR+ as transport description in 3D supernova modeling. The RbR+ approximation is beneficial regarding the parallel efficiency, because the individual rays can be calculated almost independently with only small communication overhead between MPI (Message Passing Interface) tasks. However, the preferred choice of neutrino-transport approximation strongly depends on the physical question that should be answered. For example, the FMD scheme provides approximative representations of the non-diagonal elements of the neutrino-pressure tensor, which may be relevant for some problems but cannot be directly extracted from a RbR+ treatment. Another example are fast rotating progenitor models, where the use of the RbR+ approximation is disfavored, when the proto-neutron star becomes strongly deformed and non-radial flux components cannot be neglected in the neutrino-decoupling region near the neutron-star surface. In the study by Summa et al. (2018) the rotation rate and neutron-star deformation were not sufficiently extreme to worry about deficiencies of the RbR+ treatment. A clear picture of shortcomings in dependence of the neutron-star rotation will require future comparisons of rapidly rotating models with RbR+ transport versus FMD transport. However, the good physical accuracy of the "M1" FMD scheme in such situations is also not guaranteed and needs to be verified by full Boltzmann neutrino transport.

In general, an ultimate assessment of the consequences of transport approximations entering both the FMD as well as RbR+ two-moment treatments will require future, computationally much more demanding time-dependent 2D and 3D CCSN simulations with Boltzmann neutrino transport. For first low-resolution steps in this direction, see Sumiyoshi et al. (2015) and Nagakura et al. (2018).

Chapter 4.

Effects of LESA in 3D Simulations

In this chapter, we analyze our set of eight 3D simulations of CCSNe for the consequences of the two neutrino-transport methods (FMD and RbR+) on the recently discovered LESA phenomenon. After a description of the key features of LESA in Section 4.1, we compare the behavior of LESA in FMD and RbR+ models in Section 4.2. In Section 4.3 we discuss a global, dipolar flow pattern in the proto-neutron star associated with LESA, followed by a short summary in Section 4.4 of our attempt in Glas et al. (2019a) to establish a connection between LESA and Chandrasekhar's linear theory of thermal instability in spherical shells. We conclude this chapter in Section 4.5. The contents of this chapter have already been published in Glas et al. (2019a, see also the information on already published material on page 73).

4.1. The LESA Phenomenon

Tamborra et al. (2014a) and Janka et al. (2016) reported the discovery of a large hemispheric asymmetry of the total electron lepton-number emission from the newly formed neutron star in a set of 3D CCSN simulations, which made use of the RbR+ approximation to treat the multi-dimensionality of the neutrino transport, thereby ignoring the non-radial components of the neutrino flux vector. They termed this stunning, new phenomenon "lepton-number emission self-sustained asymmetry" (LESA). It is characterized by a substantial amplitude of the dipole component (in some cases and phases even exceeding the monopole) of the lepton-number flux, which is defined by the difference of the radial number flux of electron neutrinos and antineutrinos at spatial point $\boldsymbol{r}$,

$$F_{\mathrm{lnf}}(\boldsymbol{r}) = \bar{F}^r_{N,\nu_e}(\boldsymbol{r}) - \bar{F}^r_{N,\bar{\nu}_e}(\boldsymbol{r}). \tag{4.1}$$

The radial number flux of any neutrino species ν is given by (compare Equation (A.4b))

$$\bar{F}^r_{N,\nu} = \int F^r_\nu \, \varepsilon^{-1} \, \mathrm{d}\varepsilon, \tag{4.2}$$

with the radial energy-flux density F^r_ν (see Equation (2.6b)) and the neutrino energy ε. Both the dipole amplitude and the direction of this dipole were observed to exhibit basically stationary or slowly migrating behavior over time intervals of at least several hundred milliseconds covered by the simulations.

In contrast, Dolence et al. (2015) did not observe any evidence for LESA when carrying out 2D CCSN simulations with a multi-group, flux-limited diffusion scheme for neutrino transport. For this reason, Sumiyoshi et al. (2015) speculated that LESA may be an artifact of the RbR+ approximation. In a later study, Vartanyan et al. (2018) also did not find indications of LESA when conducting 2D simulations with a fully multi-dimensional two-moment scheme. However, Tamborra et al. (2014a) argued that the behavior of LESA was considerably different between their 2D and 3D models. While in the 2D case the LESA dipole direction, which can only be aligned

with the artificial axis of symmetry, flips between both polar directions on a time scale of some 10 ms, strongly affected by SASI mass motions around the proto-neutron star, only their 3D models showed a persistent and directionally stable LESA dipole.

Roberts et al. (2016) also investigated their 3D simulations with a fully multi-dimensional two-moment neutrino-transport scheme for effects of LESA, but could not trace any evidence of this phenomenon. Although their models did not take into account velocity-dependent terms in the neutrino-moment equations and ignored inelastic neutrino scattering on electrons, this group interpreted the absence of LESA in contrast to the supernova models of Tamborra et al. (2014a) not necessarily as a consequence of these differences in the neutrino treatment. Instead, Roberts et al. (2016) hypothesized that it could be linked, for example, to the fact that neutron-star convection showed up rather late in their simulations.

The first independent confirmation of the LESA phenomenon in 3D CCSN models with detailed neutrino transport different from those of the Garching group has recently been reported by O'Connor and Couch (2018b), and it has been witnessed in 3D simulations by Vartanyan et al. (2019a) and, possibly, Vartanyan et al. (2019b). Both groups also applied a fully multi-dimensional two-moment scheme, for which reason their results provide support for LESA not being an artifact of the RbR+ transport approximation. Although O'Connor and Couch (2018b) observed a substantial LESA dipole only in their single full-sphere calculation including velocity-dependent terms in the transport, they argued that the appearance of LESA is not directly linked to this improvement but appears to be a consequence of the stronger proto-neutron star convection seen in the model with velocity dependence. This conclusion may offer an explanation why LESA was absent in the models of Roberts et al. (2016), and it is consistent with the finding by Janka et al. (2016) that LESA is weaker in rotating and further diminished in rapidly rotating models, because angular momentum gradients in the neutron star suppress convective activity.

In order to shed more light on the rather unclear situation pictured by the diverse (but not necessarily conflicting) results of the presence or absence of LESA in models reported in the literature, we also evaluate our 3D simulations for signatures of LESA. We can exploit the unique possibility to directly assess the influence of the neutrino-transport schemes, FMD vs. RbR+, by analyzing our set of eight new 3D simulations for an exploding $9\,\mathrm{M}_\odot$ progenitor and a non-exploding $20\,\mathrm{M}_\odot$ star (see Table 2.3 for an overview, and Chapter 3 for a discussion of the post-bounce dynamics of all models). In all of these eight simulations, we find clear evidence for the LESA with all of its characteristic properties described by Tamborra et al. (2014a) and Tamborra et al. (2014b).

4.2. LESA in FMD and RbR+ Models

4.2.1. Amplitude and Direction of the Dipole Mode

We first perform a multipole analysis and decompose the radial lepton-number flux in the laboratory frame (i.e., the rest frame of the stellar center),

$$F^{\mathrm{lab}}_{\mathrm{lnf}} = \bar{F}^{r}_{N,\mathrm{lab},\nu_e} - \bar{F}^{r}_{N,\mathrm{lab},\bar{\nu}_e}, \tag{4.3}$$

into real spherical harmonics, Y_l^m, of degree l and order m (see Equation (3.10)). The radial number fluxes of neutrinos ν in the lab frame are obtained by the transformation (dropping the subscript ν; compare the general case in Equation (A.6b))

$$\bar{F}^{r}_{N,\mathrm{lab}} = \bar{F}^{r}_{N} + v^{r}\ \bar{N}, \tag{4.4}$$

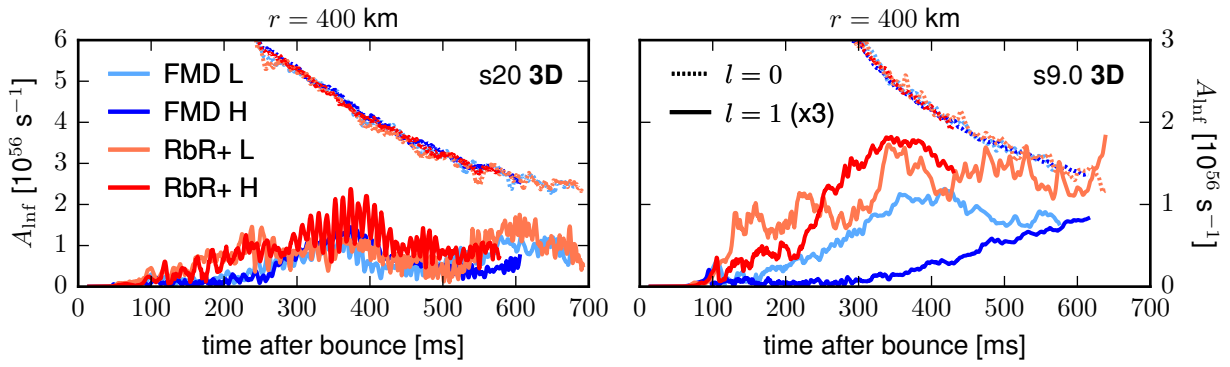

Figure 4.1.: Monopole ($l = 0$, dotted lines) and dipole ($l = 1$, solid lines) moments of the electron lepton-number flux, evaluated at a radius of $r = 400\,\mathrm{km}$ and transformed into the lab frame at infinity, as functions of time after core bounce for all 3D simulations of the s20 (left panel) and the s9.0 (right panel) progenitor models. The multipole amplitudes A_{lnf} are defined as given in Equation (4.7). While for $l = 0$ the corresponding amplitude agrees with the total electron lepton-number flux, the plot shows the dipole amplitude of Equation (4.7) scaled by a factor of 3 for consistency with the normalization used by Tamborra et al. (2014a): $A_0 + A_1 \cos\vartheta$ with A_0 and A_1 being the monopole and dipole amplitudes, respectively, and ϑ the angle relative to the dipole direction. This figure is a slightly rearranged version of Figure 1 from Glas et al. (2019a).

where v^r is the radial fluid velocity and $\bar{N}$ is the number density of neutrinos in the co-moving frame (compare Equation (A.4a)),

$$\bar{N} = \int E\,\varepsilon^{-1}\,\mathrm{d}\varepsilon. \tag{4.5}$$

The multipole coefficients at a given radius r are calculated by integrating the flux over the whole spherical surface:

$$c_l^m(r) = \sqrt{\frac{4\pi}{2l+1}} \int r^2 F_{\mathrm{lnf}}^{\mathrm{lab}} Y_l^m\,\mathrm{d}\Omega. \tag{4.6}$$

The moments of the lepton-number flux are then obtained as

$$A_{\mathrm{lnf}}(r,l) = \sqrt{\sum_{m=-l}^{l} \left[c_l^m(r)\right]^2}. \tag{4.7}$$

Here, we use a normalization for which the monopole moment, $A_{\mathrm{lnf}}(r,0)$, is identified with the total lepton-number flux through the surface of a sphere with radius r[1].

Figure 4.1 displays the time-dependent evolution of the amplitudes of the monopole ($l = 0$, dotted lines) and of the dipole ($l = 1$, solid lines, scaled by a factor of 3 compared to Equation (4.7)) of the total electron lepton-number flux (evaluated as lab-frame quantities at a radius of $r = 400\,\mathrm{km}$) for

[1] We point out that the normalization of the spherical harmonics coefficients in the present case differs from what we used for the decomposition of the shock radius in Section 3.3 (see Equations (3.12) and (3.13)). There, all coefficients R_{s}^l are rescaled by a factor of $1/(4\pi)$ compared to $A_{\mathrm{lnf}}(r,l)$. With this normalization the monopole moment stands for the mean shock radius.

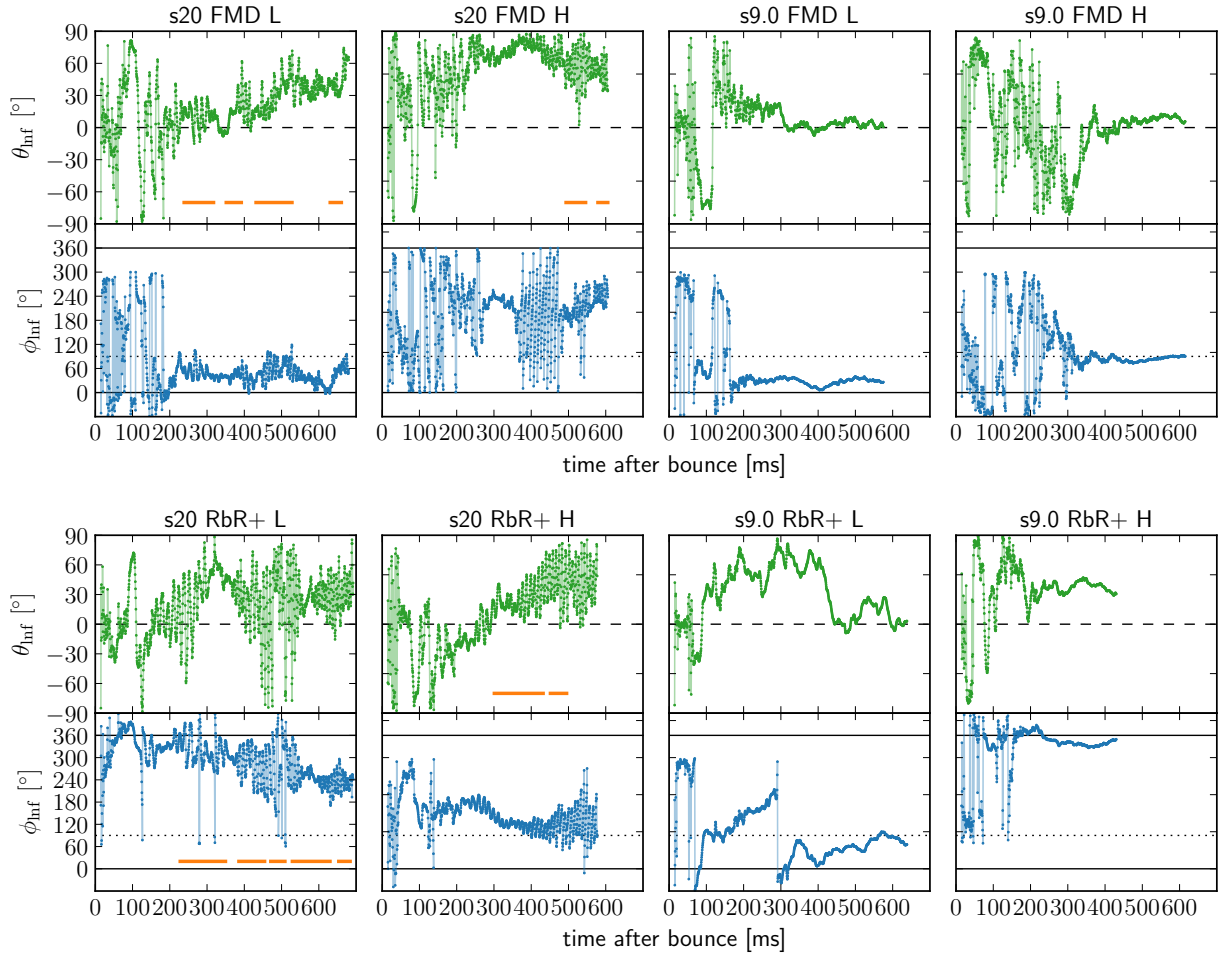

Figure 4.2.: Time evolution of the direction of the electron lepton-number flux dipole (i.e., of the amplitude of the $l = 1$ moment plotted in Figure 4.1) for all 3D simulations in terms of the polar angle θ_{lnf} (green dots connected by shaded lines) and the azimuthal angle ϕ_{lnf} (blue dots connected by shaded lines) of the dipole vector. The top panels shows the FMD runs with low and high resolution for the s20 and s9.0 progenitors, and the bottom panels show the corresponding RbR+ results. For better readability the values of the polar angle are transformed to range within the interval $\theta_{\mathrm{lnf}} \in [-90°, 90°]$, which implies that the equator is located at $\theta_{\mathrm{lnf}} = 0°$ (dashed black line). Moreover, some values of the periodic azimuthal angle are shifted by adding or subtracting 360° in some panels. The x and y directions of an associated Cartesian coordinate system correspond to $\phi_{\mathrm{lnf}} = 0°$ (or, equivalently, $\phi_{\mathrm{lnf}} = 360°$, solid black lines) and $\phi_{\mathrm{lnf}} = 90°$ (dotted black lines), respectively. Note that for directions very close to the poles, i.e. $\theta_{\mathrm{lnf}} \sim \pm 90°$, variations of the azimuthal angle ϕ_{lnf}, e.g. in model 's20 FMD H' between ~ 350 ms and ~ 500 ms after bounce, describe migrations within a small area around the poles. This is obvious from Figure 4.3, where the evolution of the dipole directions for all high-resolution simulations is visualized in terms of Aitoff projections of the angle space. The time intervals marked by orange horizontal bars roughly indicate SASI episodes. This figure is taken from Glas et al. (2019a, Figure 2).

all our 3D simulations. To visualize the evolution of the dipole direction, the polar and azimuthal angles of the dipole vector[2] are shown as functions of time after bounce in Figure 4.2.

All our simulations, both with RbR+ and FMD neutrino transport, exhibit dipole components that grow with time and reach between $\sim 10\,\%$ and more than $30\,\%$ (keeping in mind the scaling in Figure 4.1 by a factor of 3) of the monopole amplitude at the end of the calculations. While the individual characteristics of the evolution differ from model to model, a clear correlation can be observed in all cases between the time when the dipole amplitude reaches a substantial fraction of the monopole and the time when the direction of the dipole approaches a fairly stable state with only slow and modest subsequent migration. This can be most clearly seen in the CCSN runs for the s9.0 progenitor, for example around 200 ms p.b. in models 's9.0 FMD L' and 's9.0 RbR+ H', and at ~ 350 ms in 's9.0 FMH H', whereas in model 's9.0 RbR+ L' the latitudinal angle reaches a well-defined value after about 100 ms while the azimuthal angle continues to drift until ~ 350 ms p.b. But this motion takes place in a rather small region around the pole of the grid since $\theta_{\rm lnf} \gtrsim 70°$ (compare Figures 4.1 and 4.2).

In the s20 runs the dipole direction also has the tendency to evolve more slowly after an initial phase of basically random motion during the period when the amplitude still grows. However, different from the convection-dominated post-shock layer in the s9.0 models, the post-bounce dynamics of the s20 runs is characterized by repeated episodes of violent SASI activity. As shown by Tamborra et al. (2014a), the LESA dipole is mostly formed in the convective layer interior of the proto-neutron star and further enhanced by the lepton-number loss from the accretion layer around the neutrinosphere, where the electron fraction develops a pronounced hemispheric asymmetry. For this reason Tamborra et al. (2014a), Tamborra et al. (2014b), and Walk et al. (2019) observed that SASI-induced variations of the accretion flow between stalled shock and neutron star and the associated time- and direction-dependent modulations of the accretion luminosity (mostly ν_e plus $\bar{\nu}_e$) can have a considerable impact on the evolution of the LESA dipole. This influence of SASI on LESA is strongest when the LESA direction coincides with the plane or even the direction of the SASI sloshing or spiral motions. Regarding the interplay between SASI and LESA, we do not witness any obvious dependence on the employed transport method.

The corresponding effects can be clearly spotted in the s20 runs, see Figure 4.1 (upper panel) and Figure 4.2, where phases exist when both the dipole amplitude and the direction angles exhibit pronounced oscillations. These oscillations correlate with episodes of strong SASI activity in the post-shock layer (see Section 3.3 and Figure 3.4). The overlap of SASI and LESA directions is particularly evident in model 's20 RbR+ H', where between about 200 ms and 450 ms after bounce the LESA dipole and the SASI direction are roughly aligned as visible in the upper right panel of Figure 4.3. Exactly during this time interval the LESA dipole amplitude (Figure 4.1) shows large quasi-periodic modulations and both direction angles of the LESA dipole exhibit a major shift by $\sim 90°$ instead of the usual temporal fluctuations, which seem to be a consequence of the time- and directional variability of the massive accretion flows to the neutron star in the non-exploding s20 models (Figure 4.2). While the ubiquitous temporal fluctuations of the direction angles are also present in model 's20 FMD H', this case does not display any quasi-monotonic large-scale migration of the LESA direction at $t_{\rm pb} \gtrsim 250$ ms except for local motions around the pole at $\theta_{\rm lnf} = 90°$, signaled by large excursions of $\phi_{\rm lnf}$ between ~ 350 ms and ~ 500 ms after bounce. This is compatible with the fact that in model 's20 FMD H' the LESA dipole direction is far off the main plane of

[2] For the dipole direction of the lepton-number flux, we use the multipole coefficients $c_1^m(r)$ as components of the direction vector, which we then transform into spherical polar coordinates. This procedure is equivalent to the analysis of the dipole direction of the shock radius (see Equations (3.12) and (3.13) and the associated explanations in Section 3.3).

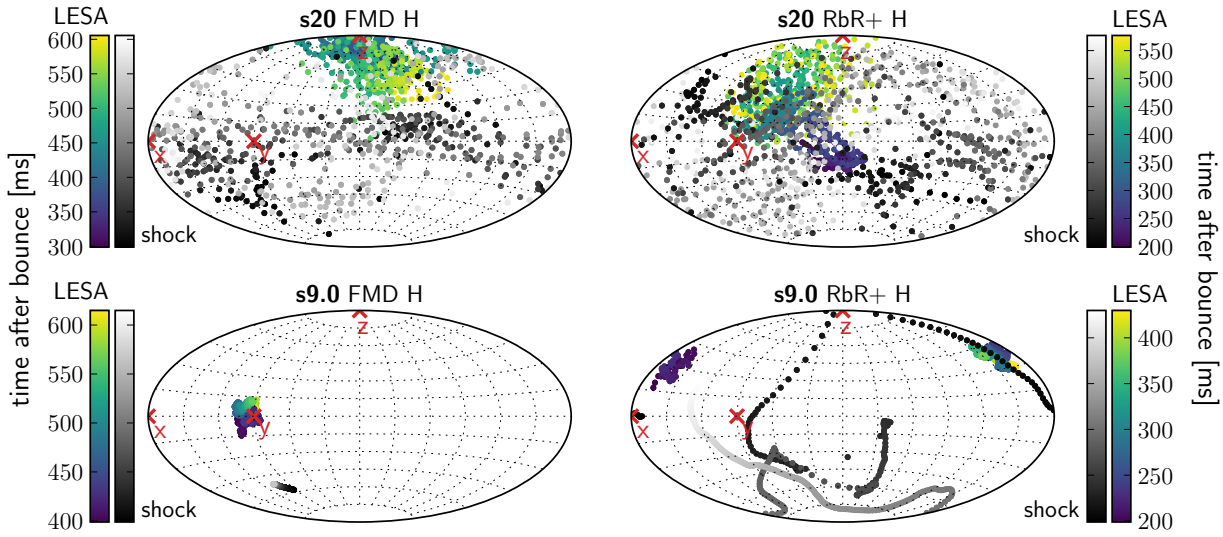

Figure 4.3.: Time evolution of the directions of the electron lepton-number flux (LESA) dipole and of the dipole vector of the deformed shock surface for all high-resolution 3D simulations visualized by Aitoff projections of the angle space. In the case of the s20 progenitor the shock dipole mainly corresponds to an asphericity of the shock caused by violent SASI sloshing and spiral motions, which also lead to direction-dependent modulations of the neutrino luminosity due to asymmetric accretion of the neutron star. The dots mark the location of the dipoles at certain times with the colors from blue to yellow for the LESA dipole and dark gray to light gray for the shock dipole indicating the direction of time (see color bars). The time intervals of the displayed evolution differs between the different panels, covering in each case the phase of the most pronounced LESA dipole. The axis directions x, y, and z of the Cartesian coordinate system, underlying the definition of the direction angles used in Figure 4.2, are marked by red crosses. In the convection-dominated s9.0 models (bottom panels) SASI plays no role. The dipole deformation mode of the shock is caused by asymmetric convection and has hardly any influence on the LESA dipole. In model 's20 FMD H' (upper left panel) SASI mass motions and accretion asymmetries occur in a plane roughly perpendicular to the LESA dipole, whose amplitude and orientation are therefore affected less strongly by the SASI-induced neutrino-emission modulations than in model 's20 RbR+ H' (upper right panel), where the LESA and SASI dipole directions coincide temporarily. The alignment of the dipole direction with the y-axis in model 's9.0 FMD H' (lower left panel) is just accidental, because the transformation from spherical polar coordinates to Cartesian coordinates in the x-y-plane is arbitrary. This figure is taken from Glas et al. (2019a, Figure 3).

SASI activity during most of the time (see upper left panel in Figure 4.3). For the Aitoff projections of the SASI direction in the latter figure we consider the dipole vector associated with the shock deformation[3], following Tamborra et al. (2014a). Alternatively, Tamborra et al. (2014b) employed the dipole of the neutrino-energy flux, summed over all six neutrino species. The spatial motions of both direction vectors are closely correlated, and both can therefore be used equally well as tracers of the SASI motions and of the associated accretion-modulated anisotropic neutrino emission, which then has an impact on the LESA dipole.

In contrast, the runs of the s9.0 progenitor explode rather early ($t_{\rm pb} \sim 300\,{\rm ms}$) and do not possess

[3]We use the multipole coefficients $a_x = a_1^1$, $a_y = a_1^{-1}$, and $a_z = a_1^0$ from the decomposition of the angle-dependent shock radius into real spherical harmonics (see Equations (3.12) and (3.13) and the associated explanations in Section 3.3) as components of the direction vector, which we then transform into spherical polar coordinates.

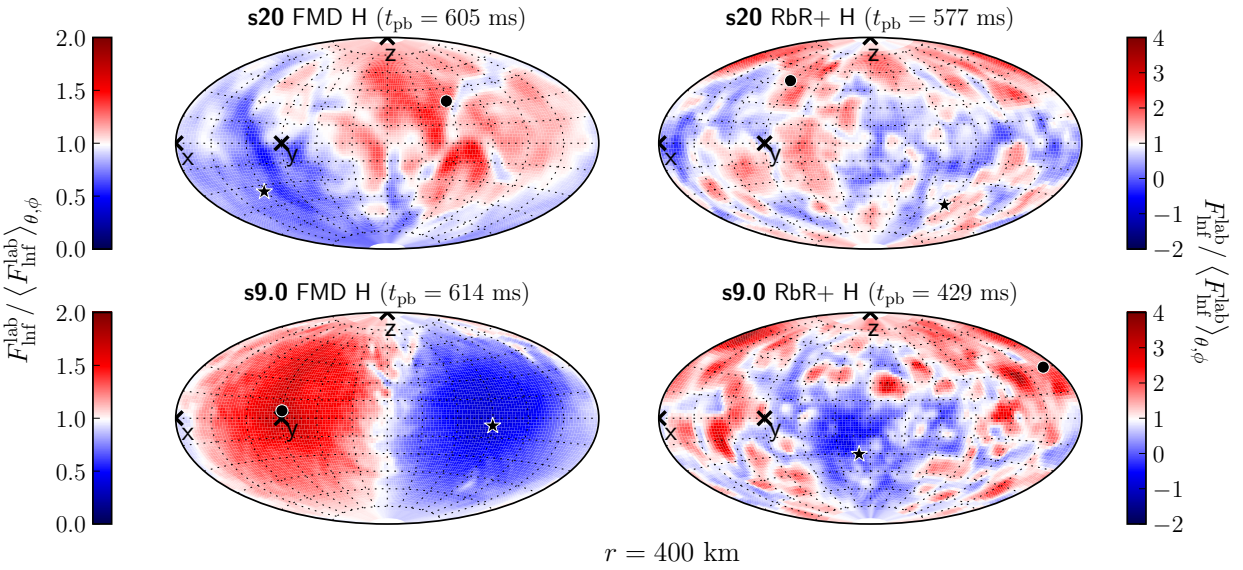

Figure 4.4.: Aitoff projections of the electron lepton-number flux, $F^{\rm lab}_{\rm lnf}$ (see Equation (4.3)), evaluated at a radius of $r = 400\,$km, transformed into the lab frame at infinity, and normalized by the angular average, $\langle F^{\rm lab}_{\rm lnf} \rangle_{\theta,\phi}$ (see Equation (3.15c)). The results are displayed for all high-resolution 3D runs (arrangement of panels analogous to Figure 4.3) at the end of each simulation (given by $t_{\rm pb}$ in the figure labels). The directions of the LESA dipole moments (see final results in Figures 4.2 and 4.3) are marked by circles, the opposite directions by stars. The dominance of a dipole asymmetry is visible in all cases, but the spottiness of the RbR+ results suggests more important contributions also from higher-order multipoles. This is confirmed by the "spectrograms" shown in Figure 4.5. The exceptionally clear hemispheric difference in model 's9.0 FMD H' (and the very stable dipole direction seen in Figure 4.3) result from (1) the absence of SASI and the low mass-accretion rate in downflows in this exploding model, (2) the "smearing" of angular variations by the non-radial flux components that are evolved in the FMD scheme, but neglected in the RbR+ transport, and (3) the fact that 's9.0 FMD H' is shown at a time of evolution when the LESA dipole mode is largest and strongly dominates the higher multipoles (see Figures 4.1 and 4.5). For orientation, also the x, y, and z directions of the Cartesian coordinate system for the measurement of the dipole angles of Figure 4.2 are indicated by black crosses. This figure is taken from Glas et al. (2019a, Figure 4).

any preceding SASI activity. Moreover, convective fluctuations of the mass-accretion rate also have a much reduced influence on the neutrino emission in these simulations because of the low mass-accretion rate of this low-mass progenitor. For these reasons the LESA amplitude (Figure 4.1, lower panel) and direction angles (Figure 4.2, two right columns and Figure 4.3, bottom panels) do not show any phases of quasi-periodic oscillations as in the s20 models, and the LESA vector is more stationary or shifts only slowly on longer timescales.

4.2.2. Analysis of the Higher Modes

Figure 4.4 presents the variations of the local electron lepton-number flux densities in all emission directions for all high-resolution 3D simulations at the times when the runs were terminated. The dominance of a dipolar mode is visible in all cases, but also contributions from higher multipolar models can be recognized. This is confirmed by Figure 4.5, which provides "spectrograms" for the temporal evolution of the moments $A_{\rm lnf}$ from order $l = 1$ up to $l = 10$ for the same set of simulations. Both of the models with FMD transport exhibit an early phase between $\sim 50\,$ms p.b. and $\sim 200\,$ms

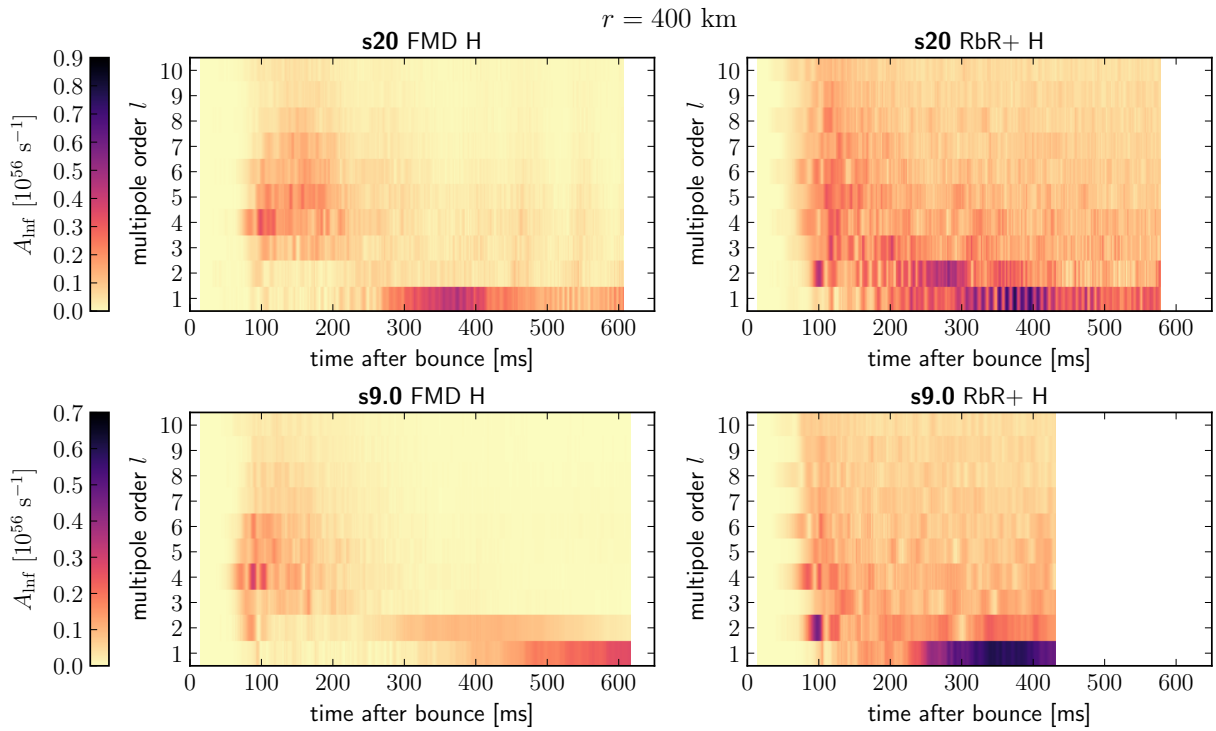

Figure 4.5.: "Spectrograms" for the time evolution of the multipole moments A_{lnf} of the electron lepton-number flux (as defined in Equation (4.7)) for orders $l = 1$ to $l = 10$ (evaluated at a radius of $r = 400\,\mathrm{km}$ for an observer in the lab frame at infinity). Results from all our four high-resolution 3D simulations are displayed (arranged analogously to the panels in Figures 4.3 and 4.4). The color intensity scales with the multipole amplitude (see color bars). To optimize the visualization of the relative strengths of the moments for $l \geq 1$, the monopole ($l = 0$), which would far dominate the early post-bounce evolution, is not displayed. This figure is taken from Glas et al. (2019a, Figure 5).

p.b. in which only the multipole modes around $l = 4$ are excited. The growth of these asymmetries coincides with the time when convective activity inside of the proto-neutron star sets in ($t_{\mathrm{pb}} \sim 40\,\mathrm{ms}$ – $50\,\mathrm{ms}$), whereas non-radial instabilities in the gain layer start only some 10 ms later (at $\gtrsim 70\,\mathrm{ms}$ – $80\,\mathrm{ms}$ p.b., see the non-radial kinetic energies given in Figure 3.4). A dominant dipole begins to appear in 's20 FMD H' at $t_{\mathrm{pb}} \gtrsim 250\,\mathrm{ms}$, at which time 's9.0 FMH H' develops most strength in the quadrupole mode, before after $\sim 450\,\mathrm{ms}$ of post-bounce evolution also in this model the dipole becomes the clearly dominant mode, as prominently visible in the lower left panel of Figure 4.4. At the end of both runs the dipole has by far the highest amplitude of all modes with $l \geq 1$.

Also in the simulations with RbR+ transport the modes of higher orders between $l = 4$ and $l = 6$ appear first, the quadrupole mode reaches a dominant amplitude several 10 ms afterwards, and the dipole mode even $\sim 150\,\mathrm{ms}$ – $200\,\mathrm{ms}$ later. And also similar to the FMD runs, as time goes on there is an obvious tendency that the power in the mode spectrum shifts to lower and lower modes until the dipole has the highest amplitude. Different from the FMD runs, for which the lepton-flux asymmetry at $t_{\mathrm{pb}} \gtrsim 250\,\mathrm{ms}$ – $300\,\mathrm{ms}$ is distinctly concentrated in the $l = 1$ and $l = 2$ modes, the RbR+ models possess a broader distribution of power in the spectrograms. The higher moments, $l > 1$, always yield visible contributions and their power decreases gradually with higher values of l. This is fully compatible with the flux variations seen in Figure 4.4, where the RbR+ cases exhibit a fragmented pattern of larger and smaller spots (i.e., of lower and higher multipole

orders), superimposed on the hemispheric (dipolar) asymmetry.

This observation, however, is not really astonishing in view of the fact that the RbR+ approximation ignores non-radial components of the neutrino fluxes and therefore variations in the directions perpendicular to the radius vector remain more localized on smaller scales. In contrast, the non-local behavior of radiative transfer with the FMD scheme, which couples spatial volumes over a neutrino mean free path, leads to a "smearing" of angular variations by the non-radial flux components. This produces much smoother radiation characteristics around the neutrinosphere and above it, as discussed in Section 3.3 and as visible in Figures 3.7 and 3.8. Therefore large-scale or global directional variations of the neutrino emission such as accretion-induced hemispheric asymmetries and the LESA phenomenon can be captured in their basic properties by both FMD and RbR+ transport treatments, whereas small-scale variations are stronger with RbR+ transport.

4.2.3. Assessment: FMD versus RbR+

A more detailed comparison reveals further differences between the results from the two treatments, though none of these differences is of fundamental nature. For example, the simulations with RbR+ show a somewhat earlier rise of the LESA dipole component for both progenitor models than in the corresponding FMD cases. Moreover, in the s9.0 models the dipole amplitudes reach somewhat higher maximal values in the RbR+ calculations. Although this does not apply to the s20 runs, the SASI-induced modulations of the LESA dipole seem to be more extreme in the RbR+ cases, in particular in model 's20 RbR+ H' (Figure 4.1). But these modulations depend sensitively on the orientation of the LESA dipole relative to the SASI direction, which is stochastic and differs from model to model and can also vary during the post-bounce evolution of a single run. The migration of the dipole (or its directional stability), although difficult to compare in detail, does not reveal any qualitatively different behavior between RbR+ and FMD simulations.

Overall, we conclude that the LESA phenomenon with its characteristic features is shared by all of our 3D models. This disproves speculations that LESA is a numerical artifact of the RbR+ approximation. Our results are consistent with those reported by Tamborra et al. (2014a), Tamborra et al. (2014b), and Janka et al. (2016), where LESA was discussed as a lepton-number emission self-sustained asymmetry first. Since a key feature of LESA is a dipole emission component that grows relative to the monopole, it shall be noted that during the phases when the dipole dominates the higher-order multipoles, the absolute value of the total electron lepton-number flux (the monopole) in our s20 models is higher by a factor of $\gtrsim 2$ than in the simulations with the Vertex code presented by Tamborra et al. (2014a). This discrepancy might stem from differences in the neutrino-interaction rates, which are considerably more elaborate in many aspects in the calculations with Vertex. It could also be a consequence of a different contraction behavior of the neutron star in response to different energy and lepton-number loss through neutrino radiation. Moreover, proto-neutron star convection is substantially stronger in calculations with the Alcar code as discussed by Just et al. (2018). All of these aspects can directly or indirectly influence the production and the convective and radiative transport of lepton number inside of the neutron star and can thus have an effect on the relative strength of the monopole and dipole of the electron lepton-number emission.

The detailed temporal evolution of LESA strongly depends on the simulation setup, including the neutrino-transport method, the grid resolution, and the progenitor model. Although the onset of lepton-emission asymmetries is seen at roughly the same time in all our models, with $l \sim 4$–6 modes showing the fastest growth, the subsequent evolution that leads to the emergence of a dominant LESA dipole could depend also on stochastic initial seeds and a stochastically-triggered complex feedback mechanism between asymmetric neutron-star convection and mass accretion of lepton-rich

material as described by Tamborra et al. (2014a) and Janka et al. (2016). Further analysis is needed, based on a future, larger pool of 3D simulations with varied physics inputs and numerical treatments of hydrodynamics and neutrino transport. In this context it is assuring that O'Connor and Couch (2018b) and Vartanyan et al. (2019b,a) also observed the LESA phenomenon in their 3D simulation with two-moment transport including velocity-dependent terms.

4.3. LESA and Proto-Neutron Star Convection

A detailed description of the characteristic empirical features of the LESA phenomenon was provided by Tamborra et al. (2014a) and Janka et al. (2016), whose results were confirmed by the analysis of our current models in Section 4.2 (see also O'Connor and Couch 2018b; Vartanyan et al. 2019b,a). As mentioned above and discussed in the previous works, the major contribution to the dipole emission originates from the convective layer inside of the neutron star, whose hemispheric differences in the lepton-number loss rate can be further amplified by an asymmetry in the mass-accretion flow from the SN shock to the neutron star.

4.3.1. Visualization of the Asymmetries and Cell Patterns

The directional dependence of the convective cell pattern and of the lepton-number flux density in the interior of the neutron star can be seen in the volume renderings of Figure 4.6. Both fiducial high-resolution models with FMD transport ('s20 FMD H', top panels, and 's9.0 FMD H', bottom panels) show a pronounced hemispheric asymmetry for large (red) and small (blue) values of the lepton-number flux density around the spherical region at roughly 10 km (red sphere in the center), measured at the times when the LESA dipole mode resides at the maximum value for each model. The volume rendering was performed for the lepton-number flux density in the lab frame, $F_{\mathrm{lnf}}^{\mathrm{lab}}$, which connects to the co-moving frame lepton-number flux density via Equations (4.3) and (4.4). Since in the neutrino-diffusion regime (which well applies to the convective layer in the proto-neutron star) the second term on the right hand side of Equation (4.4) dominates by far, the red bubbles in Figure 4.6 mainly visualize the velocities of the convective cells, demonstrating a clear hemispheric asymmetry. Because these asymmetries in the proto-neutron star are quite similar between the two fiducial simulations, we pick only one of them (model 's20 FMD H') for the following analysis.

In the volume-rendered images of Figure 4.6, the lepton-number flux density is displayed through semitransparent isosurfaces that are picked by choosing non-vanishing transparency for selected flux-density values (see the grey markers at the color bar of each panel). The inner red sphere corresponds to the spherical lepton-number flux that diffuses out from the non-convective central core. The red plumes visualize the pattern of small-scale convective cells that fill the convection layer of the proto-neutron star and become visible because $F_{\mathrm{lnf}}^{\mathrm{lab}}$ depends on the radial fluid velocity through the second term on the right hand side of Equation (4.4). Stronger convection in the hemisphere pointing in the LESA direction (which is indicated by the green arrows in the tripod of each panel) and weaker convection in the opposite direction are obvious from the larger red plumes in the former case and the smaller and less distinct plumes in the latter case. These hemispheric differences in the strength of overturn activity in the proto-neutron star convection layer lead to the pronounced dipolar asymmetry of the lepton-number flux exterior to the convective shell, which is visualized by the enveloping, cap-like blue surfaces.

The bottom panels of Figure 4.6 together with Figure 4.7 demonstrate that the LESA direction has no obvious correlation with the deformation that develops in the expanding post-shock ejecta. This can be understood by the fact that the LESA asymmetry is large (of order tens of percents)

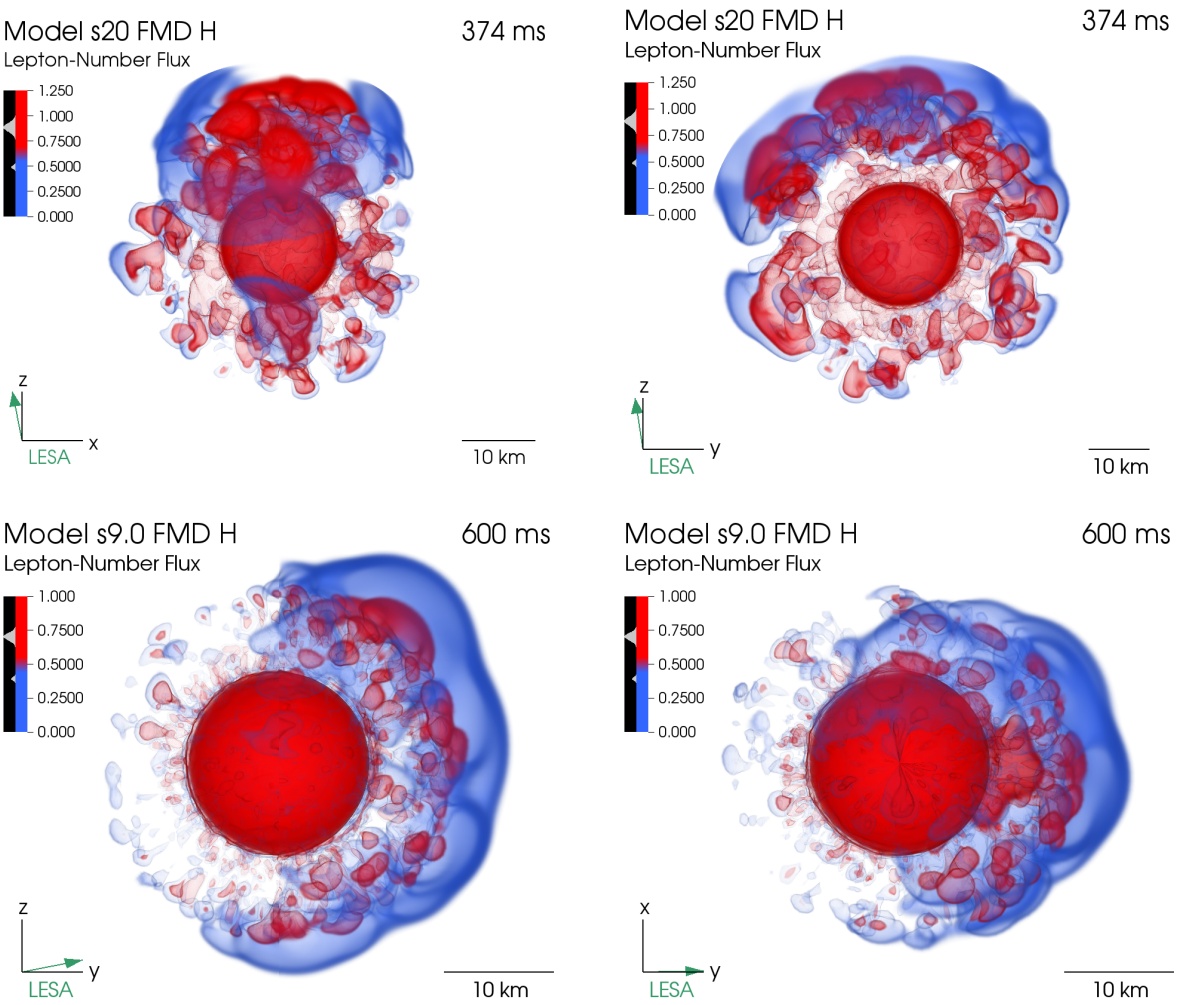

Figure 4.6.: Volume renderings of the electron lepton-number flux density in the lab frame, $F_{\mathrm{lnf}}^{\mathrm{lab}}$ (see Equations (4.3) and (4.4), in units of $\mathrm{s}^{-1}\,\mathrm{cm}^{-2}$ and scaled down by a factor of 10^{43}), in the interior of the neutron star (see yardstick in the lower right corner of each panel). For model 's20 FMD H' (top panels) we show data at 374 ms after bounce, and for model 's9.0 FMD H' (bottom panels) we pick a snapshot at 600 ms, which is close to the end of the simulation. At these times, the LESA dipole mode resides near its largest value for each model (compare Figure 4.1). The LESA dipole direction, indicated by a green arrow in the tripod in the lower left corner of each panel, roughly aligns with the $+z$-direction in model 's20 FMD H', and the $+y$-direction in model 's9.0 FMD H' (compare Figure 4.3). The left and right panels depict different planes, which in all cases contain the LESA vector (see the tripods). Since in the neutrino-diffusion regime the visualized lepton-number flux densities are vastly dominated by the velocity-dependent term in Equation (4.4), the images display the hemispheric differences of the small-scale convective cells (visible as red plumes) that fill the convection layer in the proto-neutron star. The convective cells are much more extended, and convectively enhanced lepton-number transport is much stronger (visible by the blue, hemispheric "caps"), on the side of the higher lepton-number emission. Opposite to this LESA dipole, convection is weaker and the convective cells are less distinct, indicating less efficient convective lepton-number transport. Our volume renderings are therefore 3D visualizations of the situation displayed by cross-sectional images in Figure 10 of Tamborra et al. (2014b). This figure is taken from Glas et al. (2019a, Figure 6).

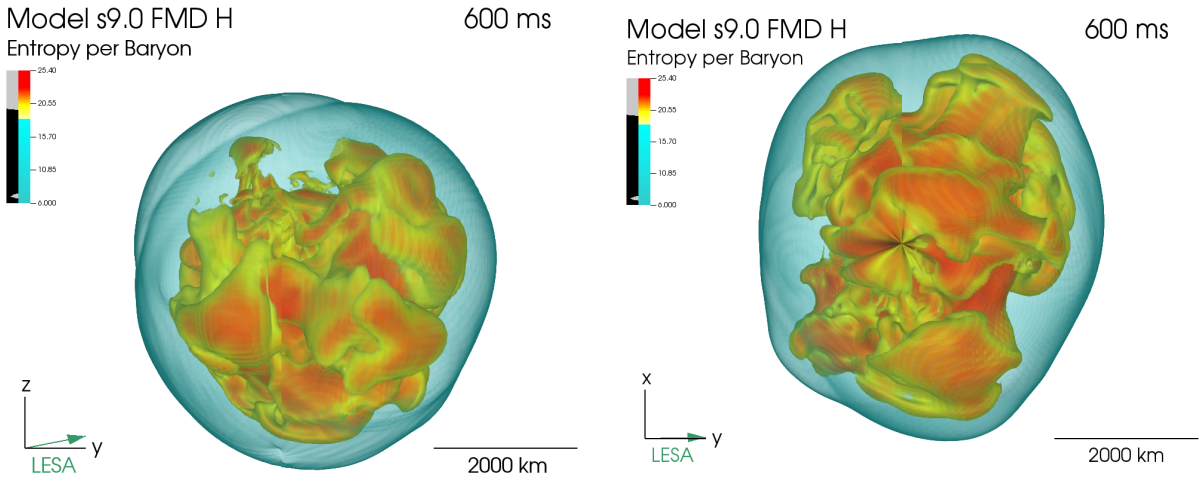

Figure 4.7.: Visualization of the explosion geometry by means of the entropy per baryon (in units of k_B) for model 's9.0 FMD H'. The volume renderings show the shock front (turquoise layer) and plumes of neutrino-heated matter in the post-shock layer (yellow and orange surfaces) for a temporal snapshot at 600 ms close to the end of the simulation. The left and right panels depict different planes (see the tripod in the lower left corner of each panel). We emphasize that the LESA direction nearly coincides with the y-axis (indicated by the green arrows in the tripods), and that there is no correlation between the LESA direction (see Figure 4.6) and the global deformation of the expanding post-shock material. The streak-like pattern in the center of the right panel is a well-known artifact for viewing directions along the polar axis, arising from the transformation from spherical polar coordinates to the Cartesian coordinate system of the visualization tool. This figure is taken from Glas et al. (2019a, Figure 7).

in the lepton-number flux, but small (on the level of a few percent only) in the total number and energy flux of ν_e plus $\bar{\nu}_e$ (see Tamborra et al. 2014a,b). Therefore, since (ν_e plus $\bar{\nu}_e$)-emission asymmetries due to accretion have mostly a larger amplitude, LESA has no dominant direct impact on the growth of neutrino-heated bubbles, and therefore on explosion asymmetries.

Figure 4.8 displays a zoom of the interior of the neutron-star and its immediate surroundings in our 3D model 's20 FMD H'. The cross-sectional plane chosen for the plots is close to the axis of the LESA dipole. The upper left panel shows the radial component of the lepton-number flux in the laboratory frame (i.e., the rest frame of the stellar center), $F_{\mathrm{lnf}}^{\mathrm{lab}}$ (see Equation (4.3)), scaled with the surface area $4\pi r^2$, at $t_{\mathrm{pb}} = 374\,\mathrm{ms}$, which is about the time when the LESA dipole reaches its maximum (see Figure 4.5, upper left panel). The higher lepton-number flux in the northern hemisphere is correlated with an excess of the electron fraction, Y_e, compared to its angular average at each radius (upper right panel). This pattern associated with LESA (Tamborra et al., 2014a) grows within the convective layer, which extends from the edge of the white circular region indicating the 10 km core that is computed in 1D, to the outer boundary of the convective layer, which roughly coincides with the effective energy sphere of muon and tau neutrinos (dotted black circle in the upper right panel). The LESA ν-emission and Y_e asymmetries continue within the overlying radiative shell, where faster neutrino diffusion carries the leptons to the neutrinospheres of ν_e and $\bar{\nu}_e$ (solid and dashed black circles, respectively), and persist into the accretion layer exterior to the neutrinospheres.

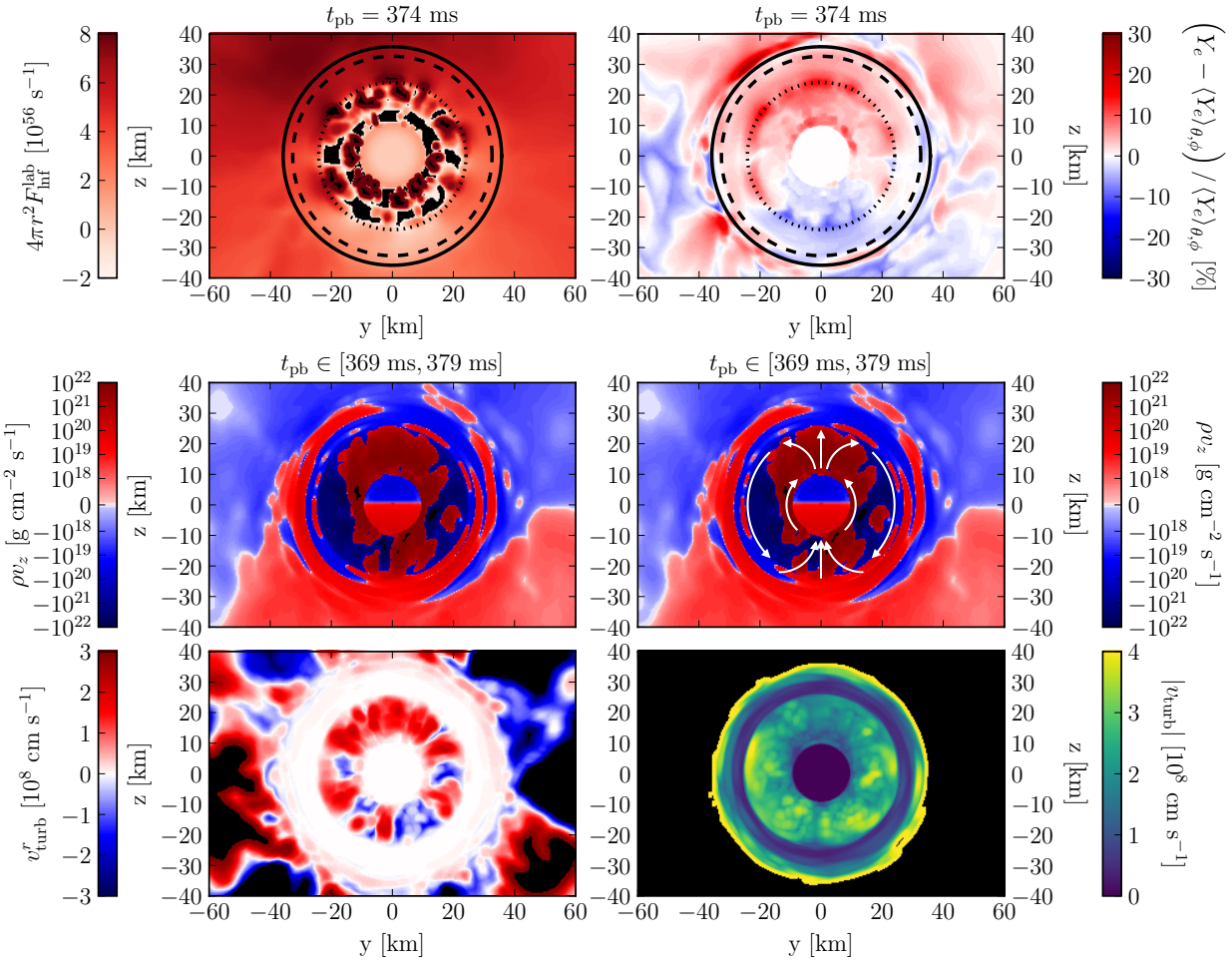

Figure 4.8.: Asymmetries associated with the LESA phenomenon inside and around the neutron star in 3D model 's20 FMD H'. The six panels provide different quantities in the cross-sectional y-z-plane, which contains the polar axis of our spherical polar grid and cuts through the neutron star very close to the axis of the LESA dipole (see Figure 4.3). The LESA direction points (roughly) to the 12 o'clock position in all panels. The upper left panel displays the radial component of the electron lepton-number flux $F^{\rm lab}_{\rm lnf}$, transformed to an observer in the rest frame of the stellar center (see Equation (4.3)) and scaled by the surface area $4\pi r^2$. The upper right panel shows spatial variations of the electron fraction Y_e, normalized by the angular average $\langle Y_e(r) \rangle_{\theta,\phi}$ (see Equation (3.15c)). The white circular region around the center corresponds to the innermost 10 km, which are computed in spherical symmetry. Both plots show a post-bounce time of $t_{\rm pb} = 374$ ms. Black circles indicate the effective energy spheres of all neutrino species (as defined in Equation (3.17)), solid for ν_e, dashed for $\bar{\nu}_e$, and dotted for ν_x. The middle panels visualize the z-component of the mass-flux density, ρv_z, averaged over the time interval of $t_{\rm pb} \in [369\,{\rm ms}, 379\,{\rm ms}]$. The white arrows in the middle right panel sketch the underlying flow pattern, forming a dipolar mode within the convective layer of the neutron star. The lower panels show the cell structure in the convective layer by means of the turbulent radial velocity $v^r_{\rm turb}$ (left) and the absolute turbulent velocity $|v_{\rm turb}|$ (right), both averaged over the time interval of $t_{\rm pb} \in [369\,{\rm ms}, 379\,{\rm ms}]$. Values that exceed the range of the corresponding color bar of each panel appear in black. The global dipolar flow pattern visible in the middle panels, which encompasses the whole proto-neutron star convection layer, is superimposed on the familiar pattern of smaller-scale convective cells filling the convective shell as visible in the lower panels. These convective cells possess a hemispheric asymmetry in the LESA dipole direction with larger and more extended outflow structures on the side of the higher lepton-number flux, which is obvious from the bottom panels and which can also be concluded from the visualization of the lab-frame lepton-number flux density in Figure 4.6 and in the cross-sectional plots of Figure 10 in Tamborra et al. (2014a). This figure is taken from Glas et al. (2019a, Figure 8).

4.3.2. Global Dipolar Flow Pattern in the Neutron Star

The effective flow pattern that is responsible for these hemispheric differences in the lepton-number transport out from the deep inner core of the proto-neutron star is displayed in the middle panels of Figure 4.8, where the component of the mass flux in the north-south (z) direction, ρv_z, is visualized by color coding.

The bottom panels of Figure 4.8 show the familiar cell pattern of the convective layer in the proto-neutron star. The characteristic convective feature associated with LESA is stronger outflow in the hemisphere pointing in LESA direction and stronger convective inflow in the opposite hemisphere, visible in the bottom left panel from the positive and negative radial components of the turbulent velocities, which are defined by

$$v_{\mathrm{turb}}^{r} = v_r - \langle v_r \rangle_{\theta,\phi}\,, \tag{4.8}$$

where $\langle v_r \rangle_{\theta,\phi}$ is the angular average of v_r (see Equation (3.15c)). In contrast, the absolute values of the convective velocities,

$$v_{\mathrm{turb}} = \sqrt{(v_r - \langle v_r \rangle_{\theta,\phi})^2 + v_\theta^2 + v_\phi^2}, \tag{4.9}$$

may not display any clear correlation with the LESA dipole direction (see bottom right panel of Figure 4.8; but also Walk et al. 2019).

Superimposed on the smaller-scale convective variations (see the pattern of convective cells in the upper left panel and in the bottom panels of Figure 4.8), a global dipolar flow can be identified, indicated by the white arrows in the middle right panel: Around the north pole lepton-rich plasma rises through the convective layer, transporting electron-lepton number from the inner core to regions closer to the neutrinospheres, where the high electron abundance causes enhanced ν_e emission. Matter with decreasing Y_e streams along the outer edge of the convective layer from the north pole towards the south pole, further losing lepton number by radiating ν_e. Near the south pole the flow of neutron-rich, specifically (i.e., per nucleon) heavier and thus denser matter submerges again to deeper layers, where it is channeled into currents that stream back towards the northern hemisphere along the inner border of the convective layer. On its way from south to north, the plasma is refueled with fresh leptons by absorbing neutrinos diffusing out from the high-density core.

4.3.3. Influence of the 1D Core

A deficiency of the present models in connection to this analysis of LESA should be mentioned here. The 1D core with a chosen radius of 10 km, which is employed in our 2D and 3D simulations for reasons of computational efficiency (see Section 2.6.3), turned out to be too large during the later post-bounce evolution of our models. At times beyond about 200 ms after bounce, the inner boundary of the convective layer hits the radius of the 1D core (see Figure 4.9), and correspondingly, the spherically symmetric treatment of the 1D core prevents the convective shell to grow deeper. The 2D calculations of Just et al. (2018), where the s20 progenitor was run with the same input physics but with a considerably smaller 1D core, demonstrate that the inner boundary of the convective shell reaches a radius of $\sim$ 10 km already after about 150 ms and becomes as small as $\sim$ 7 km after 500 ms.

We confirm this finding in a similar analysis of two 2D simulations. Figure 4.9 shows the inner boundary of the neutron star convection layer, r_{i}, which is defined as the radius at which the angle-averaged, non-radial velocities exceed $10^7\,\mathrm{cm\,s^{-1}}$. In addition to data from the 3D model ‘s20

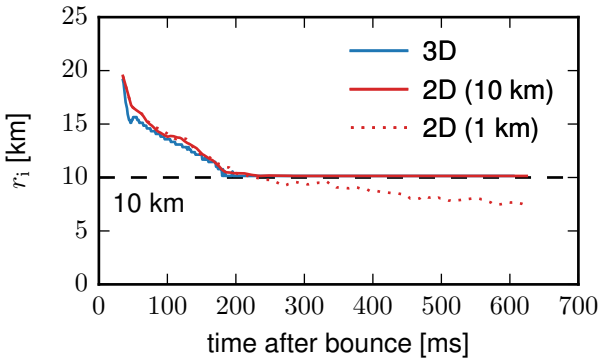

Figure 4.9.: Influence of the 1D core on the convective layer in the proto-neutron star. We show, as a function of the post-bounce time, the inner radius of the convective region, r_i, for the 3D model 's20 FMD H' (blue line), and for two 2D reference simulations with spherical symmetric cores of 10 km (red solid line) and 1 km (red dotted line), respectively. The horizontal dashed lines at 1 km and 10 km indicate the boundary of the core that is computed in spherical symmetry instead of 2D or 3D for reasons of numerical efficiency. This figure is inspired by the upper left panel of Figure 9 from Glas et al. (2019a).

FMD H' (blue line), we show r_i also for two 2D reference simulations of the s20 progenitor model, one with a spherically symmetric core of the same size of 10 km as in the 3D simulations (red solid line), and the other one with a much smaller core of only 1 km (red dotted line). In the latter case, the region of convection moves only very slowly into the neutron star down to 7 km to 7.5 km by the end of the simulation at 600 ms after bounce. In contrast, the 2D simulation with a 10 km core behaves similarly to the 3D simulation, with r_i touching 10 km starting from 200 ms.

It is therefore clear that the use of the spherical core has constrained the later growth of the proto-neutron star convection layer in the simulations of the present work. Potentially, this might even have prevented a growth of the LESA dipole beyond the amplitudes obtained in our models. Nevertheless, the basic features of the LESA phenomenon agree well with the results reported by Tamborra et al. (2014a) and Janka et al. (2016) from calculations with the Prometheus-Vertex code, where the 1D core was as small as $\sim$ 1.5 km and had no impact on the development of neutron-star convection. Evaluating the available set of 3D models from the Prometheus-Vertex runs, Stockinger (2015) also observed a dipolar flow pattern that encompasses the convective layer in the neutron star and transports electron lepton-number from one hemisphere to the other, very similar to the one visible in Figure 4.8.

4.4. Chandrasekhar's Theory of Thermal Instability

The presence of a dipolar flow pattern through and around the convection zone of the proto-neutron star motivated us to investigate whether this finding can be understood under the paradigm of Chandrasekhar's linear stability analysis for spherical shells (Chandrasekhar, 1961). In this section, we summarize our study presented in Glas et al. (2019a), which aimed at establishing a connection between the growth of neutron-star convection and Chandrasekhar's theory. We refer the reader to Section 5 of Glas et al. (2019a) and Section VI of Chandrasekhar's book (Chandrasekhar, 1961) for more details.

In his work, Chandrasekhar determined the critical conditions for the onset of thermal instability in fluid spheres and spherical shells on the basis of a linear stability analysis for a variety of situations. He concludes that a given system becomes unstable against convection for perturbations of the

spherical harmonics mode l with the lowest value of the critical Rayleigh number. This means that at marginal stability the convective pattern will manifest itself in a certain l-mode, when the Rayleigh number of the system exceeds the critical Rayleigh number $\mathcal{R}_{C,l}$ for this mode. It further means that for Rayleigh numbers lower than the critical Rayleigh number for a mode l, disturbances of this mode are expected to be stable, while such disturbances will become unstable when the Rayleigh number exceeds $\mathcal{R}_{C,l}$.

Bearing in mind Chandrasekhar's theory, we analyzed the conditions for convective instability inside the neutron star in our 3D model 's20 FMD H', and compared the growth behavior of different multipoles against the predictions from Chandrasekhar's linear stability analysis. This assessment can, of course, only be tentative because of the substantial differences between the complex physical conditions in the Ledoux-unstable neutron-star layer compared to the idealized terrestrial setups investigated by Chandrasekhar. Despite these limitations, the growth behavior of the different multipoles of the lepton-number flux (which we relate to multipoles of the flow in the convective layer) follows amazingly well the expectations from Chandrasekhar's theory. We conclude this from comparing the Rayleigh numbers for different l-modes of the system[4]—which we estimate at the center of the convective layer, at the times when we identify the initial rise of an l-mode emission asymmetry—with the corresponding critical Rayleigh numbers $\mathcal{R}_{C,l}$ derived by Chandrasekhar. In agreement with the mathematical analysis, we witness the onset of modes around $l = 4$ first. The growth of the other multipole modes sets in at times when the Rayleigh numbers for the conditions of the system follow the critical curve for $\mathcal{R}_{C,l}$ adopted from Chandrasekhar (1961). Since the Rayleigh number of the convective layer continues to rise monotonically even after the dipole mode ($l = 1$) appears for the first time, one can expect its presence also at later times. Hence, the existence of a dipolar flow pattern in the proto-neutron star convection layer seems compatible with Chandrasekhar's analysis of thermal instability in spherical shells.

4.5. Conclusions for LESA

We presented an in-depth analysis of the effects of LESA in our set of eight 3D CCSN runs for two progenitors. LESA was first witnessed as a dipolar electron lepton-number emission asymmetry by Tamborra et al. (2014a) in their 3D simulations with RbR+ neutrino transport, which neglects the non-radial components of the neutrino fluxes. Recently, LESA was also seen in various 3D simulations with FMD neutrino transport performed by O'Connor and Couch (2018b, one model), Vartanyan et al. (2019b, possibly one model), and Vartanyan et al. (2019a, all eleven simulations). We observed the appearance of a strong LESA dipole mode after some 100 ms p.b. in all of our models, for exploding $9\,M_\odot$ and non-exploding $20\,M_\odot$ cases, both with lower and doubled grid resolution, and with FMD as well as RbR+ neutrino transport.

All characteristic features of LESA reported by Tamborra et al. (2014a) and Tamborra et al. (2014b) were also diagnosed in the present models: (1) phases where the dipole component of the lepton-number flux clearly dominates all higher-order multipoles and can reach even the strength of the monopole; (2) a relatively stable position or only slow migration of the dipole direction during the phases of a strong dipole; (3) corresponding hemispheric differences in the strength of proto-neutron star convection and in the electron and lepton fractions in the convection layer and above it; (4) a hemispheric asymmetry of the accretion layer between deformed shock and neutron star with greater accretion on the side of the higher lepton-number flux; (5) SASI-induced

[4]Calculating the Rayleigh number requires the specification of the kinematic viscosity of the fluid. In our current models, viscous effects are far dominated (by a factor of ~ 10 to 100) by numerical viscosity. This needs to be kept in mind when numerical simulations are evaluated for the growth of LESA multipole modes.

modulations of the LESA dipole in periods of strong SASI activity, when the LESA dipole is located close to the direction of SASI sloshing or close to the plane of SASI spiral motions.

Our results clearly prove that LESA is *not* an artifact of the RbR+ approximation. Nevertheless, there are interesting differences between the FMD and RbR+ results in certain aspects. The LESA dipole amplitudes with RbR+ neutrino transport tend to grow noticeably faster, reach higher amplitudes earlier, and their maximum amplitudes can, at least temporarily, be higher than those obtained with FMD transport. However, the dipole, once fully developed, dominates the multipole spectra of the lepton-number flux in the FMD cases in a much cleaner way than in the RbR+ runs (although it can be somewhat lower compared to the monopole). The spectrograms of the RbR+ models typically show prominent quadrupoles as well, and significant power over a wider range of higher-order multipoles. This patchiness of the directional variations of the lepton-number emission is expected as a natural consequence of the more localized neutrino effects in the RbR+ approximation (see the discussion in Chapter 3, in particular Section 3.3.4). In contrast, the neutrino field leaving the convective layer is smoothed in the surrounding radiative shell by non-local radiation-transport effects of FMD.

Closely inspecting the mass flows in and around the convection layer interior to the proto-neutron star during phases of a strong LESA dipole, we reveal a global, volume-filling dipolar pattern that streams around the central, convectively stable core. These currents effectively transport lepton-rich matter from the hemisphere opposite to the LESA dipole direction to the hemisphere in the LESA dipole direction, and from deeper regions to layers closer to the neutrinospheres. An important effect is the gain or loss of electron lepton-number by these currents through exchange with diffusion fluxes (via neutrino absorption or emission) when the gas flow moves along the inner and outer boundaries between the convective layer and the diffusive central core on the one side and the enveloping shell on the other side. This exchange process fuels and defuels the lepton content of the currents.

Our reported work has attempted to achieve progress towards a better understanding of the puzzling LESA phenomenon. Despite the assuring result that the existence of a dipolar flow pattern in the neutron-star convection layer seems compatible with Chandrasekhar's linear stability analysis of thermal instability in spherical shells (Chandrasekhar, 1961), the detailed reason for the dominance of the $l = 1$ mode remains unclear. Previous speculations that it is driven by feedback effects with a hemispheric accretion asymmetry around the neutron star (Tamborra et al., 2014a), or by an amplifying feedback cycle connected to $Y_{\rm lep}$-dependent differences of Ledoux convection in opposite neutron star hemispheres (Janka et al., 2016), require corroboration by future investigations.

Moreover, plenty of future work will have to address the consequences of LESA in the context of supernova explosions and their detectable neutrino emission. Interpreting our present results (and those of previous reports of LESA in the literature) we would not think that LESA has any significant impact on the supernova mechanism and the "explodability" of progenitor stars. On the one hand, the LESA asymmetry concerns mainly the lepton-number flux but much less the total (number and energy) flux of electron neutrinos and antineutrinos (see Tamborra et al. 2014a,b), for which reason the emission asymmetry has a subordinated consequence on the neutrino heating in the post-shock layer. LESA effects in this respect seem to be overruled by SASI- and convection-induced perturbations and modulations, which is reflected by the fact that SASI activity in our $20\,M_\odot$ runs has considerable implications for the stability of the LESA direction and amplitude (see also Tamborra et al. 2014b). The assessment of probable implications of LESA for neutron star kicks and supernova nucleosynthesis (as mentioned already by Tamborra et al. 2014a) and possible implications for explosion energies will require much longer simulations than performed in our work. While consequences of LESA for the detectable neutrino signal have been addressed by Tamborra et al.

(2014b) as well as Walk et al. (2019), a potential connection of LESA and the gravitational-wave emission of newly formed proto-neutron stars will have to be investigated in the future (but for a first glimpse, see Powell and Müller 2019).

Chapter 5.

Conclusions

A challenging problem in core-collapse supernova (CCSN) theory is the modeling of the neutrino transport in self-consistent simulations. Because the governing Boltzmann equation cannot be solved in its full complexity, several approximations have been introduced. One of them is the ray-by-ray-plus (RbR+) approximation (Rampp and Janka, 2002; Buras et al., 2006b), which assumes the specific intensity of neutrinos to be symmetric around the radial direction of the associated spherical polar coordinate system. The RbR+ approximation has been employed by several groups in recent, sophisticated CCSN simulations (see, for example, Takiwaki et al. 2014, Lentz et al. 2015, and Summa et al. 2018). However, with RbR+ transport the non-radial (i.e., lateral and azimuthal) components of the neutrino flux vanish, whereas in a fully multidimensional (FMD) transport scheme the non-radial components are also evolved. After simulations in axial symmetry (2D) found the RbR+ approximation to foster shock revival for some progenitor stars (Skinner et al., 2016; Just et al., 2018), an evaluation of RbR+ in the general three-dimensional (3D) case is desperately needed.

In this thesis, we close this gap and assess—for the first time—the influence of the RbR+ approximation on the delayed neutrino-heating mechanism in self-consistent 3D CCSN simulations. To this end, we conducted in total eight 3D simulations with angular resolutions of $\approx 4°$ ("low resolution") and $\approx 2°$ ("high resolution"; using twice as many grid cells as for the low resolution cases) for two different progenitor models with masses of $9\,M_\odot$ and $20\,M_\odot$, respectively. For all these simulations we made use of the Aenus-Alcar code (Obergaulinger, 2008; Just et al., 2015, 2018), which implements an energy-dependent two-moment neutrino-transport scheme with an analytical closure relation ("M1 scheme") for electron neutrinos (ν_e), electron antineutrinos ($\bar{\nu}_e$), and heavy-lepton neutrinos (ν_x; representing all four other neutrino species). In addition to the FMD transport scheme, the code is capable of employing the RbR+ approximation by setting all non-radial flux components to zero.

Results For both progenitor models, we find a very good agreement of the post-bounce evolution between 3D simulations with RbR+ and FMD neutrino transport. While all runs of the $9\,M_\odot$ model lead to successful shock revival, the 3D simulations of the $20\,M_\odot$ progenitor model fail to revive the stalled shock wave in all cases until at least 400 ms after bounce. In contrast to our 2D simulations, in which the $20\,M_\odot$ model is dominated by violent sloshing motions of the standing accretion shock instability (SASI; Blondin et al. 2003) in the polar directions, our 3D simulations of the $20\,M_\odot$ model show a substantially different behavior with alternating phases of convective and SASI activity (consisting of both sloshing and spiral motions). For this reason, we do not reproduce the results from 2D simulations, in which the RbR+ approximation has been found to facilitate shock revival in particular in models with the strong axial sloshing motions of SASI. Instead, we find a much better agreement in 3D between simulations with RbR+ and FMD. For the convection-dominated $9\,M_\odot$ model, the agreement between RbR+ and FMD is even better. This model exhibits successful shock revival in all 3D simulations at roughly 300 ms after bounce,

without developing any SASI activity. The diagnostic explosion energies in both RbR+ and FMD cases reach $\approx 4 \times 10^{49}$ erg when measured at 600 ms, and are still growing by $\approx 10^{50}\,\mathrm{erg\,s^{-1}}$.

A detailed analysis of the $20\,\mathrm{M}_\odot$ progenitor model revealed further differences in the neutrino fluxes and heating rates. In agreement with a previous study by Sumiyoshi et al. (2015), we find larger angular variations of the radial neutrino fluxes with the RbR+ approximation, when compared to the FMD scheme. However, in 3D simulations these variations are systematically smaller than in corresponding 2D runs. Furthermore, the polar heating rates in 2D exhibit much larger fluctuations in simulations with the RbR+ approximation, when compared to 2D runs with the FMD scheme. In contrast, 3D models with both FMD and RbR+ transport show significantly less fluctuations of the heating rates in polar directions as well as in the instantaneous SASI direction. In view of these results, it is not surprising that we find a much better overall agreement in 3D between simulations with FMD and RbR+ neutrino transport.

LESA We further used our set of 3D models to evaluate the influence of the two neutrino-transport methods on the lepton-number emission self-sustained asymmetry (LESA)—a phenomenon that was first found by Tamborra et al. (2014a) in their self-consistent 3D CCSN simulations employing the RbR+ approximation. The key feature of LESA is a hemispheric, dipolar asymmetry of the electron lepton-number flux, i.e., the difference in number flux of ν_e and $\bar{\nu}_e$. Consistent with the original observations by Tamborra et al. (2014a,b), we found the dipole component of the lepton-number flux to rise up to a significant fraction of the monopole value (about 10 % to 30 % in our cases) for all of our models, i.e. with both FMD and RbR+ transport. The direction of the dipole vector remained roughly stable, only slowly migrating, during several tens to hundreds of milliseconds in all cases. Furthermore, we confirm SASI-induced modulations of the LESA dipole during phases of strong SASI activity, when the LESA dipole points nearly in the direction of SASI sloshing or the plane of spiral motions. Based on these results, we disprove speculations by Sumiyoshi et al. (2015) that LESA is a numerical artifact of the RbR+ approximation (compare recent results by O'Connor and Couch 2018b and Vartanyan et al. 2019a, who also witnessed LESA in their 3D simulations using FMD neutrino transport).

Although all our 3D simulations share the characteristic features of LESA listed above, we also noticed interesting differences regarding LESA between models computed with FMD and RbR+ transport. For both progenitor models, the dipole component of the lepton-number flux tends to grow faster with the RbR+ approximation, and reaches slightly larger maximum values, when compared to the corresponding FMD cases. However, the fully developed LESA dipole clearly dominates all higher modes in FMD simulations, whereas the RbR+ runs exhibit large contributions from the quadrupole moment and higher-order multipoles. The resulting "spottiness" of the spectrograms appears as a natural consequence of the RbR+ approximation: while in the FMD scheme non-radial neutrino fluxes smooth the angular variations of the radial fluxes, these angular variations remain more localized with the RbR+ approximation because non-radial flux components are neglected.

Furthermore, we attempted to improve the understanding of the physical origin of LESA by analyzing the transport of lepton number in the convective layer inside the proto-neutron star. We revealed a global, volume-filling dipolar flow around the convectively stable core. This flow effectively transports material with high lepton number to the hemisphere in direction of the LESA dipole. Finally, we discussed LESA as a possible consequence of Chandrasekhar's linear theory of thermal instability in spherical shells (Chandrasekhar, 1961).

Summary In this thesis, we demonstrated that 3D simulations with a RbR+ transport description result in the same overall post-bounce evolution as comparable models with a FMD neutrino-

transport scheme. We further showed that the LESA phenomenon is shared by all our 3D simulations with both FMD and RbR+ transport, thus proving that LESA is *not* an artifact of the RbR+ approximation. Hence, our results back up the use of the RbR+ approximation in 3D supernova simulations.

The preferred choice of neutrino-transport approximation depends on several aspects. Simulation codes with RbR+ transport benefit from a high parallel efficiency, because individual rays can be computed almost independently with only small communication overhead between MPI (Message Passing Interface) tasks. The FMD scheme, however, provides approximate representations of the non-diagonal elements of the neutrino-pressure tensor, which may be relevant for some physical problems, but are not directly available with a RbR+ treatment. Moreover, the RbR+ approximation is disfavored for fast rotating progenitor models, when non-radial neutrino fluxes at the strongly deformed neutron-star surface cannot be neglected. Nevertheless, the FMD scheme has yet to be tested in cases of fast rotating models.

Outlook In the end, two-moment closure schemes (in either FMD or RbR+ form) in general represent only approximations to the neutrino-transport problem and, thus, need to be tested against direct solutions of the full Boltzmann equation. Due to its computational complexity, however, such comparisons for time-dependent 2D and 3D simulations will be possible only with the next generation of supercomputers (see Sumiyoshi et al. 2015 and Nagakura et al. 2018 for first attempts with low resolution). Regarding the LESA phenomenon, future simulations need to cover a much longer time period than performed in this work in order to assess the consequences of LESA, like its impact on neutron-star kicks or on the nucleosynthesis in supernovae. The physical origin of LESA, and the detailed reason for the dominance of the dipole mode in particular, remain elusive. Future investigations of LESA can build up on the results presented in this thesis.

Appendix A.

Expressions for the Energy-Integrated Moments

For the sake of completeness, we provide in this appendix the expressions for the first four energy-integrated moments of the specific intensity. For the first three energy-integrated moments, we further specify the transformations from the co-moving frame into the lab frame.

In general, the energy-*dependent* angular moments of the specific intensity I, measured in the co-moving frame of the stellar fluid, are obtained by integrating I over the solid angle in momentum space $\mathrm{d}\Omega_n$ (see also Equations (2.6) in Section 2.2.2),

$$E = \frac{1}{c}\int \mathrm{d}\Omega_n \; I, \tag{A.1a}$$

$$F^i = \int \mathrm{d}\Omega_n \; I \; n^i, \tag{A.1b}$$

$$P^{ij} = \frac{1}{c}\int \mathrm{d}\Omega_n \; I \; n^i n^j, \tag{A.1c}$$

$$Q^{ijk} = \int \mathrm{d}\Omega_n \; I \; n^i n^j n^k. \tag{A.1d}$$

In addition to the angular moments of energy transport (Equations (A.1)), we define the angular moments of number transport by dividing the specific intensity by the neutrino energy ε,

$$N = \frac{1}{c}\int \mathrm{d}\Omega_n \; \varepsilon^{-1} \; I \qquad = \varepsilon^{-1} \; E, \tag{A.2a}$$

$$F_N^i = \int \mathrm{d}\Omega_n \; \varepsilon^{-1} \; I \; n^i \qquad = \varepsilon^{-1} \; F^i, \tag{A.2b}$$

$$P_N^{ij} = \frac{1}{c}\int \mathrm{d}\Omega_n \; \varepsilon^{-1} \; I \; n^i n^j \qquad = \varepsilon^{-1} \; P^{ij}, \tag{A.2c}$$

$$Q_N^{ijk} = \int \mathrm{d}\Omega_n \; \varepsilon^{-1} \; I \; n^i n^j n^k = \varepsilon^{-1} \; Q^{ijk}. \tag{A.2d}$$

Energy-Integrated Moments

The energy-integrated moments of energy transport (corresponding to Equations (A.1)) are given by

$$\bar{E} = \int \mathrm{d}\varepsilon \; E, \tag{A.3a}$$

$$\bar{F}^i = \int \mathrm{d}\varepsilon \; F^i, \tag{A.3b}$$

$$\bar{P}^{ij} = \int \mathrm{d}\varepsilon \; P^{ij}, \tag{A.3c}$$

$$\bar{Q}^{ijk} = \int \mathrm{d}\varepsilon \; Q^{ijk}. \tag{A.3d}$$

For the moments of number transport (corresponding to Equations (A.2)), we find

$$\bar{N} = \int \mathrm{d}\varepsilon\, \varepsilon^{-1}\, E, \tag{A.4a}$$

$$\bar{F}_N^i = \int \mathrm{d}\varepsilon\, \varepsilon^{-1}\, F^i, \tag{A.4b}$$

$$\bar{P}_N^{ij} = \int \mathrm{d}\varepsilon\, \varepsilon^{-1}\, P^{ij}, \tag{A.4c}$$

$$\bar{Q}_N^{ijk} = \int \mathrm{d}\varepsilon\, \varepsilon^{-1}\, Q^{ijk}. \tag{A.4d}$$

Transformations into the Lab Frame

The energy-integrated moments of energy transport in the lab frame are obtained from the moments in the co-moving frame to order v/c by (see, for example, Just et al. 2015, Equations (10a) to (10c))

$$\bar{E}_{\mathrm{lab}} = \bar{E} + \frac{2}{c^2} v_i \bar{F}^i, \tag{A.5a}$$

$$\bar{F}^i_{\mathrm{lab}} = \bar{F}^i + v^i \bar{E} + v_j \bar{P}^{ij}, \tag{A.5b}$$

$$\bar{P}^{ij}_{\mathrm{lab}} = \bar{P}^{ij} + \frac{1}{c^2} \bar{F}^i v^j + \frac{1}{c^2} \bar{F}^j v^i. \tag{A.5c}$$

The corresponding expressions for the moments of number transport in the lab frame, accurate to order v/c, read

$$\bar{N}_{\mathrm{lab}} = \bar{N} + \frac{1}{c^2} v_i \bar{F}^i_N, \tag{A.6a}$$

$$\bar{F}^i_{N,\mathrm{lab}} = \bar{F}^i_N + v^i \bar{N}, \tag{A.6b}$$

$$\bar{P}^{ij}_{N,\mathrm{lab}} = \bar{P}^{ij}_N + \frac{1}{c^2} \bar{F}^i_N v^j + \frac{1}{c^2} \bar{F}^j_N v^i + \frac{1}{c^2} v_k \bar{Q}^{ijk}_N. \tag{A.6c}$$

While Equations (A.6a) and (A.6b) can be found in Just et al. (2015, Equations (11a) and (11b)), we provide the derivation of Equation (A.6c) in the following section.

Derivation of $\bar{P}_N$ in the Lab Frame

In this section, we derive the expression for $\bar{P}^{ij}_{N,\mathrm{lab}}$ (see Equation (A.6c)). To improve the readability, we change the notation of variables throughout this section as follows: variables with tilde (e.g. $\tilde{x}$) are defined in the lab frame, and variables with hat (e.g. $\hat{x}$) are defined in the co-moving frame. Furthermore, since we only deal with energy-integrated quantities here, we omit the bar (indicating energy integration) from variables, so that $\tilde{P}^{ij}_N = \bar{P}^{ij}_{N,\mathrm{lab}}$. For Lorentz transformations we use the Lorentz factor γ,

$$\gamma = \left(1 - \beta^2\right)^{-1/2}, \tag{A.7}$$

where

$$\beta = \frac{v}{c}, \tag{A.8}$$

with the speed of light c, the fluid velocity v_i, and its absolute value v. To an accuracy of order v/c, we can use the approximation $\gamma \approx 1$.

We start with the general expression for P_N^{ij} in an arbitrary frame, which can be found from combining Equation (A.4c) and Equation (A.1c),

$$P_N^{ij} = \frac{1}{c} \int \varepsilon^{-1} \, n^i \, n^j \, I \, \mathrm{d}\varepsilon \, \mathrm{d}\Omega_n \tag{A.9a}$$

$$= \frac{h}{c^3} \int \varepsilon^2 \, n^i \, n^j \, f \, \mathrm{d}\varepsilon \, \mathrm{d}\mu \, \mathrm{d}\varphi. \tag{A.9b}$$

Here, ε is the neutrino energy, $\mu = \cos\vartheta$, with ϑ and φ being the angles in momentum space, so that $\mathrm{d}\Omega_n = \mathrm{d}\mu \, \mathrm{d}\varphi$; n^i and n^j are the normal vectors in momentum space, and I is the specific intensity, which relates to the invariant particle distribution function f by means of Equation (2.3). The expression for P_N^{ij} in the lab frame then reads

$$\tilde{P}_N^{ij} = \frac{h}{c^3} \int \tilde{\varepsilon}^2 \, \tilde{n}^i \, \tilde{n}^j \, \tilde{f} \, \mathrm{d}\tilde{\varepsilon} \, \mathrm{d}\tilde{\mu} \, \mathrm{d}\tilde{\varphi}. \tag{A.10}$$

To obtain an expression for $\tilde{P}_N^{ij}$ depending only on quantities in the co-moving frame, we need to transform all quantities one by one.

The particle distribution function f is invariant,

$$\tilde{f} = \hat{f}. \tag{A.11}$$

The neutrino energy ε transforms as (Munier and Weaver, 1986a, Equation (40))

$$\tilde{\varepsilon} = \hat{\varepsilon} \, \gamma \left(1 + \frac{v_i \hat{n}^i}{c} \right). \tag{A.12}$$

With the relations

$$\mu = \frac{v_i n^i}{v}, \tag{A.13}$$

$$\beta \, \mu = \frac{v_i n^i}{c}, \tag{A.14}$$

and the approximation $\gamma \approx 1$ we obtain

$$\tilde{\varepsilon} \approx \hat{\varepsilon} \, \left(1 + \beta \hat{\mu} \right). \tag{A.15}$$

The transformation for n^i reads (Munier and Weaver, 1986a, we use the back transformation of Equations (49) and (79), and again $\gamma \approx 1$ was assumed)

$$\tilde{n}^i \approx \frac{\hat{n}^i + v^i/c}{1 + \beta \hat{\mu}}, \tag{A.16}$$

so we find

$$\tilde{\mu} \approx \frac{\hat{\mu} + \beta}{1 + \beta \hat{\mu}}. \tag{A.17}$$

Using Equations (A.15) and (A.17), together with $\tilde{\varphi} = \hat{\varphi}$, the differentials transform (accurate to order v/c) as

$$\mathrm{d}\tilde{\varepsilon} \, \mathrm{d}\tilde{\mu} \, \mathrm{d}\tilde{\varphi} \approx \frac{1}{1 + \beta \hat{\mu}} \, \mathrm{d}\hat{\varepsilon} \, \mathrm{d}\hat{\mu} \, \mathrm{d}\hat{\varphi}. \tag{A.18}$$

Putting everything together, we obtain

$$\tilde{P}_N^{ij} = \frac{h}{c^3}\int \hat{\varepsilon}^2\ (1+\beta\hat{\mu})^2\,\frac{\hat{n}^i + v^i/c}{1+\beta\hat{\mu}}\,\frac{\hat{n}^j + v^j/c}{1+\beta\hat{\mu}}\,\hat{f}\,\frac{1}{1+\beta\hat{\mu}}\ \mathrm{d}\hat{\varepsilon}\ \mathrm{d}\hat{\mu}\ \mathrm{d}\hat{\varphi} \tag{A.19a}$$

$$= \frac{h}{c^3}\int \hat{\varepsilon}^2\ \left(\hat{n}^i + v^i/c\right)\ \left(\hat{n}^j + v^j/c\right)\ \hat{f}\,\frac{1}{1+\beta\hat{\mu}}\ \mathrm{d}\hat{\varepsilon}\ \mathrm{d}\hat{\mu}\ \mathrm{d}\hat{\varphi} \tag{A.19b}$$

$$\approx \frac{h}{c^3}\int \hat{\varepsilon}^2\ \left(\hat{n}^i + v^i/c\right)\ \left(\hat{n}^j + v^j/c\right)\ \hat{f}\ (1-\beta\hat{\mu})\ \mathrm{d}\hat{\varepsilon}\ \mathrm{d}\hat{\mu}\ \mathrm{d}\hat{\varphi} \tag{A.19c}$$

$$\approx \frac{1}{c}\int \frac{1}{\hat{\varepsilon}}\ \left(\hat{n}^i\hat{n}^j + \frac{v^j}{c}\hat{n}^i + \frac{v^i}{c}\hat{n}^j - \frac{v_k\hat{n}^k}{c}\,\hat{n}^i\hat{n}^j\right)\hat{I}\ \mathrm{d}\hat{\varepsilon}\ \mathrm{d}\hat{\Omega}_\mathrm{m}, \tag{A.19d}$$

where in Equation (A.19c) we used

$$\frac{1}{1+\beta\hat{\mu}} \approx (1-\beta\hat{\mu}) \tag{A.20}$$

for small $\beta\hat{\mu}$, and in Equation (A.19d) we dropped terms with quadratic or higher order in v/c, and reintroduced the specific intensity by means of Equation (2.3). We identify several angular moments of number transport (see Equations (A.4) together with Equations (A.1)), and finally obtain

$$\tilde{P}_N^{ij} = \hat{P}_N^{ij} + \frac{1}{c^2}\hat{F}_N^i v^j + \frac{1}{c^2}\hat{F}_N^j v^i + \frac{1}{c^2}v_k\hat{Q}_N^{ijk}. \tag{A.21}$$

Appendix B.

Calculation of the χ Parameter

In this appendix we present and compare several methods to calculate the χ parameter (see Equation (3.9)). In particular, we focus on the computation of the Brunt-Väisälä frequency, which enters the definition of χ, and the various possible ways to perform the angular averages and the radial integral. The contents of this chapter have already been published in the Appendix of Glas et al. (2019b, see also the information on already published material on page 73).

The χ Parameter

The χ parameter (Foglizzo et al., 2006) is used to analyze the conditions for the growth of convection in the post-shock layer. It essentially relates the advection timescale, which can be approximated by the ratio of the radial cell width $\mathrm{d}r$ over the radial velocity v_r, to the timescale of convective growth, given by the inverse of the Brunt-Väisälä frequency ω_{BV},

$$\chi = \int \frac{\omega_{\mathrm{BV}}}{|v_r|}\,\mathrm{d}r. \tag{B.1}$$

The radial integral in Equation (B.1) extends over the gain layer, i.e., from the gain radius to the shock radius. According to Foglizzo et al. (2006, assuming the linear regime for the growth of perturbations), the χ parameter must exceed a critical value of ~ 3 for the growth of convection in the gain layer. In formulating this criterion, Foglizzo et al. (2006) considered a spherically symmetric gain-layer configuration. However, since in reality the gain layer has a complex multi-dimensional structure for most of the time, non-trivial ambiguities arise as to how to compute and angle average the quantities entering Equation (B.1). As a consequence, as was already demonstrated by Fernández et al. (2014), different calculation methods may lead to significantly different values of χ. In order to assess the sensitivity of χ with respect to its practical computation, in this appendix we systematically compare various possible methods for computing χ. All following tests are based on the 3D model 'S20 FMD L' of the present study (for a discussion of this model, see Section 3.3).

The Brunt-Väisälä Frequency

Before considering the χ parameter itself, we start by comparing two possibilities for the numerical evaluation of the local Brunt-Väisälä frequency ω_{BV}. We use a definition that is based on the criterion for Ledoux convection,

$$\omega_{\mathrm{BV}} = \mathrm{sign}\left(C_{\mathrm{led}}\right)\sqrt{\frac{\partial\phi_{\mathrm{grav}}}{\partial r}\rho^{-1}\left|C_{\mathrm{led}}\right|} > 0, \tag{B.2}$$

with the gravitational potential ϕ_{grav} and the density ρ. The Ledoux criterion is given by

$$C_{\mathrm{led}} = \left(\frac{\partial\rho}{\partial s}\right)_{p,Y_e}\frac{\partial s}{\partial r} + \left(\frac{\partial\rho}{\partial Y_e}\right)_{p,s}\frac{\partial Y_e}{\partial r} > 0, \tag{B.3}$$

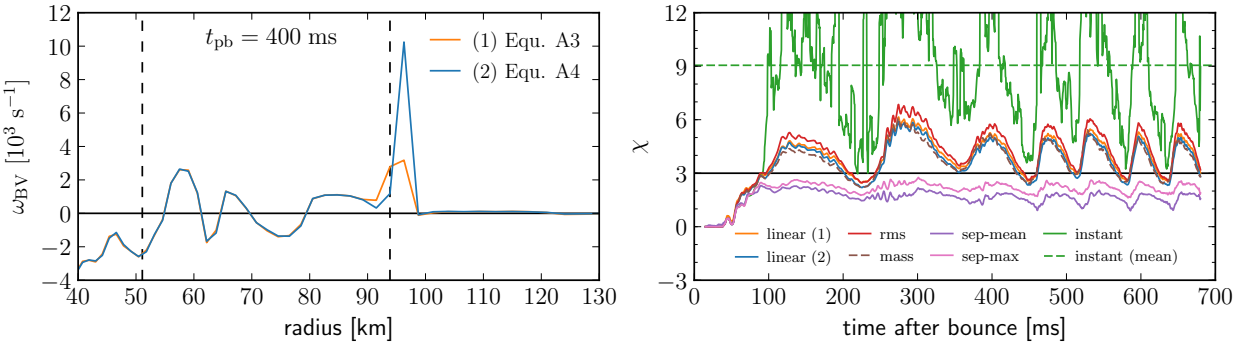

Figure B.1.: Radial profiles of the Brunt-Väisälä frequency ω_{BV} (left panel), evaluated at arbitrarily chosen angles of $\theta = 6°$ and $\phi = 2.25°$ for a snapshot of model 'S20 FMD L' at a post-bounce time of $t_{pb} = 400\,ms$, and the χ parameter as a function of time after bounce (right panel) for the same model. The line colors and line styles correspond to different methods that we use to calculate the Brunt-Väisälä frequency and the χ parameter (see labels and Table B.1). The horizontal lines depict the critical values for $\omega_{BV} = 0$ (left panel) and $\chi = 3$ (right panel), and the dashed lines in the left panel display the gain and shock radii, R_g and $R_s(\theta = 6°, \phi = 2.25°)$, respectively. The large peak in ω_{BV} just in front of the shock is nonphysical (see text) and is not included in the radial integral for the calculation of χ. The χ parameter was smoothed by running averages of 5 ms. This figure is taken from Glas et al. (2019b, Figure 16).

with entropy per baryon s, electron fraction Y_e, and pressure p. For this definition of the Ledoux criterion convectively unstable regions fulfill the condition $C_{led} > 0$ or $\omega_{BV} > 0$. The thermodynamic derivatives in Equation (B.3) with respect to entropy and electron fraction need to be calculated from the equation of state. Another way to calculate the Ledoux criterion is given by (see, e.g., Hüdepohl 2014, Equation (2.35) and Appendix B therein)

$$C_{led} = \frac{\partial \rho}{\partial r} - \frac{1}{c_s^2}\frac{\partial p}{\partial r} > 0, \tag{B.4}$$

with the local speed of sound c_s. This analytically identical alternative definition is based on radial gradients of density and pressure and, therefore, does not need additional information from the equation of state. Both definitions of C_{led} result in basically identical values for the Brunt-Väisälä frequency, as can be seen in the left panel of Figure B.1, which shows radial profiles of ω_{BV} for method 1 (orange line, based on Equation (B.3)) and for method 2 (blue line, based on Equation (B.4)). The large peak in ω_{BV} for method 2 just in front of the shock (right dashed line) is a physically irrelevant numerical artifact because it results from the numerical description of the shock front as a discretized flow structure. For this reason, we do not include this region in the radial integral in Equation (B.1). The results of the above comparison, first, support the correct implementation of both computation methods in our analysis routines, and second, confirm that numerical differences between both methods are small enough to render both methods equivalent for the practical evaluation of χ.

Three Different Classes for the Calculation of χ

We now consider different computation methods for the χ parameter. The right panel of Figure B.1 shows the χ parameter as a function of the time after bounce, obtained using the variations of calculation methods that are described in the following (see Table B.1 for an overview of the methods). We identify three different classes of possible outcomes (corresponding to the three

distinct groups of lines), which result from different realizations regarding the angular average and the radial integral in Equation (B.1). In the first class (consisting of methods "linear (1)", "linear (2)", "rms", and "mass") χ is computed as

$$\chi = \int \frac{\langle \omega_{\rm BV}(r,\theta,\phi)\rangle}{|\langle v_r(r,\theta,\phi)\rangle|}\,{\rm d}r, \tag{B.5}$$

where angle brackets denote angular averaging over angles θ and ϕ. Instead of averaging the three-dimensional Brunt-Väisälä frequency $\omega_{\rm BV}(r,\theta,\phi)$, it is possible to obtain a radial profile $\omega_{\rm BV}(r)$ from angle-averaged quantities $\langle\phi_{\rm grav}\rangle$, $\langle\rho\rangle$, $\langle c_{\rm s}\rangle$, and $\langle p\rangle$. Using the radial profile $\omega_{\rm BV}(r)$ we obtain the second class (consisting of methods "sep-mean" and "sep-max") by

$$\chi = \int \frac{\omega_{\rm BV}(r)}{|\langle v_r(r,\theta,\phi)\rangle|}\,{\rm d}r. \tag{B.6}$$

The third class (method "instant") is obtained by performing the angle average *after* the radial integral,

$$\chi = \left\langle \int \frac{\omega_{\rm BV}(r,\theta,\phi)}{|v_r(r,\theta,\phi)|}\,{\rm d}r \right\rangle. \tag{B.7}$$

In addition to these three main classes we investigated further variations of the calculation of χ. We describe these variations in great detail in the following paragraphs. An overview of all seven methods that we used to calculate the χ parameter can be found in Table B.1.

Class 1: Equation (B.5)

Starting with the first class (Equation (B.5)), we investigate the influence of the calculation method for the Ledoux criterion (see discussion above). The excellent agreement between both calculation methods for $C_{\rm led}$ can also be seen from results for the χ parameter: the values for method 1 (orange line; see Equation (B.3)) agree very well with those obtained from method 2 (blue line; see Equation (B.4)). Both results for χ have been calculated with "linear" angular averaging of the Brunt-Väisälä frequency as expressed in Equation (B.5). When performing the angular average over $\omega_{\rm BV}(r,\theta,\phi)$ we only take into account regions (a) that lie in the gain layer with radii $R_{\rm g} < r < R_{\rm s}(\theta,\phi)$ and, thus, we exclude the nonphysical shock artifact mentioned above, and (b) that are locally unstable for convection, i.e. where $\omega_{\rm BV}(r,\theta,\phi) > 0$. In contrast, the angular average of the radial velocity, $\langle v_r(r,\theta,\phi)\rangle$, is calculated from all zones with $R_{\rm g} < r < R_{\rm s}^{\rm max}$ with the maximum shock radius $R_{\rm s}^{\rm max}$ to capture the mean properties of the entire flow. We apply volumetric angular averaging for $\omega_{\rm BV}$ and v_r, i.e., we weight all values with the volume of the corresponding cells and normalize the sum by dividing through the total volume. Since possibly not all zones of a radial shell contribute to the angular average of $\omega_{\rm BV}$ due to the constraints $\omega_{\rm BV}(r,\theta,\phi) > 0$ and $R_{\rm g} < r < R_{\rm s}(\theta,\phi)$, also the total volume that is used for the normalization of $\omega_{\rm BV}$ is calculated only from contributing zones. After angular averaging, the radial integral in Equation (B.5) is formally carried out from the gain radius $R_{\rm g}$ to the maximum shock radius $R_{\rm s}^{\rm max}$.

For root-mean-squared averaging of $\omega_{\rm BV}$ ("rms" in Table B.1) as described in Fernández et al. (2014) we replace in Equation (B.5) the linear angular average $\langle\omega_{\rm BV}\rangle$ by the root-mean-squared angular average $\langle\omega_{\rm BV}^2\rangle^{1/2}$. As shown in the right panel of Figure B.1, root-mean-squared averaging increases the χ parameter by values of at most 1 (red line) with respect to the "linear" averaging. Even smaller differences with respect to the "linear" angular averaging method with volumetric weighting are found when the weighting is performed with the mass of each zone ("mass" in Table B.1, brown dashed line in Figure B.1).

Table B.1.: Possible methods to calculate the χ parameter. The volume that is considered for angle averaging and radial integration is given as a range between the gain radius R_g and the angle-dependent shock radius $R_\mathrm{s}(\theta,\phi)$, the angle-averaged mean shock radius R_s, or the maximum shock radius $R_\mathrm{s}^\mathrm{max}$. For the analysis in the main text of this thesis, we use the method "linear (2)". This table is taken from Glas et al. (2019b, Table 2).

Method Name	Class	Angle Averaging	Weighting	Considered Volume	Method for C_led
linear (1)	Eq. (B.5)	linear	volume	$R_\mathrm{g} < r < R_\mathrm{s}(\theta,\phi)$	1 - Eq. (B.3)
linear (2)	Eq. (B.5)	linear	volume	$R_\mathrm{g} < r < R_\mathrm{s}(\theta,\phi)$	2 - Eq. (B.4)
rms	Eq. (B.5)	root-mean-squared	volume	$R_\mathrm{g} < r < R_\mathrm{s}(\theta,\phi)$	2 - Eq. (B.4)
mass	Eq. (B.5)	linear	mass	$R_\mathrm{g} < r < R_\mathrm{s}(\theta,\phi)$	2 - Eq. (B.4)
sep-mean	Eq. (B.6)	separate	volume	$R_\mathrm{g} < r < R_\mathrm{s}$	2 - Eq. (B.4)
sep-max	Eq. (B.6)	separate	volume	$R_\mathrm{g} < r < R_\mathrm{s}^\mathrm{max}$	2 - Eq. (B.4)
instant	Eq. (B.7)	instantaneous	volume	$R_\mathrm{g} < r < R_\mathrm{s}(\theta,\phi)$	2 - Eq. (B.4)

Class 2: Equation (B.6)

The second class for the calculation of χ (Equation (B.6)) employs separately angle-averaged quantities $\langle\phi_\mathrm{grav}\rangle$, $\langle\rho\rangle$, $\langle c_\mathrm{s}\rangle$, and $\langle p\rangle$ to compute a spherically symmetric radial profile $\omega_\mathrm{BV}(r)$ (see Equations (B.2) and (B.4)). Here, the angular averages are again computed with volumetric weighting and include all zones with $R_\mathrm{g} < r < R_\mathrm{s}$ or $R_\mathrm{g} < r < R_\mathrm{s}^\mathrm{max}$, depending on the method: We compare values for χ where the radial integral (including only regions where $\omega_\mathrm{BV}(r) > 0$) was performed up to the mean shock radius R_s ("sep-mean" in Table B.1) and the maximum shock radius $R_\mathrm{s}^\mathrm{max}$ ("sep-max" in Table B.1), respectively. Separately averaging the quantities leads to significantly reduced values of χ not exceeding 2 (for "sep-mean", purple line in Figure B.1) or 3 (for "sep-max", pink line in Figure B.1). Since both Summa et al. (2016) and Just et al. (2018) use similar methods as the "sep-mean" one, this could explain the rather small values that both studies find for the χ parameter in their 2D simulations for the same s20 progenitor. The values of the χ parameter in this case are slightly below the critical level suggested by Foglizzo et al. (2006).

Class 3: Equation (B.7)

Last, with the third class (Equation (B.7)) we consider an "instantaneously" averaged χ parameter (similarly to Fernández et al. 2014), which is obtained by angle averaging the χ parameter *after* performing the radial integral ("instant" in Table B.1). In this case, only zones with $\omega_\mathrm{BV}(r,\theta,\phi) > 0$ and $R_\mathrm{g} < r < R_\mathrm{s}(\theta,\phi)$ are considered for the radial integral. We find for this method significantly larger values for the χ parameter (green line) than for all other methods, with a temporal average as large as 9.1 (green dashed line). This result roughly agrees with the findings by Fernández et al. (2014), who argue that the instantaneously averaged χ parameter does not capture the properties of the mean flow and, thus, is not suitable to analyze the conditions for convective growth in the gain layer.

Concluding Remarks

For the analysis in Chapter 3 of this thesis we use the "linear (2)" method, which matches best our observations regarding the phases of growth of convection ($\chi \gtrsim 3$ in agreement with the critical value from the linear analysis by Foglizzo et al. 2006) and of SASI growth (small values of the χ parameter, roughly $\chi \lesssim 4$).

Additional Information

Published Material

Large parts of this thesis have already been published in two peer-reviewed articles in the Astrophysical Journal (Glas et al. 2019a and Glas et al. 2019b; © AAS. Reproduced with permission) with me being the leading author for both articles. Mainly, this concerns Section 2.6 (published in Glas et al. 2019b), Chapter 3 (published in Glas et al. 2019b), Chapter 4 (published in Glas et al. 2019a), and Appendix B (published in Glas et al. 2019b). I referenced the corresponding publication in the beginning of each chapter, section, or appendix, and I included corresponding remarks in all figure and table captions. In order to submit a proper and coherent thesis, I adapted some of the published contents to the style and narrative of the thesis, and I furthermore added some passages, explanations, and equations in between, corrected some spelling mistakes, introduced new subsection titles, and added new references within the thesis and to recently published literature.

Funding

This project was supported by the European Research Council through grant ERC-AdG No. 341157-COCO2CASA, and by the Deutsche Forschungsgemeinschaft through Sonderforschungbereich SFB 1258 "Neutrinos and Dark Matter in Astro- and Particle Physics" (NDM) and the Excellence Cluster Universe (EXC 153; http://www.universe-cluster.de/).

Computer Resources

Computer resources for this project have been provided by the Leibniz Supercomputing Centre (LRZ) under grant pr62za, and by the Max Planck Computing and Data Facility (MPCDF) on the HPC systems Hydra, Draco, and Cobra.

Software

For this project we used the following software:

- Aenus-Alcar (Obergaulinger, 2008; Just et al., 2015, 2018)
- NumPy and Scipy (Oliphant, 2007)
- IPython (Pérez and Granger, 2007)
- Matplotlib (Hunter, 2007)
- VisIt (Childs et al., 2012)

List of Abbreviations

1D one dimensional, i.e. spherically symmetric.

2D two dimensional, i.e. axially symmetric.

3D three dimensional.

CCSN core-collapse supernova.

FMD fully multidimensional.

LESA lepton-number emission self-sustained asymmetry.

p.b. post bounce, i.e., after the core bounce.

RbR+ ray-by-ray-plus.

SASI standing accretion shock instability.

List of Figures

List of Tables

Bibliography

B. P. Abbott, R. Abbott, T. D. Abbott, et al. First targeted search for gravitational-wave bursts from core-collapse supernovae in data of first-generation laser interferometer detectors. *PhRvD*, 94(10):102001, **2016**. doi:10.1103/PhysRevD.94.102001.

E. N. Alexeyev, L. N. Alexeyeva, I. V. Krivosheina, and V. I. Volchenko. Detection of the neutrino signal from SN 1987A in the LMC using the INR Baksan underground scintillation telescope. *Physics Letters B*, 205(2-3):209–214, **1988**. doi:10.1016/0370-2693(88)91651-6.

W. Baade and F. Zwicky. On Super-novae. *Proceedings of the National Academy of Science*, 20(5): 254–259, **1934a**. doi:10.1073/pnas.20.5.254.

W. Baade and F. Zwicky. Cosmic Rays from Super-novae. *Proceedings of the National Academy of Science*, 20(5):259–263, **1934b**. doi:10.1073/pnas.20.5.259.

H. A. Bethe. Supernova mechanisms. *Reviews of Modern Physics*, 62:801–866, **1990**. doi:10.1103/RevModPhys.62.801.

H. A. Bethe and J. R. Wilson. Revival of a stalled supernova shock by neutrino heating. *ApJ*, 295: 14–23, **1985**. doi:10.1086/163343.

R. M. Bionta, G. Blewitt, C. B. Bratton, et al. Observation of a neutrino burst in coincidence with supernova 1987A in the Large Magellanic Cloud. *PhRvL*, 58(14):1494–1496, **1987**. doi:10.1103/PhysRevLett.58.1494.

R. Blandford and R. Bühler. *Supernova of 1054 and its Remnant, the Crab Nebula*. Springer, Cham, **2017**. doi:10.1007/978-3-319-21846-5_46.

J. M. Blondin and S. Shaw. Linear Growth of Spiral SASI Modes in Core-Collapse Supernovae. *ApJ*, 656:366–371, **2007**. doi:10.1086/510614.

J. M. Blondin, A. Mezzacappa, and C. DeMarino. Stability of Standing Accretion Shocks, with an Eye toward Core-Collapse Supernovae. *ApJ*, 584:971–980, **2003**. doi:10.1086/345812.

R. Bollig, H.-T. Janka, A. Lohs, et al. Muon Creation in Supernova Matter Facilitates Neutrino-Driven Explosions. *Physical Review Letters*, 119(24):242702, **2017**. doi:10.1103/PhysRevLett.119.242702.

S. W. Bruenn. Stellar core collapse - Numerical model and infall epoch. *ApJS*, 58:771–841, **1985**. doi:10.1086/191056.

S. W. Bruenn and A. Mezzacappa. Ion screening effects and stellar collapse. *PhRvD*, 56:7529–7547, **1997**. doi:10.1103/PhysRevD.56.7529.

S. W. Bruenn, A. Mezzacappa, W. R. Hix, et al. Axisymmetric Ab Initio Core-collapse Supernova Simulations of 12-25 $M_{\odot}$ Stars. *ApJL*, 767:L6, **2013**. doi:10.1088/2041-8205/767/1/L6.

S. W. Bruenn, E. J. Lentz, W. R. Hix, et al. The Development of Explosions in Axisymmetric Ab Initio Core-collapse Supernova Simulations of 12-25 M Stars. *ApJ*, 818:123, **2016**. doi:10.3847/0004-637X/818/2/123.

R. Buras, H.-T. Janka, M. Rampp, and K. Kifonidis. Two-dimensional hydrodynamic core-collapse supernova simulations with spectral neutrino transport. II. Models for different progenitor stars. *A&A*, 457:281–308, **2006a**. doi:10.1051/0004-6361:20054654.

R. Buras, M. Rampp, H.-T. Janka, and K. Kifonidis. Two-dimensional hydrodynamic core-collapse supernova simulations with spectral neutrino transport. I. Numerical method and results for a 15 $M_\odot$ star. *A&A*, 447:1049–1092, **2006b**. doi:10.1051/0004-6361:20053783.

A. Burrows. Colloquium: Perspectives on core-collapse supernova theory. *Reviews of Modern Physics*, 85:245–261, **2013**. doi:10.1103/RevModPhys.85.245.

A. Burrows, J. C. Dolence, and J. W. Murphy. An Investigation into the Character of Pre-explosion Core-collapse Supernova Shock Motion. *ApJ*, 759:5, **2012**. doi:10.1088/0004-637X/759/1/5.

A. Burrows, D. Radice, D. Vartanyan, et al. The Overarching Framework of Core-Collapse Supernova Explosions as Revealed by 3D FORNAX Simulations. *MNRAS*, page 2925, **2019**. doi:10.1093/mnras/stz3223.

C. Y. Cardall, E. Endeve, and A. Mezzacappa. Conservative 3+1 general relativistic variable Eddington tensor radiation transport equations. *PhRvD*, 87(10):103004, **2013**. doi:10.1103/PhysRevD.87.103004.

J. Cernohorsky. Symmetries in neutrino-electron scattering. *ApJ*, 433:247–249, **1994**. doi:10.1086/174639.

S. Chandrasekhar. The highly collapsed configurations of a stellar mass. *MNRAS*, 91:456–466, **1931**. doi:10.1093/mnras/91.5.456.

S. Chandrasekhar. The highly collapsed configurations of a stellar mass (Second paper). *MNRAS*, 95:207–225, **1935**. doi:10.1093/mnras/95.3.207.

S. Chandrasekhar. *Hydrodynamic and hydromagnetic stability (International Series of Monographs on Physics)*. Oxford University Press, **1961**.

H. Childs, E. Brugger, B. Whitlock, et al. VisIt: An End-User Tool For Visualizing and Analyzing Very Large Data. In *High Performance Visualization–Enabling Extreme-Scale Scientific Insight*, pages 357–372. Chapman and Hall/CRC, **2012**.

D. H. Clark and F. R. Stephenson. *The historical supernovae*. Pergamon, Oxford, **1977**.

P. Colella and P. R. Woodward. The Piecewise Parabolic Method (PPM) for Gas-Dynamical Simulations. *Journal of Computational Physics*, 54:174–201, **1984**. doi:10.1016/0021-9991(84)90143-8.

S. A. Colgate and M. H. Johnson. Hydrodynamic Origin of Cosmic Rays. *PhRvL*, 5(6):235–238, **1960**. doi:10.1103/PhysRevLett.5.235.

S. A. Colgate and R. H. White. The Hydrodynamic Behavior of Supernovae Explosions. *ApJ*, 143: 626, **1966**. doi:10.1086/148549.

J. M. Comella, H. D. Craft, R. V. E. Lovelace, and J. M. Sutton. Crab Nebula Pulsar NP 0532. *Nature*, 221(5179):453–454, **1969**. doi:10.1038/221453a0.

S. M. Couch. On the Impact of Three Dimensions in Simulations of Neutrino-driven Core-collapse Supernova Explosions. *ApJ*, 775:35, **2013**. doi:10.1088/0004-637X/775/1/35.

S. M. Couch and C. D. Ott. The Role of Turbulence in Neutrino-driven Core-collapse Supernova Explosions. *ApJ*, 799:5, **2015**. doi:10.1088/0004-637X/799/1/5.

R. Courant, K. Friedrichs, and H. Lewy. Über die partiellen Differenzengleichungen der mathematischen Physik. *Mathematische Annalen*, 100:32–74, **1928**. doi:10.1007/BF01448839.

J. C. Dolence, A. Burrows, and W. Zhang. Two-dimensional Core-collapse Supernova Models with Multi-dimensional Transport. *ApJ*, 800:10, **2015**. doi:10.1088/0004-637X/800/1/10.

B. Einfeldt. On Godunov-Type Methods for Gas Dynamics. *SIAM Journal on Numerical Analysis*, 25(2):294–318, **1988**. doi:10.1137/0725021.

B. Einfeldt, P. L. Roe, C. D. Munz, and B. Sjogreen. On Godunov-Type Methods near Low Densities. *Journal of Computational Physics*, 92(2):273–295, **1991**. doi:10.1016/0021-9991(91)90211-3.

R. Fernández. Hydrodynamics of Core-collapse Supernovae at the Transition to Explosion. I. Spherical Symmetry. *ApJ*, 749:142, **2012**. doi:10.1088/0004-637X/749/2/142.

R. Fernández. Three-dimensional simulations of SASI- and convection-dominated core-collapse supernovae. *MNRAS*, 452:2071–2086, **2015**. doi:10.1093/mnras/stv1463.

R. Fernández and C. Thompson. Stability of a Spherical Accretion Shock with Nuclear Dissociation. *ApJ*, 697:1827–1841, **2009**. doi:10.1088/0004-637X/697/2/1827.

R. Fernández, B. Müller, T. Foglizzo, and H.-T. Janka. Characterizing SASI- and convection-dominated core-collapse supernova explosions in two dimensions. *MNRAS*, 440:2763–2780, **2014**. doi:10.1093/mnras/stu408.

T. Foglizzo, L. Scheck, and H.-T. Janka. Neutrino-driven Convection versus Advection in Core-Collapse Supernovae. *ApJ*, 652:1436–1450, **2006**. doi:10.1086/508443.

T. Foglizzo, P. Galletti, L. Scheck, and H. T. Janka. Instability of a Stalled Accretion Shock: Evidence for the Advective-Acoustic Cycle. *ApJ*, 654(2):1006–1021, **2007**. doi:10.1086/509612.

T. Foglizzo, R. Kazeroni, J. Guilet, et al. The Explosion Mechanism of Core-Collapse Supernovae: Progress in Supernova Theory and Experiments. *PASA*, 32:e009, **2015**. doi:10.1017/pasa.2015.9.

F. Foucart, E. O'Connor, L. Roberts, et al. Post-merger evolution of a neutron star-black hole binary with neutrino transport. *PhRvD*, 91(12):124021, **2015**. doi:10.1103/PhysRevD.91.124021.

R. Glas, H. T. Janka, T. Melson, G. Stockinger, and O. Just. Effects of LESA in Three-dimensional Supernova Simulations with Multidimensional and Ray-by-ray-plus Neutrino Transport. *ApJ*, 881 (1):36, **2019a**. doi:10.3847/1538-4357/ab275c.

R. Glas, O. Just, H. T. Janka, and M. Obergaulinger. Three-dimensional Core-collapse Supernova Simulations with Multidimensional Neutrino Transport Compared to the Ray-by-ray-plus Approximation. *ApJ*, 873:45, **2019b**. doi:10.3847/1538-4357/ab0423.

S. K. Godunov. A difference method for numerical calculation of discontinuous solutions of the equations of hydrodynamics. *Mat. Sb. (N.S.)*, 47(89)(3):271–306, **1959**. URL `http://mi.mathnet.ru/msb4873`.

F. Hanke, A. Marek, B. Müller, and H.-T. Janka. Is Strong SASI Activity the Key to Successful Neutrino-driven Supernova Explosions? *ApJ*, 755:138, **2012**. doi:10.1088/0004-637X/755/2/138.

F. Hanke, B. Müller, A. Wongwathanarat, A. Marek, and H.-T. Janka. SASI Activity in Three-dimensional Neutrino-hydrodynamics Simulations of Supernova Cores. *ApJ*, 770:66, **2013**. doi:10.1088/0004-637X/770/1/66.

S. Hannestad and G. Raffelt. Supernova Neutrino Opacity from Nucleon-Nucleon Bremsstrahlung and Related Processes. *ApJ*, 507:339–352, **1998**. doi:10.1086/306303.

A. Harten, P. D. Lax, and B. van Leer. On upstream differencing and godunov-type schemes for hyperbolic conservation laws. *SIAM Review*, 25(1):35–61, **1983**. doi:10.1137/1025002.

J. J. Hester. The Crab Nebula: An Astrophysical Chimera. *ARA&A*, 46:127–155, **2008**. doi:10.1146/annurev.astro.45.051806.110608.

W. Hillebrandt and J. C. Niemeyer. Type IA Supernova Explosion Models. *Annual Review of Astronomy and Astrophysics*, 38:191–230, **2000**. doi:10.1146/annurev.astro.38.1.191.

W. Hillebrandt, M. Kromer, F. K. Röpke, and A. J. Ruiter. Towards an understanding of Type Ia supernovae from a synthesis of theory and observations. *Frontiers of Physics*, 8(2):116–143, **2013**. doi:10.1007/s11467-013-0303-2.

K. Hirata, T. Kajita, M. Koshiba, et al. Observation of a neutrino burst from the supernova SN1987A. *PhRvL*, 58(14):1490–1493, **1987**. doi:10.1103/PhysRevLett.58.1490.

C. J. Horowitz. Neutrino trapping in a supernova and the screening of weak neutral currents. *PhRvD*, 55:4577–4581, **1997**. doi:10.1103/PhysRevD.55.4577.

C. J. Horowitz. Weak magnetism for antineutrinos in supernovae. *PhRvD*, 65(4):043001, **2002**. doi:10.1103/PhysRevD.65.043001.

C. J. Horowitz, O. L. Caballero, Z. Lin, E. O'Connor, and A. Schwenk. Neutrino-nucleon scattering in supernova matter from the virial expansion. *PhRvC*, 95(2):025801, **2017**. doi:10.1103/PhysRevC.95.025801.

J. D. Hunter. Matplotlib: A 2d graphics environment. *Computing in Science & Engineering*, 9(3): 90–95, **2007**. doi:10.1109/MCSE.2007.55.

L. Hüdepohl. *Neutrinos from the Formation, Cooling and Black Hole Collapse of Neutron Stars*. PhD thesis, TUM, **2014**.

H.-T. Janka. Conditions for shock revival by neutrino heating in core-collapse supernovae. *A&A*, 368:527–560, **2001**. doi:10.1051/0004-6361:20010012.

H.-T. Janka. Explosion Mechanisms of Core-Collapse Supernovae. *Annual Review of Nuclear and Particle Science*, 62:407–451, **2012**. doi:10.1146/annurev-nucl-102711-094901.

H.-T. Janka, F. Hanke, L. Hüdepohl, et al. Core-collapse supernovae: Reflections and directions. *Progress of Theoretical and Experimental Physics*, 2012(1):01A309, **2012**. doi:10.1093/ptep/pts067.

H.-T. Janka, T. Melson, and A. Summa. Physics of Core-Collapse Supernovae in Three Dimensions: A Sneak Preview. *Annual Review of Nuclear and Particle Science*, 66:341–375, **2016**. doi:10.1146/annurev-nucl-102115-044747.

O. Just, M. Obergaulinger, and H.-T. Janka. A new multidimensional, energy-dependent two-moment transport code for neutrino-hydrodynamics. *MNRAS*, 453:3386–3413, **2015**. doi:10.1093/mnras/stv1892.

O. Just, R. Bollig, H.-T. Janka, et al. Core-collapse supernova simulations in one and two dimensions: comparison of codes and approximations. *MNRAS*, 481:4786–4814, **2018**. doi:10.1093/mnras/sty2578.

K. Kotake, K. Sato, and K. Takahashi. Explosion mechanism, neutrino burst and gravitational wave in core-collapse supernovae. *Reports on Progress in Physics*, 69:971–1143, **2006**. doi:10.1088/0034-4885/69/4/R03.

K. Kotake, T. Takiwaki, T. Fischer, K. Nakamura, and G. Martínez-Pinedo. Impact of Neutrino Opacities on Core-collapse Supernova Simulations. *ApJ*, 853:170, **2018**. doi:10.3847/1538-4357/aaa716.

T. Kuroda, T. Takiwaki, and K. Kotake. A New Multi-energy Neutrino Radiation-Hydrodynamics Code in Full General Relativity and Its Application to the Gravitational Collapse of Massive Stars. *ApJS*, 222:20, **2016**. doi:10.3847/0067-0049/222/2/20.

E. J. Lentz, S. W. Bruenn, W. R. Hix, et al. Three-dimensional Core-collapse Supernova Simulated Using a 15 $M_\odot$ Progenitor. *ApJL*, 807:L31, **2015**. doi:10.1088/2041-8205/807/2/L31.

C. D. Levermore. Relating Eddington factors to flux limiters. *JQSRT*, 31:149–160, **1984**. doi:10.1016/0022-4073(84)90112-2.

M. Liebendörfer, S. C. Whitehouse, and T. Fischer. The Isotropic Diffusion Source Approximation for Supernova Neutrino Transport. *ApJ*, 698:1174–1190, **2009**. doi:10.1088/0004-637X/698/2/1174.

K. Lundmark. Suspected New Stars Recorded in Old Chronicles and Among Recent Meridian Observations. *Publications of the Astronomical Society of the Pacific*, 33(195):225, **1921**. doi:10.1086/123101.

A. G. Lyne, C. A. Jordan, F. Graham-Smith, et al. 45 years of rotation of the Crab pulsar. *Monthly Notices of the Royal Astronomical Society*, 446(1):857–864, **2015**. doi:10.1093/mnras/stu2118.

Q. A. Mabanta and J. W. Murphy. How Turbulence Enables Core-collapse Supernova Explosions. *ApJ*, 856:22, **2018**. doi:10.3847/1538-4357/aaaec7.

A. Marek and H.-T. Janka. Delayed Neutrino-Driven Supernova Explosions Aided by the Standing Accretion-Shock Instability. *ApJ*, 694:664–696, **2009**. doi:10.1088/0004-637X/694/1/664.

A. Marek, H. Dimmelmeier, H.-T. Janka, E. Müller, and R. Buras. Exploring the relativistic regime with Newtonian hydrodynamics: an improved effective gravitational potential for supernova simulations. *A&A*, 445:273–289, **2006**. doi:10.1051/0004-6361:20052840.

T. Melson, H.-T. Janka, R. Bollig, et al. Neutrino-driven Explosion of a 20 Solar-mass Star in Three Dimensions Enabled by Strange-quark Contributions to Neutrino-Nucleon Scattering. *ApJL*, 808: L42, **2015a**. doi:10.1088/2041-8205/808/2/L42.

T. Melson, H.-T. Janka, and A. Marek. Neutrino-driven Supernova of a Low-mass Iron-core Progenitor Boosted by Three-dimensional Turbulent Convection. *ApJL*, 801:L24, **2015b**. doi:10.1088/2041-8205/801/2/L24.

A. Mezzacappa and S. W. Bruenn. Type II supernovae and Boltzmann neutrino transport - The infall phase. *ApJ*, 405:637–668, **1993**. doi:10.1086/172394.

A. Mignone. High-order conservative reconstruction schemes for finite volume methods in cylindrical and spherical coordinates. *Journal of Computational Physics*, 270:784–814, **2014**. doi:10.1016/j.jcp.2014.04.001.

G. N. Minerbo. Maximum entropy Eddington factors. *JQSRT*, 20:541–545, **1978**. doi:10.1016/0022-4073(78)90024-9.

B. Müller. The dynamics of neutrino-driven supernova explosions after shock revival in 2D and 3D. *MNRAS*, 453:287–310, **2015**. doi:10.1093/mnras/stv1611.

B. Müller and H.-T. Janka. Non-radial instabilities and progenitor asphericities in core-collapse supernovae. *MNRAS*, 448:2141–2174, **2015**. doi:10.1093/mnras/stv101.

B. Müller, H.-T. Janka, and A. Heger. New Two-dimensional Models of Supernova Explosions by the Neutrino-heating Mechanism: Evidence for Different Instability Regimes in Collapsing Stellar Cores. *ApJ*, 761:72, **2012a**. doi:10.1088/0004-637X/761/1/72.

B. Müller, H.-T. Janka, and A. Marek. A New Multi-dimensional General Relativistic Neutrino Hydrodynamics Code for Core-collapse Supernovae. II. Relativistic Explosion Models of Core-collapse Supernovae. *ApJ*, 756:84, **2012b**. doi:10.1088/0004-637X/756/1/84.

B. Müller, T. Melson, A. Heger, and H.-T. Janka. Supernova simulations from a 3D progenitor model - Impact of perturbations and evolution of explosion properties. *MNRAS*, 472:491–513, **2017**. doi:10.1093/mnras/stx1962.

A. Munier and R. Weaver. Radiation transfer in the fluid frame: A covariant formulation. Part I: Radiation hydrodynamics. *Computer Physics Reports*, 3:127–164, **1986a**. doi:10.1016/0167-7977(86)90007-9.

A. Munier and R. Weaver. Radiation transfer in the fluid frame: A covariant formulation. Part II: The radiation transfer equation. *Computer Physics Reports*, 3:165–208, **1986b**. doi:10.1016/0167-7977(86)90008-0.

E. M. Murchikova, E. Abdikamalov, and T. Urbatsch. Analytic closures for M1 neutrino transport. *MNRAS*, 469:1725–1737, **2017**. doi:10.1093/mnras/stx986.

J. W. Murphy, J. C. Dolence, and A. Burrows. The Dominance of Neutrino-driven Convection in Core-collapse Supernovae. *ApJ*, 771:52, **2013**. doi:10.1088/0004-637X/771/1/52.

H. Nagakura, W. Iwakami, S. Furusawa, et al. Simulations of Core-collapse Supernovae in Spatial Axisymmetry with Full Boltzmann Neutrino Transport. *ApJ*, 854:136, **2018**. doi:10.3847/1538-4357/aaac29.

M. Obergaulinger. *Astrophysical magnetohydrodynamics and radiative transfer: numerical methods and applications*. PhD thesis, TUM, **2008**.

E. O'Connor. An Open-source Neutrino Radiation Hydrodynamics Code for Core-collapse Supernovae. *ApJS*, 219:24, **2015**. doi:10.1088/0067-0049/219/2/24.

E. P. O'Connor and S. M. Couch. Two-dimensional Core-collapse Supernova Explosions Aided by General Relativity with Multidimensional Neutrino Transport. *ApJ*, 854:63, **2018a**. doi:10.3847/1538-4357/aaa893.

E. P. O'Connor and S. M. Couch. Exploring Fundamentally Three-dimensional Phenomena in High-fidelity Simulations of Core-collapse Supernovae. *ApJ*, 865:81, **2018b**. doi:10.3847/1538-4357/aadcf7.

T. E. Oliphant. Python for scientific computing. *Computing in Science Engineering*, 9(3):10–20, **2007**. ISSN 1521-9615. doi:10.1109/MCSE.2007.58.

C. D. Ott, E. Abdikamalov, P. Mösta, et al. General-relativistic Simulations of Three-dimensional Core-collapse Supernovae. *ApJ*, 768:115, **2013**. doi:10.1088/0004-637X/768/2/115.

C. D. Ott, L. F. Roberts, A. da Silva Schneider, et al. The Progenitor Dependence of Core-collapse Supernovae from Three-dimensional Simulations with Progenitor Models of 12–40 M $_\odot$. *ApJL*, 855:L3, **2018**. doi:10.3847/2041-8213/aaa967.

K.-C. Pan, M. Liebendörfer, M. Hempel, and F.-K. Thielemann. Two-dimensional Core-collapse Supernova Simulations with the Isotropic Diffusion Source Approximation for Neutrino Transport. *ApJ*, 817:72, **2016**. doi:10.3847/0004-637X/817/1/72.

S. Pennisi. On third order tensor-valued isotropic functions. *International Journal of Engineering Science*, 30(5):679 – 692, **1992**. ISSN 0020-7225. doi:https://doi.org/10.1016/0020-7225(92)90011-5.

S. Pennisi and M. Trovato. On the irreducibility of professor g.f. smith's representations for isotropic functions. *International Journal of Engineering Science*, 25(8):1059 – 1065, **1987**. ISSN 0020-7225. doi:https://doi.org/10.1016/0020-7225(87)90097-8.

F. Pérez and B. E. Granger. IPython: a system for interactive scientific computing. *Computing in Science and Engineering*, 9(3):21–29, **2007**. ISSN 1521-9615. doi:10.1109/MCSE.2007.53. URL `https://ipython.org`.

J. A. Pons, J. A. Miralles, and J. M. A. Ibanez. Legendre expansion of the $\vec{\nu}$. *A&AS*, 129:343–351, **1998**. doi:10.1051/aas:1998189.

J. Powell and B. Müller. Gravitational wave emission from 3D explosion models of core-collapse supernovae with low and normal explosion energies. *MNRAS*, 487(1):1178–1190, **2019**. doi:10.1093/mnras/stz1304.

D. Radice, C. D. Ott, E. Abdikamalov, et al. Neutrino-driven Convection in Core-collapse Supernovae: High-resolution Simulations. *ApJ*, 820:76, **2016**. doi:10.3847/0004-637X/820/1/76.

D. Radice, A. Burrows, D. Vartanyan, M. A. Skinner, and J. C. Dolence. Electron-capture and Low-mass Iron-core-collapse Supernovae: New Neutrino-radiation-hydrodynamics Simulations. *ApJ*, 850:43, **2017**. doi:10.3847/1538-4357/aa92c5.

M. Rampp and H.-T. Janka. Radiation hydrodynamics with neutrinos. Variable Eddington factor method for core-collapse supernova simulations. *A&A*, 396:361–392, **2002**. doi:10.1051/0004-6361:20021398.

S. Richers, H. Nagakura, C. D. Ott, et al. A Detailed Comparison of Multidimensional Boltzmann Neutrino Transport Methods in Core-collapse Supernovae. *ApJ*, 847(2):133, **2017**. doi:10.3847/1538-4357/aa8bb2.

L. F. Roberts, C. D. Ott, R. Haas, et al. General-Relativistic Three-Dimensional Multi-group Neutrino Radiation-Hydrodynamics Simulations of Core-Collapse Supernovae. *ApJ*, 831:98, **2016**. doi:10.3847/0004-637X/831/1/98.

L. Scheck, H.-T. Janka, T. Foglizzo, and K. Kifonidis. Multidimensional supernova simulations with approximative neutrino transport. II. Convection and the advective-acoustic cycle in the supernova core. *A&A*, 477:931–952, **2008**. doi:10.1051/0004-6361:20077701.

M. Shibata, K. Kiuchi, Y. Sekiguchi, and Y. Suwa. Truncated Moment Formalism for Radiation Hydrodynamics in Numerical Relativity. *Progress of Theoretical Physics*, 125:1255–1287, **2011**. doi:10.1143/PTP.125.1255.

M. A. Skinner, A. Burrows, and J. C. Dolence. Should One Use the Ray-by-Ray Approximation in Core-collapse Supernova Simulations? *ApJ*, 831:81, **2016**. doi:10.3847/0004-637X/831/1/81.

D. H. Staelin and I. Reifenstein, Edward C. Pulsating Radio Sources near the Crab Nebula. *Science*, 162(3861):1481–1483, **1968**. doi:10.1126/science.162.3861.1481.

A. W. Steiner, M. Hempel, and T. Fischer. Core-collapse Supernova Equations of State Based on Neutron Star Observations. *ApJ*, 774:17, **2013**. doi:10.1088/0004-637X/774/1/17.

G. Stockinger. - Features of LESA - A Study on the Lepton-Number Emission Self-Sustained Asymmetry as a new Phenomenon in Supernova Explosions. Master's thesis, TUM, **2015**.

T. Sukhbold, T. Ertl, S. E. Woosley, J. M. Brown, and H.-T. Janka. Core-collapse Supernovae from 9 to 120 Solar Masses Based on Neutrino-powered Explosions. *ApJ*, 821:38, **2016**. doi:10.3847/0004-637X/821/1/38.

K. Sumiyoshi and S. Yamada. Neutrino Transfer in Three Dimensions for Core-collapse Supernovae. I. Static Configurations. *ApJS*, 199:17, **2012**. doi:10.1088/0067-0049/199/1/17.

K. Sumiyoshi, T. Takiwaki, H. Matsufuru, and S. Yamada. Multi-dimensional Features of Neutrino Transfer in Core-collapse Supernovae. *ApJS*, 216:5, **2015**. doi:10.1088/0067-0049/216/1/5.

A. Summa, F. Hanke, H.-T. Janka, et al. Progenitor-dependent Explosion Dynamics in Self-consistent, Axisymmetric Simulations of Neutrino-driven Core-collapse Supernovae. *ApJ*, 825:6, **2016**. doi:10.3847/0004-637X/825/1/6.

A. Summa, H.-T. Janka, T. Melson, and A. Marek. Rotation-supported Neutrino-driven Supernova Explosions in Three Dimensions and the Critical Luminosity Condition. *ApJ*, 852:28, **2018**. doi:10.3847/1538-4357/aa9ce8.

T. Takiwaki, K. Kotake, and Y. Suwa. Three-dimensional Hydrodynamic Core-collapse Supernova Simulations for an 11.2 $M_\odot$ Star with Spectral Neutrino Transport. *ApJ*, 749:98, **2012**. doi:10.1088/0004-637X/749/2/98.

T. Takiwaki, K. Kotake, and Y. Suwa. A Comparison of Two- and Three-dimensional Neutrino-hydrodynamics Simulations of Core-collapse Supernovae. *ApJ*, 786:83, **2014**. doi:10.1088/0004-637X/786/2/83.

I. Tamborra, F. Hanke, H.-T. Janka, et al. Self-sustained Asymmetry of Lepton-number Emission: A New Phenomenon during the Supernova Shock-accretion Phase in Three Dimensions. *ApJ*, 792:96, **2014a**. doi:10.1088/0004-637X/792/2/96.

I. Tamborra, G. Raffelt, F. Hanke, H.-T. Janka, and B. Müller. Neutrino emission characteristics and detection opportunities based on three-dimensional supernova simulations. *PhRvD*, 90(4): 045032, **2014b**. doi:10.1103/PhysRevD.90.045032.

T. A. Thompson, A. Burrows, and P. A. Pinto. Shock Breakout in Core-Collapse Supernovae and Its Neutrino Signature. *ApJ*, 592:434–456, **2003**. doi:10.1086/375701.

T. A. Thompson, E. Quataert, and A. Burrows. Viscosity and Rotation in Core-Collapse Supernovae. *ApJ*, 620:861–877, **2005**. doi:10.1086/427177.

E. F. Toro. *Riemann Solvers and Numerical Methods for Fluid Dynamics: A Practical Introduction*. Springer-Verlag Berlin Heidelberg, **1997**. doi:10.1007/978-3-662-03490-3.

E. F. Toro, M. Spruce, and W. Speares. Restoration of the contact surface in the HLL-Riemann solver. *Shock Waves*, 4:25–34, **1994**. doi:10.1007/BF01414629.

K. A. van Riper. General relativistic hydrodynamics and the adiabatic collapse of stellar cores. *ApJ*, 232:558–571, **1979**. doi:10.1086/157314.

D. Vartanyan, A. Burrows, D. Radice, M. A. Skinner, and J. Dolence. Revival of the fittest: exploding core-collapse supernovae from 12 to 25 $M_\odot$. *MNRAS*, 477:3091–3108, **2018**. doi:10.1093/mnras/sty809.

D. Vartanyan, A. Burrows, and D. Radice. Temporal and Angular Variations of 3D Core-Collapse Supernova Emissions and their Physical Correlations. *MNRAS*, page 2235, **2019a**. doi:10.1093/mnras/stz2307.

D. Vartanyan, A. Burrows, D. Radice, M. A. Skinner, and J. Dolence. A successful 3D core-collapse supernova explosion model. *MNRAS*, 482(1):351–369, **2019b**. doi:10.1093/mnras/sty2585.

L. Walk, I. Tamborra, H.-T. Janka, and A. Summa. Effects of the standing accretion-shock instability and the lepton-emission self-sustained asymmetry in the neutrino emission of rotating supernovae. *PhRvD*, 100(6):063018, **2019**. doi:10.1103/PhysRevD.100.063018.

S. E. Woosley and A. Heger. Nucleosynthesis and remnants in massive stars of solar metallicity. *PhR*, 442:269–283, **2007**. doi:10.1016/j.physrep.2007.02.009.

S. E. Woosley and A. Heger. The Remarkable Deaths of 9-11 Solar Mass Stars. *ApJ*, 810:34, **2015**. doi:10.1088/0004-637X/810/1/34.

W. R. Yueh and J. R. Buchler. Neutrino transport in supernova models - S_N method. *ApJ*, 217: 565–577, **1977**. doi:10.1086/155605.

W. Zhang, L. Howell, A. Almgren, et al. CASTRO: A New Compressible Astrophysical Solver. III. Multigroup Radiation Hydrodynamics. *ApJS*, 204:7, **2013**. doi:10.1088/0067-0049/204/1/7.

Acknowledgments (Danksagung)

Nach mehr als drei Jahren intensiver Arbeit an meinem Dissertationsthema möchte ich gerne einigen Personen danken, ohne deren Unterstützung diese Doktorarbeit nicht möglich gewesen wäre.

Zunächst danke ich meinem Betreuer, *Hans-Thomas Janka*, zum einen für die Gelegenheit, zu diesem spannenden Thema im Rahmen einer Doktorarbeit forschen zu können, und zum anderen für seine immerwährende Unterstützung meiner Arbeit – sowohl durch wertvolle Ideen und Anregungen zum Thema, als auch die Möglichkeit, auf internationalen Konferenzen kostbare Erfahrungen zu sammeln.

Außerdem danke ich meinem Mentor, *Oliver Just*, von dem ich schon während meiner Zeit als Masterand sehr viel lernen durfte: Ich bedanke mich für zahlreiche Erklärungen zur Physik von Kernkollaps-Supernovae im Allgemeinen, und zu den Details des Neutrino-Transports im Speziellen, sowie für die Einführung in sämtliche numerische Methoden, die wir im Alcar-Code verwenden.

Ich danke zudem meinen Kollaborateuren, *Hans-Thomas Janka*, *Oliver Just*, *Tobias Melson* und *Georg Stockinger* für die hervorragende Zusammenarbeit an unseren zwei Publikationen (Glas et al. 2019b und Glas et al. 2019a).

Ich danke *Shaoming Zhang* für die Hilfe beim Erstellen der Visualisierungen in Abbildungen 4.6 und 4.7, und *Robert Bollig* für die Erweiterung der „SFHo“-Zustandsgleichung.

Weiterer Dank gebührt den Administratoren am Max-Planck-Institut für Astrophysik (MPA), am Rechenzentrum der Max-Planck-Gesellschaft (MPCDF) und am Leibniz-Rechenzentrum der Bayerischen Akademie der Wissenschaften (LRZ) für die Hilfe bei technischen Problemen. Besonders hervorheben möchte ich *Andreas Weiss* vom MPA, der mir bei Computer-Problemen aller Art immer hilfreich zur Seite stand.

I am grateful to *Thomas Ertl*, *Naveen Yadav*, and *Martin Schlecker* for proofreading parts of this thesis and providing many useful comments on the manuscript, and to *Daniel Kresse* for lots of inspiring discussions concerning this dissertation.

Moreover, I thank all my colleagues from our group for very enjoyable coffee breaks and lunchtimes, for stimulating discussions about both scientific and non-scientific topics, and, in general, for a very pleasant working environment at our institute.

A special thanks goes to my former and current (long-term) office mates, *Hai Liang Chen*, *Ninoy Rahman*, and *Daniel Kresse*, who contributed to a very pleasant atmosphere in our office.

Zu guter Letzt danke ich meiner Frau, *Carlotta Glas*, für ihre großartige Unterstützung während der kompletten letzten dreieinhalb Jahre.